

AN ABSTRACT OF THE DISSERTATION OF

Ty C. Nietupski for the degree of Doctor of Philosophy in Sustainable Forest Management presented on June 3, 2021.

Title: Characterizing an Annual Grass Invasion and Its Link to Environmental and Disturbance Factors Using Remote Sensing: New Tools and Applications

Abstract approved:

Temesgen Hailemariam

Becky K. Kerns

The spread of nonnative species across the globe has contributed to biodiversity loss and changes in ecosystem structure and function. Monitoring the introduction, naturalization, and spread of introduced species is critical in abating negative impacts wrought by species invasions. However, providing basic information concerning the presence or spread of many introduced species is often only considered once the invasion is already at an advanced stage, resulting in economic or ecological impacts. To better assess the present and future effects of and risk from introduced species, a clear understanding of invasive species populations' spatial and temporal patterns is needed. In some cases, remote sensing can serve as a useful information source that may be leveraged to characterize and monitor the invasion of nonnative species.

This dissertation utilizes remote sensing and other geospatial data sources to better understand a nonnative annual grass (*Ventenata dubia*) invasion in the northwestern United States. Each research chapter builds a different facet of our understanding of this invasion by connecting land-surface processes, environmental conditions, and landscape disturbances. These three different topics help to describe the current state of the invasion, how it progressed to this state, and what this may mean for the future.

The first research-chapter adapts image fusion methods to a cloud-computing environment in an effort to improve the spatial and temporal resolution of estimates of land surface phenology. The research focused on whether these methods would enable the estimation of phenology in heterogeneous landscapes that have historically been difficult to characterize. This chapter showed that high-quality image fusion results are possible with less processing time when image fusion is conducted in a cloud-computing environment. Further, this chapter showed that phenology estimated from these data can capture patterns occurring in grassland, shrubland, and open forest land cover types.

The second research-chapter leverages the improved land surface phenology estimates from the first research-chapter to model the present distribution of the invasive annual grass species *Ventenata dubia* in the Blue Mountains Ecoregion of the interior Pacific Northwest. The results from this chapter suggest that both phenological and environmental information are needed to best detect populations of *ventenata*. The model based on phenological and environmental information predicted that *ventenata* was present in 7.8% of the Blue Mountains Ecoregion in 2017.

The third research-chapter uses the information gained from the preceding chapters to examine the change occurring over a decade of invasion by applying the model developed in the second research-chapter to the image archive and examining the invasion progression. Spatial and temporal patterns of the invasion were characterized by their association with the biophysical environment and the effect of wildfire on *ventenata* occurrence was investigated. This analysis revealed that *ventenata* may have been introduced to lower shrubland ecosystems but has since transitioned to higher elevation dry conifer forests and areas with abundant ecotone. Furthermore, this chapter shows that wildfire occurrence and severity was associated with an increased probability of invasion in some parts of the interior Pacific Northwest.

Although this research is focused on a specific annual grass species (*Ventenata dubia*), insights gained from this investigation are applicable to other invasive annual grasses. This research contributes to the scientific advancement in the study of exotic plant invasion and provides useful baseline ecological information that can be employed to inform both policy and management. Additionally, the methods developed for cloud-computing-based image fusion offer a useful tool to the remote sensing community that has the flexibility to be utilized for many applications.

©Copyright by Ty C. Nietupski
June 3, 2021
All Rights Reserved

Characterizing an Annual Grass Invasion and Its Link to Environmental and
Disturbance Factors Using Remote Sensing: New Tools and Applications

by
Ty C. Nietupski

A DISSERTATION

submitted to

Oregon State University

in partial fulfillment of
the requirements for the
degree of

Doctor of Philosophy

Presented June 3, 2021
Commencement June 2021

Doctor of Philosophy dissertation of Ty C. Nietupski presented on June 3, 2021.

APPROVED:

Co-Major Professor, representing Sustainable Forest Management

Co-Major Professor, representing Sustainable Forest Management

Head of the Department of Forest Engineering, Resources and Management

Dean of the Graduate School

I understand that my dissertation will become part of the permanent collection of Oregon State University libraries. My signature below authorizes release of my dissertation to any reader upon request.

Ty C. Nietupski, Author

ACKNOWLEDGEMENTS

I would like to express my sincere gratitude towards my co-advisers Dr. Becky Kerns and Dr. Temesgen Hailemariam. Without their support and encouragement, I would not have been able to achieve success in my research. I also owe a debt of gratitude to my committee members, who shared their insight through the stages of my research and provided stimulating discussions surrounding invasive species, remote sensing, and fire. I would like to specifically thank Dr. Robert Kennedy, who spent many hours discussing and troubleshooting technical aspects of my research.

Finishing this program would not have been possible without the help of collaborators outside of Oregon State University. Many people contributed their knowledge and data to this project. I would particularly like to thank Michelle Day and Bridgett Naylor for their many contributions to data wrangling and field sampling. I would also like to thank Kent Cole for being willing to wander around the Blue Mountains with me for a summer in search of *ventenata*.

I would also like to thank the other graduate students in the Forest Measurements and Biometrics Laboratory for their friendship, technical support, and many interesting conversations. Without them, I would not have enjoyed my experience nearly as much and would not have learned about such a diversity of topics.

As for my family and friends, thank you for putting up with me over the last few years. To my parents, your love and exemplary ethic to work for others before yourselves is a tremendous source of inspiration. None of this would have been possible without the love, emotional support, and writing and statistical advice of my partner, Karin Kralicek. I could not have wished for a better companion to share this journey with.

I would also like to thank the organizations that supported me financially. The primary funding for this research was provided by the Joint Fire Science Program

(Proposal ID: 16-1-01-21) through a Joint Venture Agreement between the USFS Pacific Northwest Research Station and Oregon State University. Additional financial support for my program was provided by the Department of Forest Engineering, Resources and Management, the Department of Forest Ecosystems and Society, and the College of Earth, Ocean, and Atmospheric Sciences.

There are too many people to thank by name but to all of those that supported me throughout the last few years and prior- thank you!

CONTRIBUTION OF AUTHORS

Dr. Temesgen Hailemariam provided technical advice and assisted with the refinement of manuscripts. Dr. Becky Kerns assisted with the study design, result interpretation, and revisions to the manuscripts. Dr. Robert Kennedy provided technical advice and revisions to the chapter 2 manuscript.

TABLE OF CONTENTS

	<u>Page</u>
1. INTRODUCTION.....	1
1.1. Background	1
1.2. Remote Sensing Methods for Invasive Species Mapping	4
1.3. Research Overview.....	7
2. SPATIOTEMPORAL IMAGE FUSION IN GOOGLE EARTH ENGINE FOR ANNUAL ESTIMATES OF LAND SURFACE PHENOLOGY IN A HETEROGENEOUS LANDSCAPE.....	10
2.1. Abstract	11
2.2. Introduction	13
2.3. Methods	16
2.3.1. Study Area.....	16
2.3.2. Spatio-temporal Image Fusion.....	18
2.3.3. Land Surface Phenology.....	24
2.4. Results	31
2.4.1. Spatio-temporal Image fusion	31
2.4.2. Land Surface Phenology.....	35
2.5. Discussion.....	40
2.5.1. Spatio-temporal Image Fusion.....	41
2.5.2. Land Surface Phenology.....	42
2.5.3. Future Directions and Potential Applications.....	44
2.6. Conclusions	46
2.7. Acknowledgements.....	46
3. MAPPING THE INVASIVE ANNUAL GRASS VENTENATA (<i>VENTENATA DUBIA</i>) IN THE NORTHWESTERN UNITED STATES.....	48
3.1. Abstract	48
3.2. Introduction	50
3.3. Methods	53
3.3.1. Study Area.....	53
3.3.2. Data.....	54
3.3.3. Modeling.....	57
3.4. Results	60
3.4.1. Model Performance	60
3.4.2. Model Interpretation	63

TABLE OF CONTENTS (Continued)

	<u>Page</u>
3.4.3. Predicted Distribution.....	65
3.4.4. Elevation and Vegetation Associations.....	69
3.5. Discussion.....	71
3.5.1. Regional Assessment	71
3.5.2. Model Performance	73
3.5.3. Phenological and Climatic Relationships	75
3.5.4. Interpretation and Challenges	76
3.6. Conclusion.....	77
3.7. Acknowledgements.....	78
4. SPATIAL DYNAMICS AND PATTERNS OF RECENT <i>VENTENATA DUBIA</i> INVASION IN THE BLUE MOUNTAINS ECOREGION OF THE PACIFIC NORTHWEST	79
4.1. Abstract	79
4.2. Introduction	81
4.3. Methods	83
4.3.1. Study Area.....	83
4.3.2. Predicting Ventenata	84
4.3.3. Regional Change	88
4.3.4. Case Studies	93
4.4. Results	94
4.4.1. Regional Change	94
4.4.2. Case Studies	106
4.5. Discussion.....	110
4.5.1. Phenology and Biophysical Setting.....	111
4.5.2. Wildfire	113
4.5.3. Caveats and Considerations.....	116
4.6. Conclusion.....	117
5. CONCLUSION	119
BIBLIOGRAPHY	124
APPENDICES	145

LIST OF FIGURES

<u>Figure</u>		<u>Page</u>
2.1	The study area including one of the Landsat scenes (Figure 2.5, 2.6) used to evaluate image fusion. Land cover types within the region vary at fine spatial scales, as shown by the National Land Cover Database (NLCD) 2016 land cover classes (Yang et al., 2018). The PhenoCam sites (purple) and the Starkey Experimental Forest and Range site (blue) used to evaluate LSP estimates are also indicated	17
2.2	The dates of all Landsat images used in the GEE image fusion and LSP estimation for each WRS-2 scene. For LSP estimation, images occurring in January and February 2017 were dropped due to persistent cloud and snow cover during this period. An orange point indicates that the Landsat image was paired with a MODIS image for GEE image fusion. A black point indicates that the image was not used in the GEE image fusion because it had greater than 5-percent cloud cover, but valid pixels from the image were retained in the final time series. Percent cloud cover is indicated by the transparency of each point where high transparency correspond with high cloud cover. Specific images used to evaluate the accuracy of image-fusion predictions are denoted with an "X" mark	25
2.3	Example of the fitted double-logistic model (black line) for a single pixel's time series after post-processing (orange points). Blue dotted lines show the start of green-up (1), maturity (3), and dormancy (5). Blue dashed lines show the start of season (2) and end of season (4). Black arrows show the length of season (6), seasonal amplitude (7), and 'winter' NDVI (8). The bottom two panels show the first and second derivative of the fitted double-logistic model and the local maxima and minima corresponding to the various phenometrics	27
2.4	The image taken at approximately noon on July 5 th , 2017 for each of the four PhenoCams. Each image recorded by the PhenoCams was masked using the shaded polygons (region of interest). The masked images were then used to calculate the mean digital number for each band.....	29

LIST OF FIGURES (Continued)

<u>Figure</u>	<u>Page</u>
2.5	Three panels showing the 2016 NCLD land-cover classes, NDVI from the true Landsat image, and NDVI from the GEE image fusion prediction. This example is from path 43/ row 29 on June 7 th , 2017. Image pairs used for this prediction occurred on May 22 nd , 2017 and June 23 rd , 2017. The location of this scene is shown in the context of the study region in Figure 2.1. NDVI values below 0 shown in blue to help focus on the variation in the 0 to 1 range. Masked pixels are shown in white..... 32
2.6	Hex grid of the NDVI derived from true Landsat vs. the GEE image fusion for path 43/ row 29 on June 7 th , 2017 (DOY 158, Figure 2.5)..... 33
2.7	Performance of the GEE image fusion and locally run ESTARFM within the four NLCD land-cover types and within the scenes located at A) path 43/ row 29, and B) path 43/ row 30. The x-axis shows the DOY in which the model performance was evaluated for each scene (3 DOY's/scene). Performance metrics evaluated for each scene-date combination include RMSPE, bias, and SRB..... 35
2.8	Comparison of the time series and model fit for the sagebrush PhenoCam site near Burns, Oregon (PhenoCam-1). The top panel (a) shows the GEE image fusion's NDVI-derived time series, model, and phenometrics. The bottom panel (b) shows the PhenoCam's G _{cc} -derived time series, model, and phenometrics. For each main panel (i.e., a and b), the three subpanels follow the labeling and symbology conventions of Figure 2.3..... 37
2.9	The SEFR transects sampled in open-pine sites for the 2017 growing season. The top panel shows percent cover by functional group at the four sites (transects). The bottom panel shows the proportion of vegetation in each phase by functional group. In both panels, vertical lines show the phenometrics estimated from the GEE image fusion's NDVI time-series, including start of green-up (SOG), start of season (SOS), end of season (EOS), and dormancy (Dorm). In both panels, lines may overlap for functional groups with little aerial cover (i.e., those with cover recorded in the 0-10 % class or low proportion in a given phase; e.g., shrub in transect 5 or, at day of year 100 in transect 5, grass in the cured phase)..... 39

LIST OF FIGURES (Continued)

<u>Figure</u>	<u>Page</u>
<p>2.10 The SEFR transects sampled in grassland sites for the 2017 growing season. The top panel shows percent cover by functional group at the four sites (transects). The bottom panel shows the proportion of vegetation in each phase by functional group. In both panels, vertical lines show the phenometrics estimated from the GEE image fusion’s NDVI time-series, including start of green-up (SOG), start of season (SOS), end of season (EOS), and dormancy (Dorm). In both panels, lines may overlap for functional groups with little aerial cover (i.e., those with cover recorded in the 0-10 % class or low proportion in a given phase; e.g., shrub in transect 5 or, at day of year 100 in transect 5, grass in the cured phase).....</p>	40
<p>3.1 Location of ventenata presence and absence observations throughout the Blue Mountains Ecoregion.....</p>	54
<p>3.2 ROC curves for each of the (a) hybrid, (b) bioclimatic, and (c) phenology models. The bold blue line shows the mean ROC curve from the k-fold (k=10) cross validation. The light blue lines show the ROC curve for each fold and the grey band shows the variation in the ROC curves. The dashed line-of-equality represents an AUC of 0.5 and is interpreted as performance of a model with random predictions</p>	60
<p>3.3 Importance and rank of the 48 predictors included in the hybrid model. Descriptions of the individual covariate codes can be found in Appendix E</p>	64
<p>3.4 Partial dependence plots from the hybrid model indicating the average relationship between the probability of ventenata presence and the predictors. Tick marks in the rug plot along the x axis indicate deciles from the training dataset. Appendix E provides a description of each predictor. Units of the x-axes include a) NDVI, b) day of year, c) degrees Celsius, d) degrees Celsius, e) degrees Celsius, and f) millimeters.....</p>	65

LIST OF FIGURES (Continued)

<u>Figure</u>		<u>Page</u>
3.5	Predictions (probability) from the hybrid model (top panel), the bioclimatic model (middle panel), and the phenology model (bottom panel). The color ramp is split at the presence threshold (i.e., the threshold that maximizes kappa; hybrid=0.58, bioclimatic=0.73, phenology=0.7), where areas above the threshold (presence) are colored in yellow to red and areas below the threshold (absence) are colored in grey to black. Masked areas are outside the BME or are presumed to be currently uninhabitable due to high elevation, high forest canopy cover, or perennial water	67
3.6	The difference between probability where the bioclimatic and phenology models are subtracted from the hybrid model (Top panel). Blue colors indicate that the hybrid model predicts higher probability while red colors indicate that the bioclimatic or phenology model predict higher probability. Predicted cheatgrass presence within a subset of the BME showing the similarity of spatial patterns to the difference between the hybrid and phenology model (Bottom panel).....	69
3.7	PNV types with greater than 0.1 percent area of ventenata and greater than 0.5 percent area of the BME. The invaded area (orange) and uninvaded area (grey), according to the hybrid model (greater than 0.58 probability), is shown for each PNV type. The percent of each PNV type invaded by ventenata is reported as an inset. PNV types are presented in descending order by proportion of total invaded area.....	71
4.1	The Blue Mountains Ecoregion with case-study areas and wildfires that occurred in Oregon and Washington between 2006 and 2017. Wildfire perimeters were provided by the Monitoring Trends in Burn Severity database (Eidenshink et al., 2007)	84

LIST OF FIGURES (Continued)

<u>Figure</u>	<u>Page</u>
<p>4.2 Weather similarity between the model development period (2017) and the year selected for historic ventenata prediction (2006); the years 2017 and 2006 are shaded by grey bands in each panel. The top two panels show the monthly Palmer Drought Severity Index (PDSI) from 2000 through 2017 within the two climate divisions covering approximately 80 percent of the BME (3507, 3508). Climate division 3507 covers the western BME, and climate division 3508 covers the central to northeastern BME. Positive PDSI values (blue) indicate that the region is in a wet period, while negative values (red) indicate that region is experiencing drought. The bottom panel depicts the multivariate Euclidean distance (MVD) from 2017 to each year between 2000 and 2016 based on weather data from the five RAWS stations. Smaller MVD values indicate greater similarity with weather conditions in 2017</p>	87
<p>4.3 Contraction, expansion, and persistence of ventenata populations from 2006 to 2017 throughout the BME. In A, the categorical change in ventenata’s distribution is mapped across the region. In B-D, the distribution of change in phenometrics between 2006 and 2017 is shown for the start-of-greenup (B), minimum-NDVI (C), and end-of-season (D), where change is calculated as 2017 value – 2006 value. The density plots in B-D are scaled to show equal area for visibility. Positive values indicate that: vegetation greening was later in 2017 (B), minimum-NDVI was higher in 2017 (C), end-of-season was later in 2017 (D)</p>	95
<p>4.4 Elevation summaries by expansion, persistence, and contraction. The top left panel (A) shows the total invaded area within the context of the elevation of the Blue Mountains Ecoregion, while the bottom left panel (B) shows the area associated with each of the invasion classes across the elevation gradient. The right panel (C) shows the proportion of the invaded area for each of the invasion classes.</p>	97
<p>4.5 Summary of the difference in probability between 2017 and 2006 for the potential natural vegetation (PNV) subzones presented in Table 4.1. Boxplot summaries of the probability differences include the median (middle line segment), the 25th and 75th percentile (the upper and lower hinges), and the 5th and 95th percentile (the whiskers). The heatmap on the right shows the total area per PNV subzone within the study area of the BME</p>	100

LIST OF FIGURES (Continued)

<u>Figure</u>	<u>Page</u>
<p>4.6 Summaries by fire-veg group for the mean percent-change in the probability of ventenata within wildfires and non-wildfire areas. Boxplot summaries include the median (middle line segment), the 25th and 75th percentile (the upper and lower hinges), and the 5th and 95th percentile (the whiskers).....</p>	101
<p>4.7 Summary of the median and IQR of burn severity (RdNBR) within wildfires by change-class (percent-change in probability of ventenata) and fire-veg group. For example, in the mixed/woodland group and median statistic, boxplots summaries for the > 200% change-class are based on the median of RdNBR in the > 200% change-class for each wildfire in that fire-veg group. Boxplot summaries include the median (middle line segment), the 25th and 75th percentile (the upper and lower hinges), and the 5th and 95th percentile (the whiskers)</p>	103
<p>4.8 Heatmap of the average (mean) difference in the median and IQR of burn severity (RdNBR) between change-classes (percent-change in probability of ventenata) within wildfires for each fire-veg group. For example, in the dry-forest group and median statistic, the right-most column of the heatmap shows the average difference in the median RdNBR between the > 200% change-class and progressively smaller change-classes (i.e., lower percent-change in probability) moving down the column, where the greatest average difference in median burn severity is between the >200% and the < -50% change-classes (differences in this cell are calculated at the wildfire-level first, before the average taken at the fire-veg level)</p>	105
<p>4.9 Change in vegetation (A-B), minimum-NDVI (C), and ventenata predictions (D; percent-change in ventenata probability) across the Starkey Experimental Forest and Range (SEFR) from 2006 to 2017. The percent-change in probability of ventenata is shown for all of SEFR in the right panel, with a dark-grey square corresponding to the location of the zoomed-in panels A-D. Change in vegetation for the nearest dates to 2006 and 2017 are shown as NAIP imagery from 2005 (A) and 2016 (B)</p>	107

LIST OF FIGURES (Continued)

<u>Figure</u>		<u>Page</u>
4.10	Change in ventenata's distribution across the Starkey Experimental Forest and Range (right panel) between 2006 and 2017, illustrated by contraction, expansion, and persistence of ventenata populations. In the right panel, the location of panels A-B are indicated by the dark-grey squares. The example in panel A illustrates how contraction generally occurred along the border of forest openings close to persistent patches. The location of panel B is the same as Figure 4.9, panels A-D. In the background of all images is a grey-toned NAIP image from 2016 showing the configuration of forested and non-forested areas within the SEFR.....	108
4.11	The Corner Creek Complex wildfire's burn perimeter, including NAIP imagery from 2016 (A), burn severity (B; RdNBR), and the change in ventenata's distribution between 2006 and 2017 (C-D). Panel C shows ventenata expansion, contraction, and persistence, while panel D shows percent-change in ventenata probability (percent-change in probability between 2006 and 2017). White-area within the burn perimeter indicates locations masked from the analysis because the elevation was above 1,829 m.....	110

LIST OF TABLES

<u>Table</u>		<u>Page</u>
2.1	Image evaluation results for each DOY and scene combination. A total of 5,000 pixels were sampled from each image to calculate bias, correlation, RMSPE, and SRB. All pixels were used to calculate the variance of each image. Italicized values inside parentheses correspond to the ESTARFM results while the GEE image fusion results are in a regular typeface	33
2.2	Phenometrics (DOY) estimated at each of the PhenoCam sites	36
3.1	RF model parameters determined through grid search.....	58
3.2	Mean and IQR of evaluation metrics showing the overall model performance for each of the three models. Threshold dependent metrics were calculated based on thresholds of 0.58 (hybrid), 0.73 (bioclimatic), and 0.7 (phenology).....	61
3.3	Summary of model performance by elevation class with sample size, ventenata prevalence, and the percent area of the Blue Mountains Ecoregion. Models are abbreviated as HY (hybrid), BIO (bioclimatic), and PHEN (phenology). In some cases, sensitivity could not be calculated because the class did not have any presence observations. Interquartile range of accuracy, sensitivity, and specificity are in parenthesis	62
3.4	Summary of total area and percentiles of elevation for six probability classes for the hybrid model. The probability range above and below the threshold that maximizes kappa was split into three equal classes.....	70
4.1	Regional change in ventenata area for potential natural vegetation (PNV) subzones in which ventenata occupied greater than one percent of the PNV in 2017. PNV subzones are sorted in descending order by the percent occupied by ventenata in 2017	99
4.2	Number of wildfires, median fire size by fire-veg group, and number of non-wildfire samples	102

LIST OF APPENDICES

<u>Appendix</u>	<u>Page</u>
A. Landsat and MODIS Metadata.....	146
B. Spatio-temporal Image Fusion Evaluation.....	149
C. PhenoCam Time Series Comparisons	155
D. Starkey Experimental Forest and Range Mixed Conifer Phenology	159
E. Phenology, Climate, Soils, and Topography Predictors	161
F. Bioclimatic and Phenology Model Importance Plots.....	163
G. Hybrid Model Performance by Potential Natural Vegetation Class.....	164
H. Spatial Patterns of Ventenata Probability Difference and Percent Probability Difference.....	166

LIST OF APPENDIX FIGURES

<u>Figure</u>	<u>Page</u>
A.1 The percent of MODIS pixels masked by date within the bounds of each Landsat WRS-2 scene used in the image fusion and LSP estimation. MODIS pixels were masked for snow and cloud cover. Vertical orange lines indicate the dates of the Landsat images paired with MODIS images (see Table A.1 for Landsat specific information).....	146
B.1. Hex grid of the true Landsat NDVI vs. the GEE image fusion NDVI for path 43/ row 29 on DOY 252. See Table 2.1 for further evaluation details.....	150
B.2. Hex grid of the true Landsat NDVI vs. the GEE image fusion NDVI for path 43/ row 29 on DOY 206. See Table 2.1 for further evaluation details.....	151
B.3. Hex grid of the true Landsat NDVI vs. the GEE image fusion NDVI for path 43/ row 30 on DOY 94. See Table 2.1 for further evaluation details.....	152
B.4. Hex grid of the true Landsat NDVI vs. the GEE image fusion NDVI for path 43/ row 30 on DOY 206. See Table 2.1 for further evaluation details.....	153
B.5. Hex grid of the true Landsat NDVI vs. the GEE image fusion NDVI for path 43/ row 30 on DOY 222. See Table 2.1 for further evaluation details.....	154
C.1. Comparison of the time series and model fit for the conifer PhenoCam site near Sisters, Oregon (PhenoCam-2). The top panel (a) shows the image fusion NDVI-derived time series, model, and phenometrics. The bottom panel (b) shows the PhenoCam G_{cc} -derived time series, model, and phenometrics. For each main panel (e.g., a and b), the three subpanels follow the labeling and symbology conventions of Figure 2.3	156
C.2. Comparison of the time series and model fit for the agricultural PhenoCam site near Pullman, Washington (PhenoCam-4). The top panel (a) shows the GEE image fusion's NDVI-derived time series, model, and phenometrics. The bottom panel (b) shows the PhenoCam's G_{cc} -derived time series, model, and phenometrics. For each main panel (i.e., a and b), the three subpanels follow the labeling and symbology conventions of Figure 2.3	157

LIST OF APPENDIX FIGURES (Continued)

<u>Figure</u>	<u>Page</u>
<p>C.3. Comparison of the time series and model fit for the conifer PhenoCam site near Sisters, Oregon (PhenoCam-3). The top panel (a) shows the GEE image fusion’s NDVI-derived time series, model, and phenometrics. The bottom panel (b) shows the PhenoCam’s G_{cc}-derived time series, model, and phenometrics. For each main panel (i.e., a and b), the three subpanels follow the labeling and symbology conventions of Figure 2.3</p>	158
<p>D.1. The SEFR transects sampled in mixed conifer sites for the 2017 growing season. The top panel shows percent cover by functional group at the four sites (transects). The bottom panel shows the proportion of vegetation in each phase by functional group. In both panels, vertical lines show the phenometrics estimated from the image-fusion based NDVI time-series, including start of green-up (SOG), start of season (SOS), end of season (EOS), and dormancy (Dorm).....</p>	159
<p>F.1. Variable importance and rank of the 32 predictors in the bioclimatic model</p>	163
<p>F.2. Variable importance and rank of the 16 predictors in the phenology model</p>	163
<p>H.1. Google satellite image showing the broad scale spatial patterns of forested and non-forested areas within the Blue Mountains Ecoregion</p>	166
<p>H.2. Regional change in ventenata probability between 2006 and 2017. Positive values indicate that the probability was higher in 2017 than 2006</p>	167

LIST OF APPENDIX TABLES

<u>Table</u>	<u>Page</u>
A.1 All Landsat images used in the GEE image fusion and evaluation. Images used to evaluate the GEE image fusion and locally run ESTARFM algorithm are indicated with bold typeface	147
E.1. Complete list of predictors used to model the presence and absence of ventenata.....	161
G.1. Model performance per potential natural vegetation class. HY = hybrid, BIO = bioclimatic, PHEN = phenology.....	164
G.2. Composition of the BME by PNV class and their representation in the ventenata field data set.....	165

1 INTRODUCTION

1.1 Background

Before the development of transportation technology, organisms were limited in their range by geographic and environmental constraints. In recent decades, as globalization has expanded trade, species' movement outside of their native range has resulted in an increase in biological invasions (Levine and D'Antonio, 2003). The global consequences of species invasion have become increasingly apparent as the abundance of invasive species has increased. Species invasion results in biodiversity decline (Tilman et al., 2017), loss of ecosystem services (Boyd et al., 2013), economic costs (Pimentel et al., 2005), and substantial impacts to human livelihood (Pejchar and Mooney, 2009; Shackleton et al., 2019). The numerous potential outcomes of species invasion in concert with climate change are also major concerns and sources of uncertainty (Hellmann et al., 2008).

Forest and rangeland resources in the United States have suffered, sometimes severely, from the introduction of nonnative species. One classic example of the impact of biological invasions on the forestry sector is the introduction of the chestnut blight fungus (*Cryphonectria parasitica*) and the subsequent decline of the American chestnut (*Castanea dentata*), which historically served as an important source of high-value timber and mast for wildlife (Hepting, 1974). Biological invasion of plant species is also problematic to forest management and can hinder natural and artificial regeneration processes. Accordingly, forest stands are routinely treated mechanically or chemically in the early stages of forest regeneration to reduce the competitive effects of herbaceous vegetation, including invasive plants (Wagner et al., 2006). Concerning rangelands, loss in range productivity and ecosystem integrity has been a widely documented result of annual grass invasion (Brooks et al., 2016; Knapp, 1996). Semi-arid and arid shrublands of the western United States have experienced some of the greatest ecosystem transformations from annual grasses, such as *Bromus tectorum*, which have altered

the natural disturbance regime by increasing fire frequency (Brooks et al., 2004; D'Antonio and Vitousek, 1992). Although grass invasion has historically been more common in arid landscapes, the topic of grass invasion in and around forests has also recently drawn attention as the abundance of species like *Microstegium vimineum* and *Ventenata dubia* has increased in these ecosystems (Flory et al., 2015; Kerns et al., 2020).

Preventing and mitigating the impacts of species invasion is a complex topic that requires a multifaceted approach. When approached from the preventative perspective, the vectors that contribute to species transport and the species likely to become problematic are important factors to address. The movement pathways by which species may be transported are diverse but include intentional introductions or unintentional transport as contaminants or stowaways in commodities like agricultural products (Hulme, 2011). Accordingly, governments worldwide have worked to develop strategies to prevent species movement with approaches ranging from international treaties to inspections at ports of entry (Elferink and van der Weijden, 2011). Determining which species are likely to become invasive in a new range is a challenging task. While there is limited information known to be important in determining invasion potential, substantial progress is being made in developing preventative risk assessments (Pyšek and Richardson, 2010). Once species have arrived within a new range, early detection and rapid response efforts are the best methods to prevent the adverse effects that species may bring. However, there are obvious challenges with early detection as incipient invaders are typically rare, making detection more challenging. Regardless of the preventative efforts made to restrict species introduction, new species are likely to be introduced.

Risk assessments of established nonnative species are critical sources of information that can improve policy and management decisions. One approach to assessing the risk of invasion across broad spatial scales is species distribution modeling (Peterson, 2003). Species distribution models (SDMs) aim to map the areas

likely to be suitable to a species by quantifying the ecological niche of a species using correlative or mechanistic modeling approaches (Guisan and Thuiller, 2005). While SDMs can provide important information regarding the invasion risk across an uninvaded region, there are numerous challenges associated with invasive species SDMs related to the process of invasion and the characteristics of the invading species. Regardless of the challenges associated using SDMs to characterize potential species distributions, the value of these and other methods of mapping species distributions are widely recognized (Latombe et al., 2017).

In recent years, advances in technology and modeling methods have improved our ability to capture and characterize both the potential (SDM-based) and actual species distribution (Jetz et al., 2019). Remote sensing data has been incorporated into SDMs as a way to, directly and indirectly, quantify environmental conditions that influence species (He et al., 2015). While remote sensing has been shown to improve some SDMs in mapping species distributions, there are questions about whether the mapped distribution represents the potential or actual species distribution. Some argue that by including remote sensing data, models are more representative of the present species distribution because the target species' unique spectral or temporal characteristics are captured by remote sensing (Bradley et al., 2012). This is particularly true for sessile species like plants. The use of remote sensing in studying species distributions is appealing both from the standpoint of the improvements that it can provide in mapping present species distributions and because the data archive can span decades (Wulder et al., 2016), allowing for monitoring of the progression of invasion.

After nonnative species naturalize, there can be a lag before widespread dispersal and negative ecological and economic impacts occur (Aikio et al., 2010). This lag time can mean that resources are not devoted to monitoring and assessing species until after they have gained a strong foothold and eradication is no longer a feasible solution. In these situations, remote sensing can link the past and present

state and distribution of invasive species populations. Connecting the stages of the invasion through these means can provide valuable information that may reveal local or regional patterns and trends in spread (Santos et al., 2016). Quantifying basic information about the progression of an invasion can allow for better-informed decision-making and more targeted field-based studies, while land managers and policy makers grapple with how to respond to the presence of a novel species.

A prime candidate for this type of spatio-temporal invasion analysis is *ventenata* (*Ventenata dubia*), also known as North Africa grass, or wiregrass. *Ventenata* was first documented in eastern Washington state in the early 1950's (Barkworth et al., 1993) and has since spread through much of the western United States (Scheinost et al., 2008). *Ventenata* originated in Mediterranean Eurasia and, like many other invasive annual grass species present in the western United States, exhibits annual growth patterns that differ from the native vegetation in the region. *Ventenata* typically begins its growth cycle in the late fall or early winter and completes senescence and fruit ripening by early to mid-summer (Wallace et al., 2015). Initially problematic in hay production systems (Wallace et al., 2015), *ventenata* has since spread to undeveloped areas and has become abundant in some grasslands (Endress et al., 2020), shrublands (Jones et al., 2018), and dry forest ecosystems (Tortorelli et al., 2020). Due to the shared characteristics between *ventenata* and other invasive annual grass species, like cheatgrass (*Bromus tectorum*), interest has arisen about the potential of this species to negatively impact plant communities and alter fire regimes (Kerns et al., 2020).

1.2 Remote Sensing Methods for Invasive Species Mapping

A wide range of methods have used with remotely sensed data to identify the unique properties that differentiate plant species from their surrounding biotic and abiotic setting. Each approach used to identify species relies on characteristics of the target species, the biotic and abiotic factors related to the ecosystem of interest, and the availability of data that adequately captures the necessary

information. Successful species detection is heavily reliant on an invasive species' biological and structural traits (Underwood et al., 2007). In some cases, the traits that make invasive species successful can differentiate them from native vegetation. For instance, the winter annual grass cheatgrass (*Bromus tectorum*) has a competitive advantage over native species in the Great Basin because of its earlier phenological cycle, which can be detected using satellite-image time series (Bradley et al., 2017).

Species detection has relied on spectral, structural, textural, and phenological properties (Bradley, 2014; Gavier-Pizarro et al., 2012; Huang and Asner, 2009; Underwood et al., 2007). Pigmentation, leaf chemistry, and leaf water content have helped distinguish some exotic plant species with spectral information (Andrew and Ustin, 2008; Asner et al., 2008; Galvão et al., 2005; Große-Stoltenberg et al., 2016; Ustin et al., 2002). Differences in pigmentation can be sensed from either leaf or flowering pigments and are typically related to chlorophyll, carotenoid, anthocyanin, and lignin-cellulose content (Bradley, 2014; Galvão et al., 2005). Spectrally based detection generally requires detailed information in the spectral domain, and therefore, hyperspectral sensors are typically the most useful when trying to characterize the properties of invasive species. However, spectrally-based detection can become challenging when applied across vast heterogeneous landscapes because species diversity increases with scale. With greater species diversity there is an increased possibility that a native species will contain the same spectral properties as an invasive species (Andrew and Ustin, 2008).

Texture or object-based techniques have also served to successfully detect invasive species. These techniques require that patches of the target species be larger than the grain size of the data. With this approach, species are typically detected based on unique shapes or patterns identified by visual interpretation or by applying automated techniques using the variation within a multi-pixel moving window (Blaschke, 2010; Bradley, 2014). Some of the more successful

implementations of this kind of technique are related to tracking tree invasions into shrublands or grasslands (Weisberg et al., 2007). However, texture or object-based methods have not been widely applied as they can require high spatial resolution, heavy human intervention in image interpretation, or produce substantial errors when using automated classification methods (Pearlstone et al., 2005).

Phenological patterns have been useful for detecting a variety of invasive species. Phenology has been used to distinguish lantana (*Lantana camara* L.) within a deciduous forest in India (Kimothi and Dasari, 2010), identify glossy privet (*Ligustrum lucidum*) from surrounding forest in Argentina (Hoyos et al., 2010), differentiate gamba grass (*Andropogon gayanus*) from senesced native grasses in Australia (Petty et al., 2012), and quantify the distribution and cover percentage of cheatgrass in the Great Basin (Boyte and Wylie, 2016; Bradley et al., 2017; Pastick et al., 2020; Peterson, 2005). Phenological characteristics have been assessed with several methods and data sources. These measurements may include timing and rate of green-up, start of season, maturity, peak greenness, timing and rate of senescence, end of season, dormancy, and season duration (Elmore et al., 2005; Fisher et al., 2006; Jönsson and Eklundh, 2002; Richardson et al., 2018a; Zhang et al., 2003). In some cases, specific metrics related to phenological cycles may not even be necessary if the imagery is acquired at the right time (Kimothi and Dasari 2010). Both lantana and gamba grass were identified in this way because imagery was acquired at a time when native species were dormant but the invasive species were still actively growing. However, in most cases where phenological characteristics are used to differentiate invasive species, one or more of the phenological metrics are estimated.

Capitalizing on multiple remote sensing sources can also provide a means of detection for some species. Structural and spectral properties in combination have helped to key in on coniferous and broad leaf tree species (Cho et al., 2012; Dalponte et al., 2012; Hill and Thomson, 2005; Mäyrä et al., 2021; Wang et al.,

2018). In one study, invasive trees on the Hawaiian Islands were distinguished from native tree species with hyperspectral and LiDAR data. The invasive trees were detectable because of both spectral characteristics related to leaf nitrogen content and structural features related to crown shape and size (Asner et al., 2008). Other sensor combinations may provide complementary spectral and spatial data useful when distinguishing invasive plants based on phenology (Walker et al., 2014). While much progress has been made in detecting and mapping invasive plants using remote sensing, there remains room for improvement in processing and modeling techniques. Furthermore, there are many cases where species-level detection based on remote sensing alone may not be feasible.

1.3 Research Overview

In the following chapters, this dissertation explores the use of satellite remote sensing for detecting, mapping, and examining spatial patterns and relationships of the *ventenata* invasion over an 11-year period. This research is centered around the landscapes of the interior Pacific Northwest, with Chapters 3 and 4 focus exclusively on the Blue Mountains Ecoregion (BME) found in eastern Oregon, southeastern Washington, and west central Idaho. This region contains a variety of developed and undeveloped land cover types, all of which have a long history of human influence in the form of agriculture, grazing, fire, and/or forest management. Given the wide range of environmental conditions suitable to *ventenata*, I examine natural ecosystems ranging from remnant patches of Palouse Prairie to sagebrush steppe shrublands to dry coniferous forests of pine and fir species.

In Chapter 2, I examine the potential of satellite image time series for capturing phenological patterns of vegetation development across a heterogeneous landscape in the interior Pacific Northwest. The estimation of phenology with satellite imagery relies on the temporal coverage of satellite observations across the growing season (Beck et al., 2006). This requirement can limit the use of some

moderate- and high-resolution data because they may either lack the temporal coverage required to characterize annual phenology or they may lack observations at critical times of the growing season. While previous mapping endeavors have been successful at using 250 to 500 m MODIS imagery (Moderate Resolution Imaging Spectroradiometer) to map cheatgrass (Boyte and Wylie, 2016; Bradley et al., 2017), use of these data poses multiple issues specifically related to the characteristics of ventenata invasion and spatial configuration of the vegetation communities in my study region. The first critical issue with lower spatial resolution data is that the area associated with an individual pixel is relatively large. This may limit the ability of these sensors to detect smaller populations of ventenata. Additionally, the forest and non-forest mosaic composition and spatial configuration is highly fragmented and may prevent the detection of ventenata in smaller forest openings as conifer cover could dominate the signal received by the sensor. To address these spatial and temporal issues, I implement a spatio-temporal image fusion algorithm in a cloud computing environment to capitalize on the strengths of Landsat (30 m spatial resolution) and MODIS data. I use the resulting 30 m time series to estimate land surface phenology and evaluate the quality of the land surface phenology estimates using near-surface sensors and field observations.

In Chapter 3, I explore the utility of the land surface phenology estimates I develop in Chapter 2 in detecting and mapping the present (2017) distribution of ventenata throughout the BME. While similar in some respects to other invasive annual grass species (e.g., cheatgrass), previous research on ventenata has identified that ventenata occupies unique environmental niche space (Tortorelli et al., 2020). Therefore, I examine whether the inclusion of environmental predictors improves the phenological models' ability to detect populations of ventenata. I develop three models to test and evaluate the differences between using phenology, environmental predictors, and a combination of phenology and environmental predictors.

In Chapter 4, I examine the progression of *ventenata*'s invasion in the BME over an 11-year period. The main objective of this research is to determine the spatio-temporal attributes of the invasion in recent past. Such assessment can provide land managers with critical information for decision-making and resource prioritization and provide guidance for future research endeavors. To accomplish these goals, I apply a model I develop in Chapter 3 to predict the distribution of *ventenata* in 2006 and 2017. From these predictions, I evaluate how spatial patterns and biophysical associations changed over 11 years, focusing on the changes associated with elevation, potential natural vegetation, and spread patterns. I also investigate the impacts of wildfire on the *ventenata* invasion by comparing areas with and without wildfire and examining the relationship between burn severity and *ventenata*.

2 SPATIOTEMPORAL IMAGE FUSION IN GOOGLE EARTH ENGINE FOR ANNUAL ESTIMATES OF LAND SURFACE PHENOLOGY IN A HETEROGENEOUS LANDSCAPE

Ty C. Nietupski, Robert E. Kennedy, Hailemariam Temesgen, Becky K. Kerns

International Journal of Applied Earth Observation and Geoinformation

P.O. Box 217

7500 AE Enschede, NL

Volume 99, July 2021

2.1 Abstract

Currently, quantifying phenology at landscape to regional scales is not feasible with field data or near-surface sensors. Consequently, the spatial and temporal complexity of phenology has been assessed using satellite-based estimates (land surface phenology, LSP). While estimates from Moderate Resolution Imaging Spectroradiometer (MODIS) capture intraannual patterns of phenology, they have relatively low spatial resolution. Estimates from sensors like Landsat capture finer spatial detail but are often limited by Landsat's temporal resolution. We implemented a spatio-temporal image fusion method on the Google Earth Engine (GEE) platform and used the resulting dense time series of images to estimate intraannual LSP at 30 m resolution. We utilized Landsat 8 surface reflectance and MODIS NBAR (Nadir BRDF-Adjusted Reflectance; MCD43A4) images from 2016 and 2017 in the interior Pacific Northwest of the United States. Images predicted from the GEE image fusion algorithm were evaluated with true Landsat observations and compared with the accuracy achieved by executing the original ESTARFM algorithm. Excluding snow and cloud obscured observations, the algorithm produced approximately 215 observations per 30 m pixel in 2017. Root mean squared prediction error (RMSPE) of Normalized Difference Vegetation Index (NDVI) for the GEE predicted images ranged from 0.032 to 0.066. The RMSPE for the original ESTARFM predicted images ranged from 0.027 to 0.064. Phenometric estimates were evaluated with near-surface sensors (PhenoCams) in shrubland, conifer, and agricultural sites and field observations of phenology in grassland, open-pine, and mixed-conifer sites. Although phenometric estimates were dissimilar at all PhenoCam sites, the general temporal pattern of the GEE image fusion and PhenoCam time series was often similar. The start of season derived from the GEE image fusion time series had closer correspondence to the PhenoCam-derived start of season at the shrubland site (13 days) than the agriculture and conifer sites. The end of season was closest at one of the conifer sites and the agriculture site (22 and 31 days, respectively). Trends of some of the field-based phenology observations

aligned with phenometrics estimated from the image fusion time series. At the grassland and open-pine field sites, the phenometrics from GEE image fusion were associated with phenophase trends of dominant plant functional types. Though characterizing LSP within the interior Pacific Northwest remains a challenge, this study demonstrates that image fusion implemented in GEE can produce a densified time series capable of capturing seasonal trends in NDVI related to vegetation phenology, which can be used to estimate intraannual phenometrics.

2.2 Introduction

The study of vegetation phenology provides important information about past, current, and potential future ecosystem states. Variation in the timing of phenology results from temperature, precipitation, plant community composition and condition, genetic traits, and soil characteristics (Wolkovich et al., 2014), giving it the capacity to serve as an indicator of climate change (Richardson et al., 2013). Phenology also influences many processes, including carbon flux (Forkel et al., 2016; Richardson et al., 2012), wildfire activity (Westerling et al., 2006), crop production (Anwar et al., 2015), and wildlife populations (Morellato et al., 2016). Moreover, certain species' phenology can drive plant community composition, with invasive species being of great concern (Colautti et al., 2017). However, monitoring phenology with traditional field-based methods is expensive and limited to small spatial extents (Richardson et al., 2009).

The availability of satellite-imagery time series has allowed for phenological observation across previously unattainable extents, expanding our understanding of the relationship between phenology and the environment. Characterization of the temporal patterns of electromagnetic reflectance with satellite imagery is referred to as land surface phenology (LSP; de Beurs and Henebry, 2004). However, the spatial resolution of LSP does not always match the scale at which vegetation communities vary. Moreover, the phenological metrics (e.g., start of season) extracted by these means do not necessarily represent the same stages that might be recorded at a field site (e.g., leaf emergence) and can be influenced by abiotic processes like snow melt and soil-moisture fluctuation. Consequently, LSP does not entirely fit with the ecological definition of phenology, which is “the study of the timing of recurring biological events, the causes of their timing with regard to biotic and abiotic forces, and the interrelation among phases of the same or different species” (Lieth, 1974). This inconsistency makes the validation of LSP challenging (Nijland et al., 2016; Richardson et al., 2018b). Quantifying LSP at more meaningful

spatial and temporal scales may be one potential solution to some discrepancies between LSP estimates and ground-based observations of phenology.

A major challenge in choosing satellite data for LSP is the tradeoff between revisit frequency and spatial detail. Satellites like MODIS (Moderate Resolution Imaging Spectroradiometer), AVHRR (Advanced Very High Resolution Radiometer), and VIIRS (Visible Infrared Imaging Radiometer Suite) identify fine-grained temporal signals of plant development owing to their daily revisit frequency (White et al., 1997; Zhang et al., 2018, 2003). These revisit frequencies allow for intraannual estimates of phenology. However, the relatively low spatial resolution (e.g., 250 m – 1 km for MODIS) of these satellites results in a highly mixed composition of vegetation, reducing the utility of LSP estimates for studying phenomena occurring at a fine scale. This is particularly problematic in landscapes where resources are variably dispersed leading to heterogeneous vegetation patterns.

Other satellites, like the Landsat missions, have finer spatial resolutions (30 m) but typically lack the temporal resolution to capture fine-scale intraannual patterns of LSP (Fisher et al., 2006; Jönsson and Eklundh, 2002). To address this deficiency, some have assessed long-term phenology estimates by aggregating multiple years of data (Melaas et al., 2013), ensuring adequate observations across the growing season. Melaas et al. (2016) used such methods to correct the phenological estimate for individual years by adjusting the long-term mean curve based on individual years' anomalies. More recently, others have developed methods to estimate LSP at 30 m using Landsat and Sentinel-2 imagery (Bolton et al., 2020; Gao et al., 2020; Zhang et al., 2020). Although the utilization of Landsat and Sentinel-2 shows promise moving forward, methods focused on leveraging older platforms enable the investigation of phenological changes that have occurred over the last 20 or more years.

Methods that blend data from these sensors (i.e., spatio-temporal image fusion) have been developed to capture the complementary strengths of Landsat

and MODIS. These algorithms leverage the temporal frequency of MODIS (daily) and the spatial resolution of Landsat (30 m) to predict imagery at 30 m resolution for times when observations are unavailable from Landsat. There have been many new fusion methods developed in the last decade (see Belgiu and Stein, 2019). One of the first methods developed for this purpose was the Spatio-temporal Adaptive Reflectance Fusion Model (STARFM; Gao et al., 2006). STARFM uses pairs of Landsat and MODIS images to predict the Landsat reflectance at a time where only MODIS is available. This method performs well when change in the spatial dimension is gradual but is less effective when change is abrupt (Emelyanova et al., 2013; Gao et al., 2006; Hilker et al., 2009b). Other variations of spatio-temporal image fusion were developed to address issues with STARFM, including STAARCH (Spatial Temporal Adaptive Algorithm for mapping Reflectance Change) which improved the method for detecting disturbances (Hilker et al., 2009a) and ESTARFM (Enhanced STARFM; Zhu et al., 2010) which improved predictions in heterogenous regions (Emelyanova et al., 2013).

The STARFM algorithm has been employed to estimate LSP in a limited number of instances (Coops et al., 2012; Gao et al., 2017; Liang et al., 2014; Walker et al., 2014). Walker et al. (2014) reported that the inclusion of STARFM-fused images helped improve LSP estimates in semi-arid ecosystems. Cropland LSP was also recently assessed with STARFM and Timesat (Jönsson and Eklundh, 2004) by Gao et al. (2017). They extracted various phenometrics (i.e., phenological transition dates) from the time series and evaluated these estimates with crop progress reports. There remains a need to execute and evaluate high-spatial and high-temporal LSP across expansive, heterogenous natural landscapes.

While image fusion methods are promising as a means of filling in missing or noisy Landsat observations, these methods are computationally expensive (Gao et al., 2017; Rao et al., 2015). The development of cloud computing platforms like Google Earth Engine (GEE; Gorelick et al., 2017) may allow for the development and

deployment of image fusion techniques, increasing their availability and reducing the onsite processing infrastructure and processing time. One such method was recently developed and tested using GEE (Moreno-Martínez et al., 2020), demonstrating the potential for this type of application of the GEE platform.

In this study, we developed and evaluated methods for estimating LSP in a heterogenous region of the interior Pacific Northwest of the United States. This research had three primary objectives: 1) develop an ESTARFM-like approach to spatio-temporal image fusion that is capable of running on a cloud-computing platform (GEE); 2) process and assemble a time series of daily 30 m imagery and evaluate the quality of fused images across the growing season; and 3) estimate LSP and assess the similarity of LSP estimates to estimates from near-surface cameras (PhenoCams) and ground-based observations from field data. Phenometrics were evaluated at varying spatial scales and with multiple datasets to account for potential discrepancies in scale and the method of phenological observation.

2.3 Methods

The estimation of LSP with high-spatial and high-temporal resolution was accomplished with a two-phase process. First, a high-resolution time series was assembled from Landsat observations and MODIS-derived predictions with an ESTARFM-like algorithm implemented on GEE (hereafter, GEE image fusion). The time series created with the GEE image fusion was then used to estimate phenometrics with a double-logistic smoothing method where transition dates were extracted based on rates of change and curve inflection points.

2.3.1 Study Area

The interior Pacific Northwest region is composed of a variety of natural and human-derived land cover types that are well suited to testing the methods of this research (Figure 2.1). The region includes parts of the Columbia Plateau, Blue Mountains, and Northern Basin and Range Ecoregions, including the eastern edge of

the Eastern Cascades Slopes and Foothills (Omernik, 1987). The region has an arid to semi-arid climate resulting from the Cascade Range's rain-shadow, which interacts with numerous mountain ranges, canyons, and valleys to produce a mosaic of forest, grassland, and shrubland plant communities. The marine-influenced continental climate is characterized by warm, dry summers and cold winters, during which most of the annual precipitation occurs. On average, total annual precipitation for this region ranged from 16 to 277 cm (mean of 43 cm) and mean annual temperature ranged from -1 to 13 °C (mean of 8 °C) between 1981 and 2010 (PRISM Climate Group, 2012).

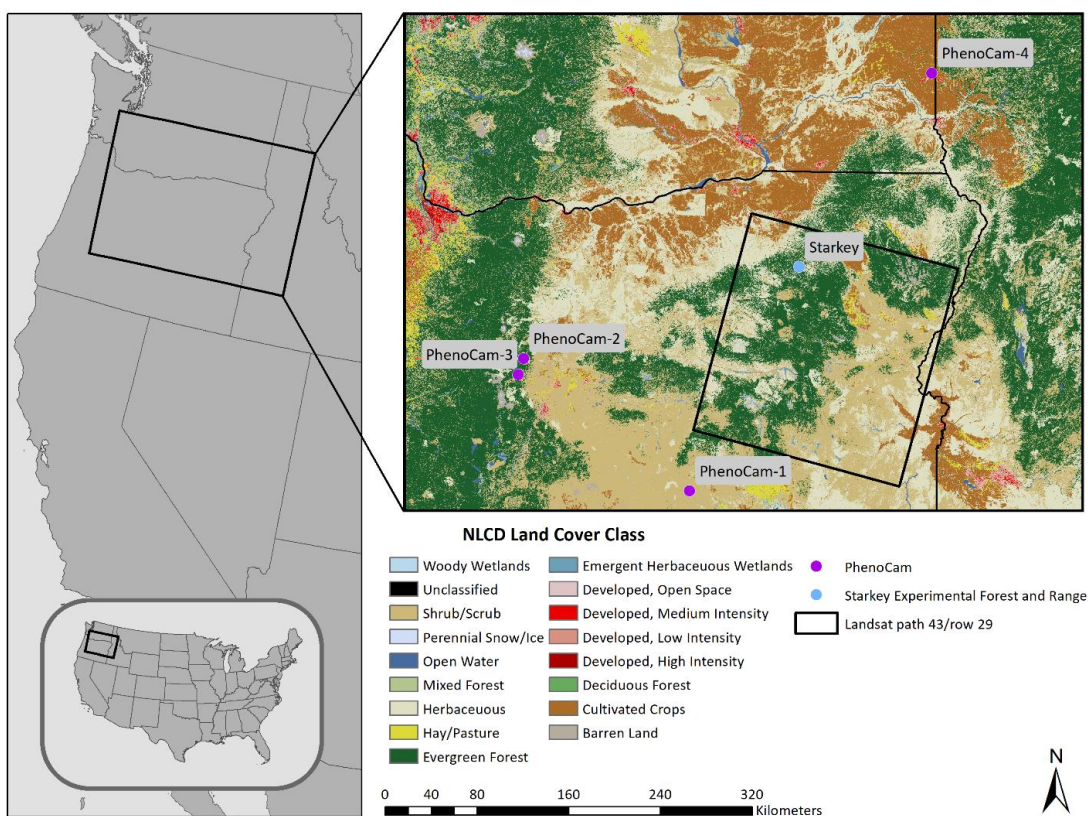


Figure 2.1. The study area including one of the Landsat scenes (Figure 2.5, 2.6) used to evaluate image fusion. Land cover types within the region vary at fine spatial scales, as shown by the National Land Cover Database (NLCD) 2016 land cover classes (Yang et al., 2018). The PhenoCam sites (purple) and the Starkey Experimental Forest and Range site (blue) used to evaluate LSP estimates are also indicated.

2.3.2 Spatio-temporal Image Fusion

2.3.2.1 Satellite Data and Image Pre-processing

The satellite data used in this study are Landsat 8 OLI (Operational Land Imager) Surface Reflectance and MODIS NBAR (Nadir BRDF-Adjusted Reflectance) imagery provided to GEE by the United States Geological Survey. Landsat data were corrected to surface reflectance with the LaSRC method (Landsat Surface Reflectance Code; Vermote et al., 2016) and included a cloud mask calculated with the CFMask method (C code based on the Function of Mask; Foga et al., 2017). MODIS NBAR data (i.e., MCD43A4) are generated using both Terra and Aqua satellites to correct MOD09 surface reflectance to a nadir viewing angle using the bidirectional reflectance distribution function generated from images in a 16-day moving window (Schaaf et al., 2002; Vermote et al., 1997). These data were found to yield the best results in spatio-temporal image fusion based on comparisons among MOD09GA, MCD43A4, and MOD09A1 (Walker et al., 2012).

In preparation of the image-fusion process, additional filtering and preprocessing methods were applied to the Landsat and MODIS data. First, Landsat and MODIS images were acquired for dates between July 29th, 2016 and June 1st, 2018. Landsat images used in the image fusion were restricted to those with less than 5-percent cloud cover to ensure that fused images were as close to cloud-free as possible. Landsat images with greater than 50-percent snow-flagged pixels were also excluded from use in the image-fusion process. All Landsat pixels flagged as cloud, cloud shadow, or snow in the quality band of each image were masked. The MCD43A4 product does not include a mask for snow, so the Snow Water Index (Dixit et al., 2019) was used to identify and mask all snow-covered pixels from the MODIS imagery. For each image, the NDVI (Normalized Difference Vegetation Index; Rouse et al., 1973) was calculated from red and near-infrared bands. The filtered and masked Landsat images were then paired with masked MODIS images from the corresponding date. For each scene, this resulted in between 6 and 11 pairs of

Landsat and MODIS images. The earliest Landsat image from 2016 was the first image paired with a MODIS image prior to September (further details provided in section 2.3.3.2). All MODIS images from dates between the first and last pairs were used for prediction. The geolocation accuracy of MODIS and Landsat differ, partially as a result of pixel resolution, and it has been reported that an additional pre-fusion step of co-registration can improve image-fusion results (Gao et al., 2015).

Therefore, MODIS images used in the GEE image fusion were registered to the earliest Landsat image of each set of pairs. The co-registration of MODIS images to Landsat images was performed using a rubber-sheet technique based on image correlation (Wang et al., 2014).

2.3.2.2 Image Fusion Algorithm and Theory

Preprocessed Landsat and MODIS imagery were used to perform an image fusion-process similar to the methods developed by Gao et al. (2006) and Zhu et al. (2010). Although systematic differences exist between these two sensors for the same location and date, Landsat OLI and MODIS surface reflectance products were recently determined to be highly comparable (Vermote et al., 2016). The implementation of image fusion in GEE was guided by the following theory and assumptions.

For a MODIS pixel with homogenous land cover (i.e., a homogenous MODIS pixel), the relationship with Landsat surface reflectance can be represented as

$$L_{s_{ij},t_k,b} = M_{s_i,t_k,b} + \varepsilon_{t_k} \quad (2.1)$$

where L and M represent Landsat and MODIS images, respectively; s_i is the location of a MODIS pixel; s_{ij} is the location of a Landsat pixel within the MODIS pixel at s_i ; t_k is the date; b is the band; and ε_{t_k} is the reflectance difference at date t_k .

Reflectance difference can be induced by various factors, including geolocation error and solar geometry at the time of acquisition. Assuming that the error is the same between time periods (i.e., $\varepsilon_{t_0} = \varepsilon_{t_1}$; Gao et al., 2006), equation (2.1) can be

rewritten to approximate the Landsat reflectance at a time where only MODIS reflectance is available as

$$L_{s_{ij},t_1,b} = L_{s_{ij},t_0,b} + (M_{s_i,t_1,b} - M_{s_i,t_0,b}) \quad (2.2)$$

where time-1 (t_1) represents a date without a true Landsat observation and time-0 (t_0) is a date with both Landsat and MODIS observations.

Land cover is often heterogenous at the scale of a MODIS pixel. The reflectance of a MODIS pixel ($M_{s_i,t_k,b}$) can be represented as a mixture of the reflectance of each cover class within that pixel. In this context, the reflectance of a MODIS pixel could be thought of as the area weighted average reflectance of each land-cover class at the Landsat scale,

$$M_{s_i,t_k,b} = \sum_{c=1}^C \left(\frac{n_c}{N} \times \frac{\sum_{j=1}^{n_c} L_{s_{ij},t_k,b,c}}{n_c} \right) + \varepsilon_{t_k} \quad (2.3)$$

where C is the total number of land cover classes; N is the total number of s_{ij} Landsat-resolution pixels within a MODIS pixel at s_i ; n_c is the number of Landsat pixels in a land-cover class; and here $L_{s_{ij},t_k,b,c}$ notates the $L_{s_{ij},t_k,b}$ (Landsat pixel reflectance) in the c^{th} land-cover class.

In practice, a pixel's surface reflectance can be better estimated by considering a moving window that includes multiple MODIS pixels at times when Landsat observations are not available. Within this window, 'similar' pixels (i.e., pixels assumed to be the same land-cover class) are used to estimate the central pixel's value. For this study, similar pixels were selected based on the following criteria defined by Gao et al. (2006)

$$\left| L_{s_{ij},t_k,b} - L_{s_i,t_k,b} \right| \leq \sigma_{t_k,b} \times \frac{2}{C_L} \quad (2.4)$$

For simplicity, $L_{s_i,t_k,b}$ is hereafter redefined to represent the central pixel in the moving window and $L_{s_{ij},t_k,b}$ to represent any other pixel within the moving

window; $\sigma_{t_k,b}$ is the standard deviation of a band (b) of the Landsat image (L) at time t_k ; and C_L is the number of land-cover classes in image L . Similar pixels were constrained to those that were similar in the image pairs immediately before and after the prediction date. Note that M has been resampled to the same resolution as L (i.e., 30 m). At this resolution for M , $M_{s_{ij},t_k,b}$ refers to a pixel within the moving window, as defined above.

To improve the prediction accuracy, similar pixels within a land-cover type were weighted based on spatial and spectral proximity (Zhu et al., 2010). It is assumed that similar pixels within a land-cover type are more likely to change similarly to the central pixel. Therefore, this weighting step ensures that pixels of the same land-cover class within close proximity are given greater weight. Different cover classes may not change at the same rate over time, so linear regression can be used to approximate a scaling coefficient (i.e., β in equation 2.5) for the rate of change of an individual cover class within the window.

After adding the moving window and scaling coefficient, equation (2.2) becomes

$$L_{s_i,t_1,b} = L_{s_i,t_0,b} + \sum_{p \in j}^P w_p \times \beta \times (M_{s_{ij_p},t_1,b} - M_{s_{ij_p},t_0,b}) \quad (2.5)$$

where P is the number of similar pixels within the window; w_p is the weight of the p^{th} similar pixel in the window; β is a scaling coefficient for the MODIS pixel difference, which is based on the rate of change between image dates for all similar pixels in the window; and s_{ij_p} notates the p^{th} similar pixel, which is located at s_{ij} . The final refinement to the prediction is achieved by averaging predictions obtained from Landsat and MODIS image pairs before and after the prediction date.

The approach outlined here follows much of the same theory and assumptions as image fusion with the ESTARFM algorithm, however, some details

differ. The design of GEE prevents the direct iteration over pixels performed in the original STARFM and ESTARFM algorithms. However, similar approaches can be applied in GEE where the neighborhood around each pixel is used. As mentioned above, the calculation for the scaling coefficient (β) in the GEE image fusion approach is based on all similar pixels within a window. In contrast, the calculation in ESTARFM solely uses values within an individual MODIS pixel. As opposed to having a scaling coefficient applied to a broad region (e.g., an entire image), calculating the scaling coefficient in the whole window keeps this calculation local to the window but still increases the region over which the scaling coefficient is applied in comparison to the calculation implemented in ESTARFM. Producing a dense time series of a vegetation index can be performed with “blend-then-index” or “index-then-blend” approaches, but it was found that the latter method produces higher accuracy results because there is less error propagation in the process (Jarihani et al., 2014). Although the algorithm used in the GEE image fusion is flexible in terms of its application to an index or reflectance, an “index-then-blend” approach was used. This raises an issue for calculating spectral similarity using the ESTARFM methodology. In assigning the weight to similar pixels Zhu et al. (2010) determined spectral similarity based on the correlation between Landsat and MODIS spectral vectors. However, spectral similarity calculated from the correlation of a single band could only take the value of -1 or 1. Therefore, spectral similarity in the GEE image fusion was calculated as the absolute difference between Landsat and MODIS pixels allowing for any number of bands to be used in the fusion process.

2.3.2.3 Evaluation

Landsat 8 images with low amounts of cloud cover that were not used in the GEE image fusion process (i.e., cloud cover between 5 and 25%) were used to evaluate the quality of the images produced through the image fusion. These images were not suited for use in the image fusion, as the amount of cloud cover was too high, but contained cloud and snow-free observations that could be compared with

the image fusion predictions. Clouds, cloud shadows, and snow were masked from these images.

Two Landsat WRS-2 scenes were used for evaluation (path 43/ row 29 and path 43/ row 30). These scenes contained all land-cover types present within the broader study area and areas of high spatial heterogeneity. All six images meeting cloud cover requirements were used to evaluate the image fusion predictions (Figure 2.1, Appendix A). The six evaluation images were captured during April, June, July, August, and September, allowing performance to be quantified across the growing season.

The overall quality of the prediction was evaluated using root mean squared prediction error (RMSPE), bias, signed relative bias (SRB), and Pearson's correlation (r), calculated as:

$$RMSPE = \sqrt{\frac{1}{n} \sum_{i=1}^n (NDVI_i - \widehat{NDVI}_i)^2} \quad (2.6)$$

$$bias = \frac{1}{n} \sum_{i=1}^n (NDVI_i - \widehat{NDVI}_i) \quad (2.7)$$

$$SRB = sign(bias) \sqrt{\frac{bias^2}{RMSPE^2 - bias^2}} \quad (2.8)$$

$$r = \frac{\sum_{i=1}^n (NDVI_i - \overline{NDVI})(\widehat{NDVI}_i - \overline{\widehat{NDVI}})}{\sqrt{\sum_{i=1}^n (NDVI_i - \overline{NDVI})^2} \sqrt{\sum_{i=1}^n (\widehat{NDVI}_i - \overline{\widehat{NDVI}})^2}} \quad (2.9)$$

where n is the number of sampled pixels, $NDVI_i$ is the NDVI value for the i^{th} pixel from the true Landsat image, \widehat{NDVI}_i is the NDVI value for the i^{th} pixel from the predicted image, \overline{NDVI} is the mean NDVI of the true image, $\overline{\widehat{NDVI}}$ is the mean NDVI of the predicted image, and $sign(bias)$ is the sign associated with the value of $bias$.

These measures were calculated from a random sample of 5,000 pixels across each image to get an overall measure of accuracy at an image level. Accuracy was also evaluated by land-cover class in each image by sampling 5,000 pixels within forest, shrub, grassland, and agriculture land-cover types. The NLCD 2016 land-cover map (Yang et al., 2018) was utilized to determine the location of each of these land-cover types. In addition to evaluating prediction metrics, the NDVI from both true Landsat and predicted images was visually inspected to identify unusual patterns in the images.

To determine cloud-computing improvements to computation time and confirm that predictive performance of the GEE implementation of image fusion was comparable to the original ESTARFM algorithm, a Python version of ESTARFM (<https://xiaolinzhu.weebly.com/open-source-code.html>) was also executed and evaluated using the same pre-processed image pairs, including the same sampling process for evaluation metrics at the scene level and within each of the land-cover classes. The ESTARFM algorithm was run on a 16-core processor (AMD Ryzen 9 3950x) at an average clock rate of 4.2 GHz.

2.3.3 Land Surface Phenology

2.3.3.1 Image Post-processing

As a post-processing step for estimating LSP, predictions of Landsat-resolution images produced using the GEE image fusion were combined with all true Landsat observations from late 2016 through the end of 2017. Landsat images that contained cloud- and snow-free observations not used in the GEE image fusion were combined with the time series of fused images. True Landsat observations were retained at times when there were both true pixels and predicted pixels. The final time series contained a near-daily record over late 2016 through the end of 2017. Detailed information about the Landsat and MODIS images used in the GEE image fusion can be found in Appendix A. All image processing, from pre-processing

through post-processing, was completed using the Python and JavaScript API's for GEE.

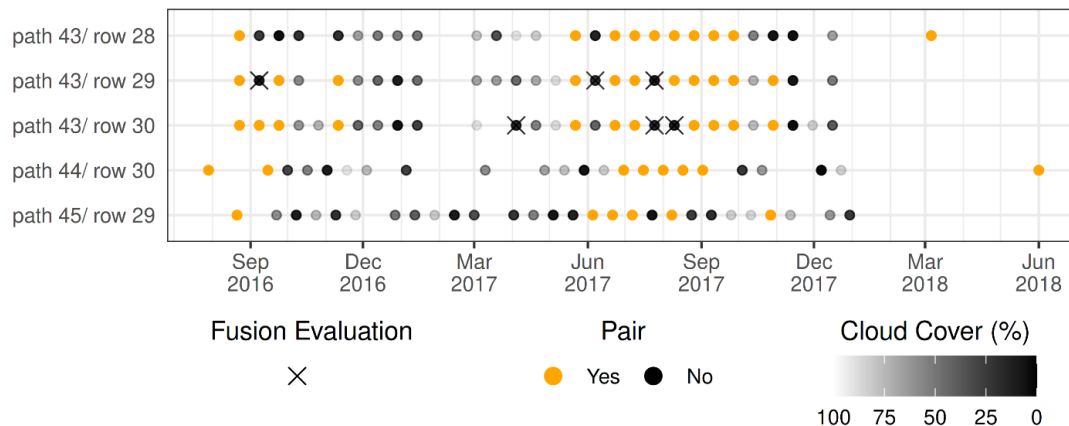


Figure 2.2. The dates of all Landsat images used in the GEE image fusion and LSP estimation for each WRS-2 scene. For LSP estimation, images occurring in January and February 2017 were dropped due to persistent cloud and snow cover during this period. An orange point indicates that the Landsat image was paired with a MODIS image for GEE image fusion. A black point indicates that the image was not used in the GEE image fusion because it had greater than 5-percent cloud cover, but valid pixels from the image were retained in the final time series. Percent cloud cover is indicated by the transparency of each point where high transparency correspond with high cloud cover. Specific images used to evaluate the accuracy of image-fusion predictions are denoted with an “X” mark.

2.3.3.2 Time Series Smoothing and Phenometric Extraction

Periods of cloud and snow cover are common in the interior Pacific Northwest, resulting in missing data in the early season (Appendix A). To approximate the NDVI at these times, the median NDVI value from September 2016 was imputed to January and February of 2017 as this time of year represents the NDVI expected for dormant vegetation in the region. This method of determining the ‘winter’ NDVI is similar to methods that have been employed to estimate long-term phenological cycles in northern latitudes, which typically do not have many snow- or cloud-free early- or late-season observations (Beck et al., 2006). Later in the growth cycle, other occasional missing values were linearly interpolated from values occurring before and after the missing observation.

Moving from a time series of observations to an estimate of phenometrics can be accomplished through several approaches (Cai et al., 2017; Zeng et al., 2020; Zhou et al., 2016). Some methods only provide an estimate of the start of season (SOS) while others offer a suite of phenology characteristics. A recent comparison of methods found that using double-logistic functions produced predictions that showed coherent spatial patterns, corresponded well with gross primary productivity, and agreed with the expected effects of elevation on phenometrics (Cai et al., 2017). Furthermore, double-logistic smoothing can capture asymmetrical annual patterns and is more robust to the effects of noise than local smoothing methods like Savitsky-Golay filtering and LOESS smoothing (Cai et al., 2017). Double-logistic smoothing also allows for the extraction of several phenometrics automatically and robustly across an image.

Double-logistic smoothing and automated phenometric-extraction techniques were applied to calculate phenometrics. The following double-logistic function was used to model the annual growth pattern:

$$v_t = m_1 + (m_2 - m_1) \times \left(\frac{1}{1 + e^{(-m_3 \times (t - m_4))}} + \frac{1}{1 + e^{(m_5 \times (t - m_6))}} - 1 \right) \quad (2.10)$$

where v_t is the vegetation index at time t ; m_1 is the minimum index value or the 'winter' NDVI; m_2 is the maximum index value; m_3 and m_5 are the rate of change associated with the SOS and end of season (EOS), respectively; and m_4 and m_6 are the day of year (DOY) associated with the SOS and EOS, respectively.

This double logistic model (equation 10) also allows for the automated extraction of phenometrics that characterize six seasonal transition dates: start of green-up, SOS, maturity, EOS, dormancy, and length of season (Figure 2.3). The SOS and EOS are represented by m_4 and m_6 , respectively, and are found at the point along the spring growth and fall senescence trajectory where the model's slope is steepest (i.e., maximum (SOS) and minimum (EOS) of the first derivative of equation 10). Start of green-up, maturity, and dormancy correspond to the model's inflection

points (i.e., local maxima of the second derivative of equation 10). Length of season is the number of days between SOS and EOS. Other characteristics that could be used to describe the phenology for an individual time series include the seasonal amplitude (i.e., $m_2 - m_1$) and the slope at the SOS and EOS (m_3 and m_5 , respectively).

Equation 10 was solved using the Levenberg-Marquardt least-squares algorithm (Levenberg, 1944). Non-linear least-squares optimization and phenometric extraction were performed with Python 3 using the LMFIT and SciPy packages (Newville et al., 2014; Virtanen et al., 2020).

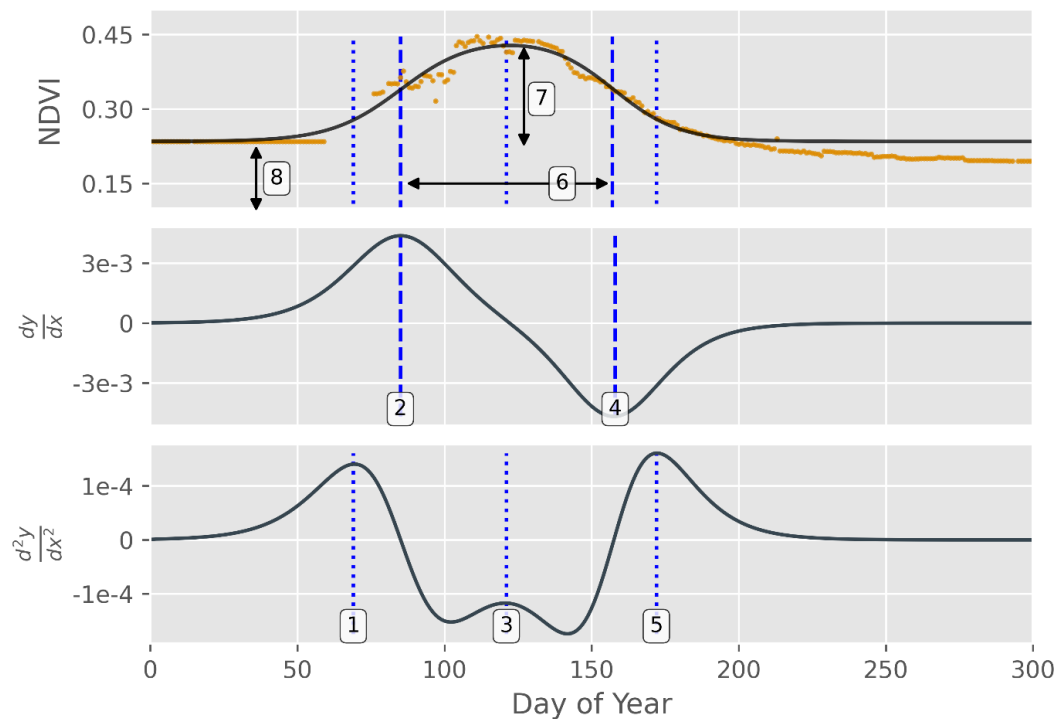


Figure 2.3. Example of the fitted double-logistic model (black line) for a single pixel's time series after post-processing (orange points). Blue dotted lines show the start of green-up (1), maturity (3), and dormancy (5). Blue dashed lines show the start of season (2) and end of season (4). Black arrows show the length of season (6), seasonal amplitude (7), and 'winter' NDVI (8). The bottom two panels show the first and second derivative of the fitted double-logistic model and the local maxima and minima corresponding to the various phenometrics.

2.3.3.3 Evaluation

Fusion-derived LSP and phenometrics were compared with estimates from near-surface cameras and ground-based observations. Near-surface estimates came from the PhenoCam Dataset v2.0 (Seyednasrollah et al., 2019) and ground-based observations came from field data provided by the Oregon Department of Fish and Wildlife (ODFW; ODFW, unpublished data). To compare the fusion-derived estimates with PhenoCam and ODFW data, the pixel nearest the location of each PhenoCam or ODFW site were extracted. Scenes overlapping PhenoCam and ODFW sites include Landsat WRS-2 path 45/ row 29, path 44/ row 30, path 43/ row 30, path 43/ row 28, and path 42/ row 28.

The PhenoCam project is a digital camera network that observes near-surface conditions across North America (<http://phenocam.unh.edu>). While several PhenoCams are located within the region, only four cameras had an adequate number of observations for 2017. The four cameras are burnssagebrush, oregonMP, oregonYP, and cafcookeastltar01, referred to hereafter as PhenoCam-1 through 4, respectively. The four cameras are located within land-cover types including sagebrush steppe (PhenoCam-1), ponderosa pine forest (PhenoCam-2, PhenoCam-3), and agriculture (PhenoCam-4). The camera located at the agriculture site did not have observations recorded before the crop was planted in 2017, so values from the dormant period after the harvest were used to estimate conditions in early 2017.

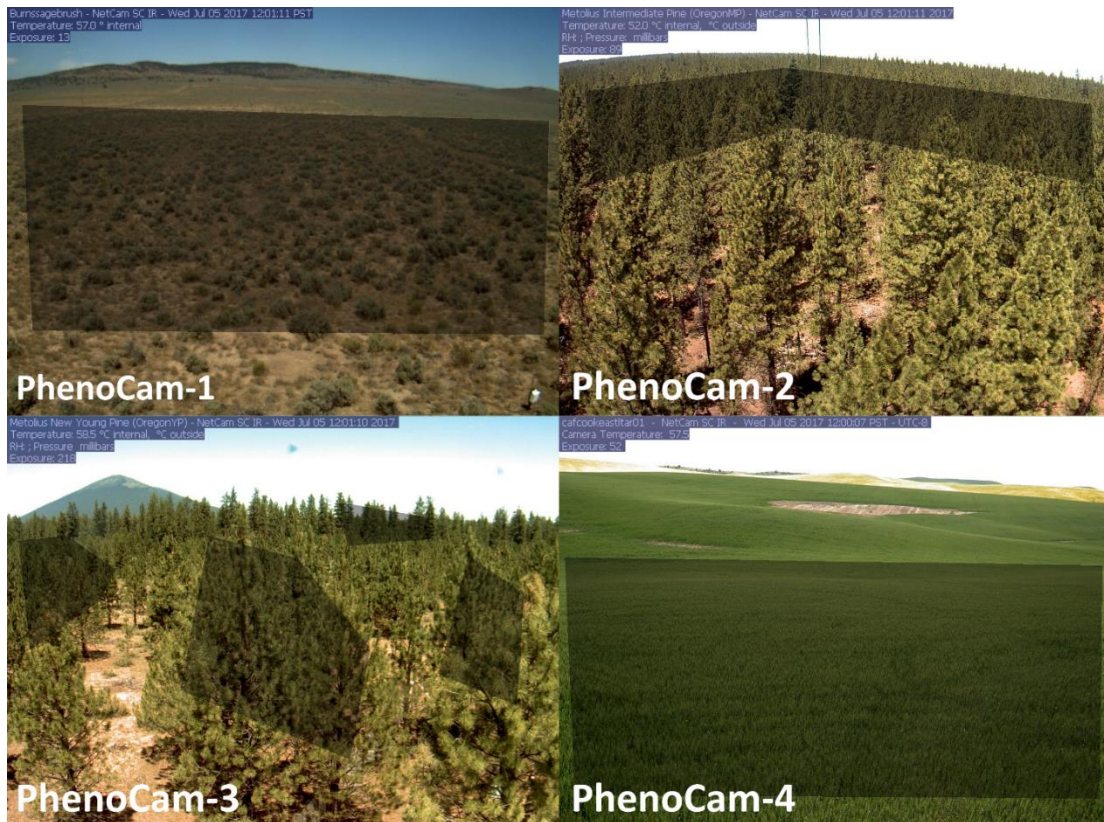


Figure 2.4. The image taken at approximately noon on July 5th, 2017 for each of the four PhenoCams. Each image recorded by the PhenoCams was masked using the shaded polygons (region of interest). The masked images were then used to calculate the mean digital number for each band.

Several preprocessing procedures were performed for the PhenoCam data (downloaded from https://daac.ornl.gov/cgi-bin/dsvviewer.pl?ds_id=1674) before their utilization in this analysis; further details can be found in Seyednasrollah et al. (2019). Green Chromatic Coordinate (G_{cc}), a canopy greenness metric, is the most similar metric to NDVI produced with the PhenoCam data and has been frequently used to compare LSP from satellites and PhenoCams (Gao et al., 2020; Richardson et al., 2018b). Green Chromatic Coordinate is defined as

$$G_{cc} = \frac{G_{DN}}{R_{DN} + G_{DN} + B_{DN}} \quad (2.11)$$

where the subscript DN indicates the digital number and R_{DN} , G_{DN} , and B_{DN} are the red, green, and blue bands, respectively. The double-logistic smoothing and

phenometric extraction techniques were applied to the prepared G_{cc} time series with the method described in section 2.3.3.2.

Field phenology data contributed by ODFW were collected at the Starkey Experimental Forest and Range (SEFR), located in the area overlapping Landsat WRS-2 scenes at path 44/ row 29 and path 43/ row 29 (Figure 2.1). A total of 11 sites in three plant-community types were monitored at two-week intervals starting April 6th, 2017 and continuing through November 11th, 2017. The plant-community types included grassland, open pine, and mixed conifer (4, 4, and 3 sites, respectively). At each site, a 25 m transect was established containing four one-meter square subplots. Within each subplot, the understory aerial cover was recorded in 20-percent intervals for four plant functional groups (forbs, grasses, deciduous woody, and evergreen woody). Additionally, the percent of plants in each of three phenophase categories (green-up, vegetative, and cured) was recorded in 20-percent intervals for each functional group. Therefore, the proportion of a given functional group in each phenophase is weighted by that functional group's total aerial cover at that time. The green-up phase included plants with any new growth (e.g., the onset of leaf greening, young leaves, increasing leaf size); the cured phase included plants with senescent leaves or other vegetative parts (e.g., loss of pigment, leaf drop, cured plant parts); and the vegetative phase included plants that fell between green-up and cured (e.g., fully green leaves, elongated stems, no longer putting on new growth).

The ODFW data of aerial cover and phenophase were summarized at the transect level to represent a scale closer to a Landsat pixel. To accomplish this for a given functional group and phenophase (e.g., forb in green-up), the subplot-level values for aerial cover class and phenophase class were first converted to the midpoint of their respective ranges (i.e., 10% represents the 0-20% class). Next, midpoint values for aerial cover and phenophase were multiplied together at the subplot level. Finally, these values were averaged across the 4 subplots within a

transect. The resulting values represent a summary of the proportion of each functional group in each phenophase relative to the cover of the functional group.

2.4 Results

2.4.1 Spatio-temporal Image Fusion

Combining all available cloud- and snow-free Landsat images with the GEE image fusion predictions resulted in a substantial increase in the number of 30 m observations. Within the two scenes for which GEE image fusion was evaluated, the final time series had a median of 215 observations in each pixel between DOY 1 and 300, with the middle 90% of pixels containing between 53 (5th quantile) and 248 observations (95th quantile) for this period. This temporal range (i.e., DOY 1 – 300) captures the region's growing season, with a buffer on either side. Pixels associated with the lower range of these values corresponded to high elevation areas with persistent snow and cloud cover.

Visual comparison of the GEE image fusion predictions with true Landsat images from the same date showed relatively strong correspondence (Figure 2.5). Areas where differences were most apparent corresponded to conditions of especially high-spatial or high-temporal variability, such as areas with forest and grassland in close-proximity and areas where surface water was ephemerally present. This was not unexpected as an accurate prediction of abrupt or rapid changes is a known challenge for image fusion techniques (Gao et al., 2006; Zhu et al., 2010).

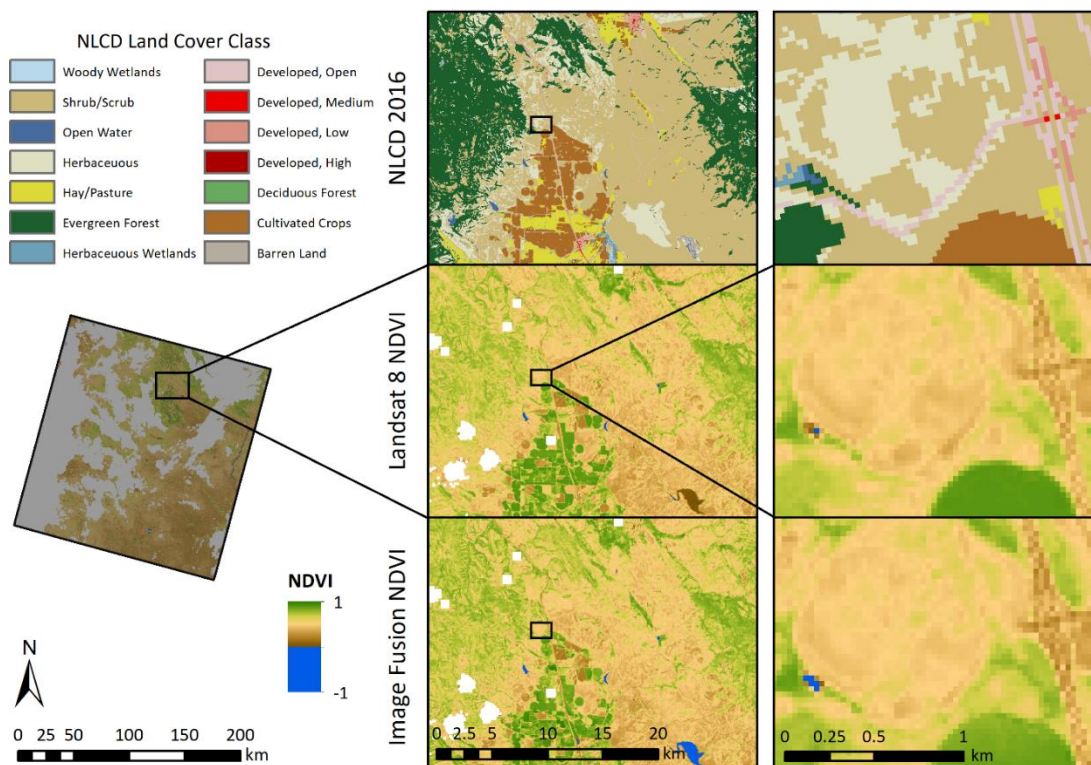


Figure 2.5. Three panels showing the 2016 NCLD land-cover classes, NDVI from the true Landsat image, and NDVI from the GEE image fusion prediction. This example is from path 43/ row 29 on June 7th, 2017. Image pairs used for this prediction occurred on May 22nd, 2017 and June 23rd, 2017. The location of this scene is shown in the context of the study region in Figure 2.1. NDVI values below 0 shown in blue to help focus on the variation in the 0 to 1 range. Masked pixels are shown in white.

Overall, the images predicted with the GEE image fusion strongly corresponded with the true Landsat observations from the same date (Table 2.1, Figure 2.6, Appendix B). Predicted images had the lowest correlation to true Landsat images in the early growing season (e.g., the image from DOY 94 at path 43/ row 30). The evaluation metrics calculated on a scene-wide basis also showed that the GEE image fusion performed better during peak growing season than during earlier or later periods of the year. The predictions had negative bias and SRB, overpredicting NDVI in five out of the six images. Overall, SRB ranged from 0.07 to -0.54 and was best during the peak of the season. As expected, variability in the predictions was similar but slightly lower than variability in the true Landsat images

(an artifact of downscaling coarse-resolution data). Differences in variability in the evaluation images follows seasonal trends also present in RMSPE, bias, and SRB.

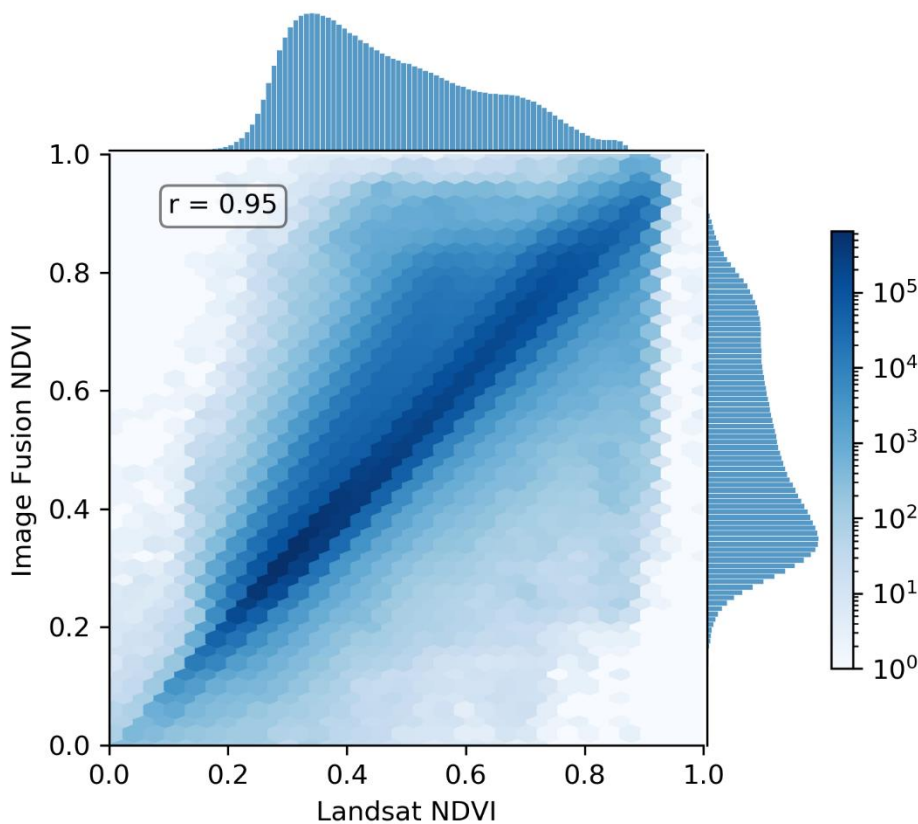


Figure 2.6. Hex grid of the NDVI derived from true Landsat vs. the GEE image fusion for path 43/ row 29 on June 7th, 2017 (DOY 158, Figure 2.5).

Compared to the locally run ESTARFM algorithm, the total processing time between the two methods differed substantially. On average, the GEE fusion completed in 105.83 minutes, and the ESTARFM processing completed in 298.41 minutes. However, evaluation metrics demonstrated similar performance between the GEE fusion and locally run ESTARFM methods (Table 2.1).

Table 2.1. Image evaluation results for each DOY and scene combination. A total of 5,000 pixels were sampled from each image to calculate bias, correlation, RMSPE, and SRB. All pixels were used to calculate the variance of each image. *Italicized*

values inside parentheses correspond to the ESTARFM results while the GEE image fusion results are in a regular typeface.

path 43/ row 29

<i>DOY</i>	<i>Landsat σ^2</i>	<i>Image Fusion σ^2</i>	<i>Bias</i>	<i>Pearson's r</i>	<i>RMSPE</i>	<i>SRB</i>
158	0.033	0.028 (0.032)	-0.026 (-0.027)	0.955 (0.955)	0.060 (0.060)	-0.483 (-0.51)
206	0.040	0.042 (0.042)	-0.002 (-0.002)	0.980 (0.978)	0.041 (0.043)	-0.059 (-0.042)
252	0.047	0.040 (0.049)	-0.016 (-0.015)	0.971 (0.972)	0.054 (0.053)	-0.318 (-0.291)

path 43/ row 30

<i>DOY</i>	<i>Landsat σ^2</i>	<i>Image Fusion σ^2</i>	<i>Bias</i>	<i>Pearson's r</i>	<i>RMSPE</i>	<i>SRB</i>
94	0.011	0.008 (0.012)	-0.032 (-0.031)	0.847 (0.870)	0.066 (0.064)	-0.546 (-0.562)
206	0.022	0.022 (0.019)	0.002 (0.002)	0.977 (0.981)	0.032 (0.030)	0.070 (0.063)
222	0.018	0.017 (0.018)	-0.002 (-0.001)	0.971 (0.98)	0.033 (0.027)	-0.049 (-0.039)

When predicted images were evaluated by the four land-cover classes, a seasonal trend was also present in the RMSPE, bias, and SRB (Figure 2.7). Predictive accuracy varied by land-cover type, with shrubland and grassland generally performing better across the year in terms of RMSPE and bias. However, when the class variability is considered (i.e., SRB), the difference in performance between land cover classes was less noticeable. While forest and agriculture classes tended to have higher variation in bias across the year, the SRB is more similar across classes because the variability of NDVI is lower in grassland and shrubland. This is not unexpected as forest and agricultural areas are more spatially heterogenous than grassland and shrubland areas in this region. GEE fused images tended to overpredict rather than underpredict, regardless of the cover type. As found in the scene-wide evaluation, ESTARFM produced similar results across the four different land-cover types (Figure 2.7).

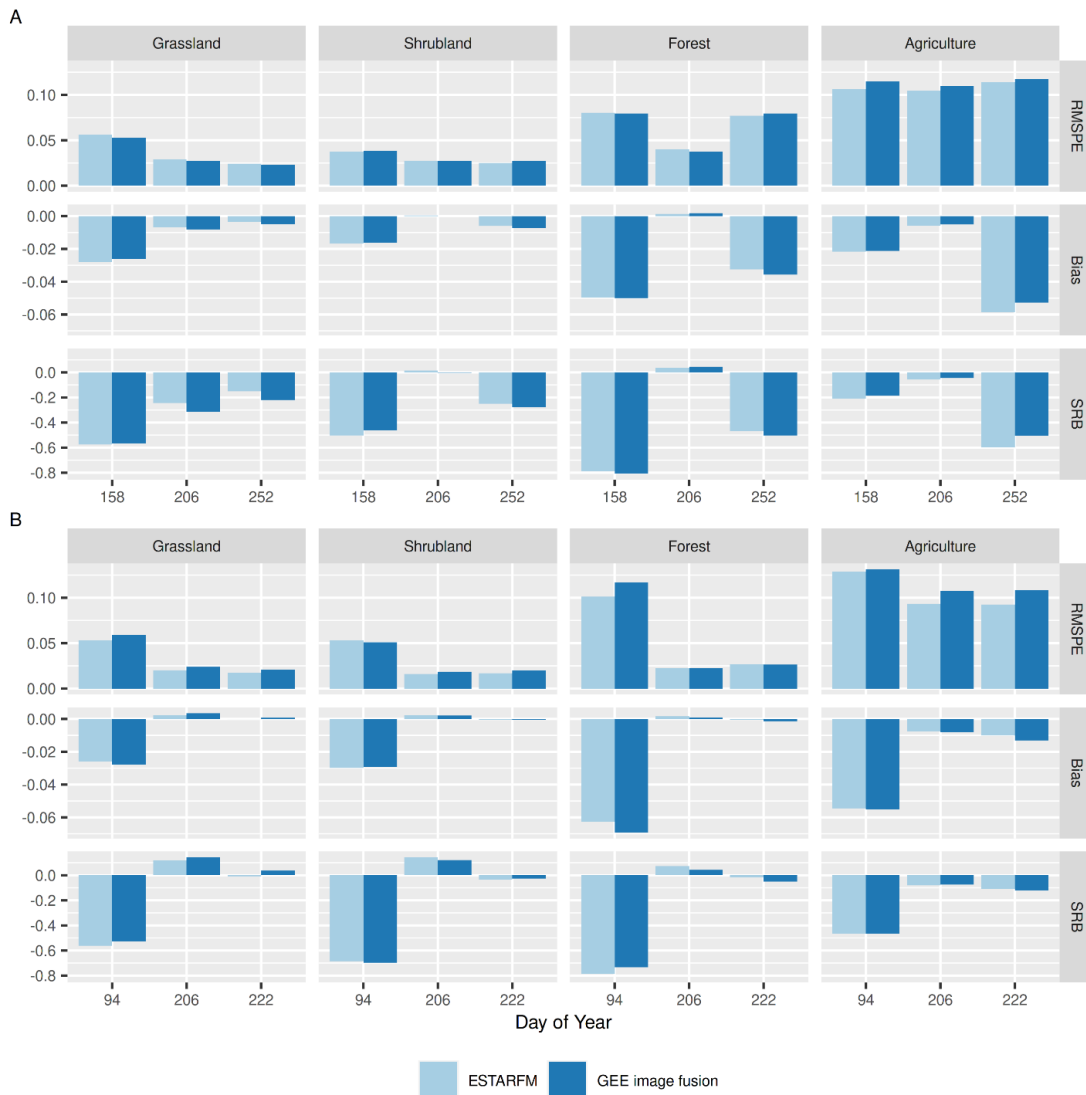


Figure 2.7. Performance of the GEE image fusion and locally run ESTARFM within the four NLCD land-cover types and within the scenes located at A) path 43/ row 29, and B) path 43/ row 30. The x-axis shows the DOY in which the model performance was evaluated for each scene (3 DOY's/scene). Performance metrics evaluated for each scene-date combination include RMSPE, bias, and SRB.

2.4.2 Land Surface Phenology

2.4.2.1 PhenoCam

General temporal trends in the double-logistic curve fit were consistent between the GEE image fusion and PhenoCam datasets (e.g., Figure 2.8). However, not all NDVI-derived phenometrics estimated from the GEE image fusion dataset

reliably aligned with the G_{cc} -derived phenometrics estimated from the PhenoCam datasets. Both datasets resulted in similar SOS but different EOS for the PhenoCam located in sagebrush steppe near Burns, Oregon (PhenoCam-1; Figure 2.8).

The PhenoCam in agricultural lands near Moscow, Idaho (PhenoCam-4) showed little similarity in the predicted SOS and EOS metrics (Appendix C). However, the image fusion dataset did show a similar trend in declining NDVI at the EOS. Some of the differences in predicted metrics at this site are likely attributable to greening in the early season not recorded by this PhenoCam (this site had early-season values imputed). As other authors have noted, conifer forests typically do not have distinct transitions between the dormant and active states. The double-logistic model is not suited to reliably capture such seasonal trends (Nijland et al., 2016). Accordingly, the phenometrics from the two PhenoCam sites located in conifer forest near Bend, Oregon (PhenoCam-2, PhenoCam-3) did not align well with the NDVI-derived phenometrics (Appendix C).

Table 2.2. Phenometrics (DOY) estimated at each of the PhenoCam sites.

Dataset	Site	SOG	SOS	Mat	EOS	Dorm
NDVI- image fusion	PhenoCam-1	63	71	110	172	194
	PhenoCam-2	--	62	--	142	--
	PhenoCam-3	--	-823	--	292	--
	PhenoCam-4	56	74	92	223	279
G_{cc} - PhenoCam	PhenoCam-1	50	84	117	252	331
	PhenoCam-2	50	104	165	306	362
	PhenoCam-3	28	91	190	314	362
	PhenoCam-4	138	149	169	193	201

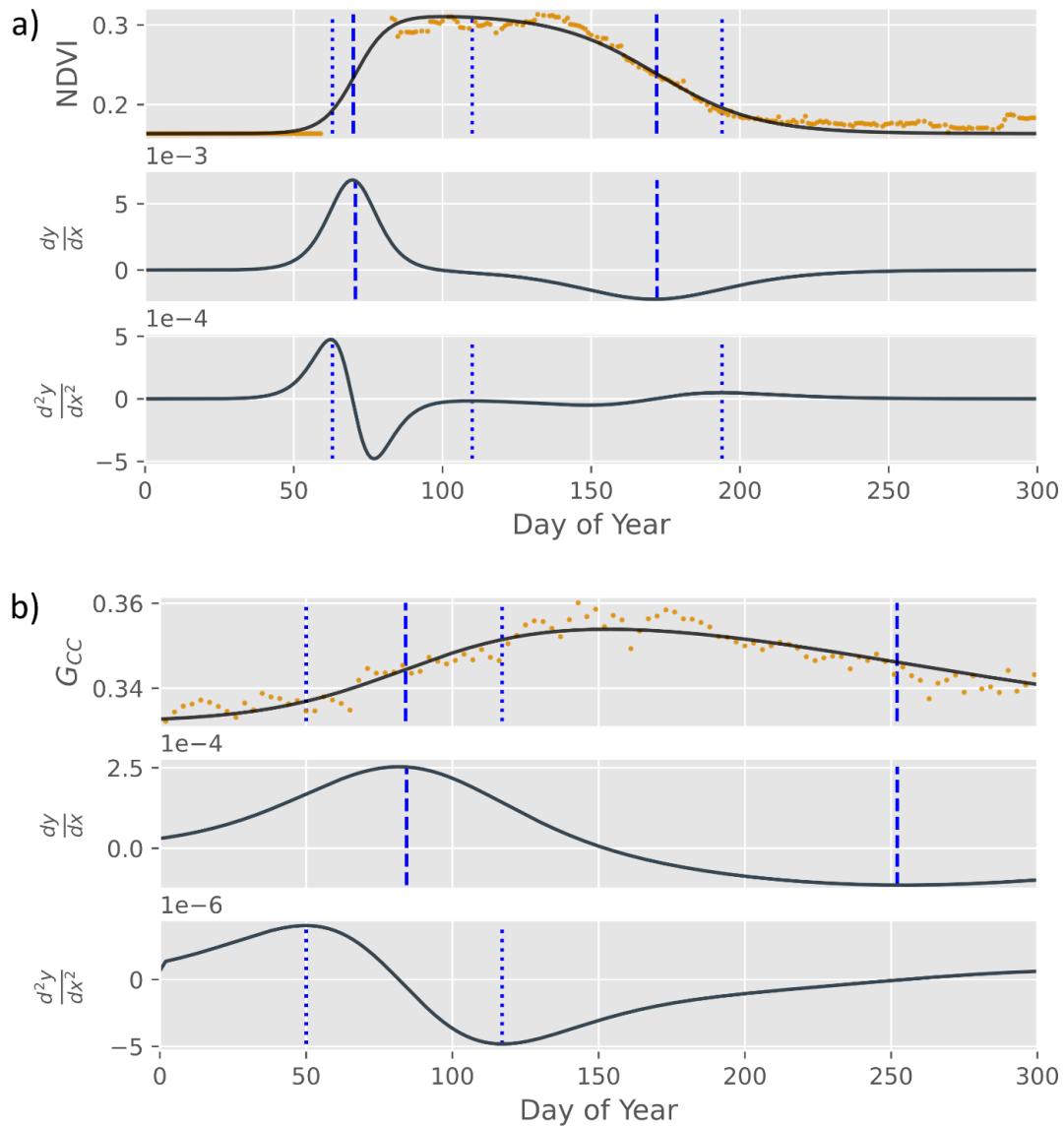


Figure 2.8. Comparison of the time series and model fit for the sagebrush PhenoCam site near Burns, Oregon (PhenoCam-1). The top panel (a) shows the GEE image fusion’s NDVI-derived time series, model, and phenometrics. The bottom panel (b) shows the PhenoCam’s G_{cc} -derived time series, model, and phenometrics. For each main panel (i.e., a and b), the three subpanels follow the labeling and symbology conventions of Figure 2.3.

2.4.2.2 Starkey Experimental Forest and Range

The fusion-derived SOS corresponded with SEFR understory observations at a few of the open pine sites (Figure 2.9, transects 4, 6, and 9). At these sites, the estimated SOS occurred when the dominant functional groups (grass, forb) were

primarily in the green-up phenophase. Because phenology monitoring at SEFR did not start until April 6th, 2017, the true beginning of the season and growth initiation was not captured for the SEFR grassland sites (Figure 2.10). The fusion-derived EOS and dormancy closely aligned with field-observed patterns of senescence and temporal trends in dominant functional groups. EOS most frequently occurred when the proportion of plants putting on new growth rapidly decreased and right before or during the time when the proportion of cured plants increased. Dormancy coincided with the time of year when the proportion of cured plants was at or near its maximum. As expected, correspondence between the fusion-derived phenometrics and the SEFR understory field observations was lowest for the SEFR mixed-conifer sites (Appendix D). Correspondence is likely to decrease with increased mature conifer canopy cover as conifer dominance will obscure the signal exhibited by understory plants.

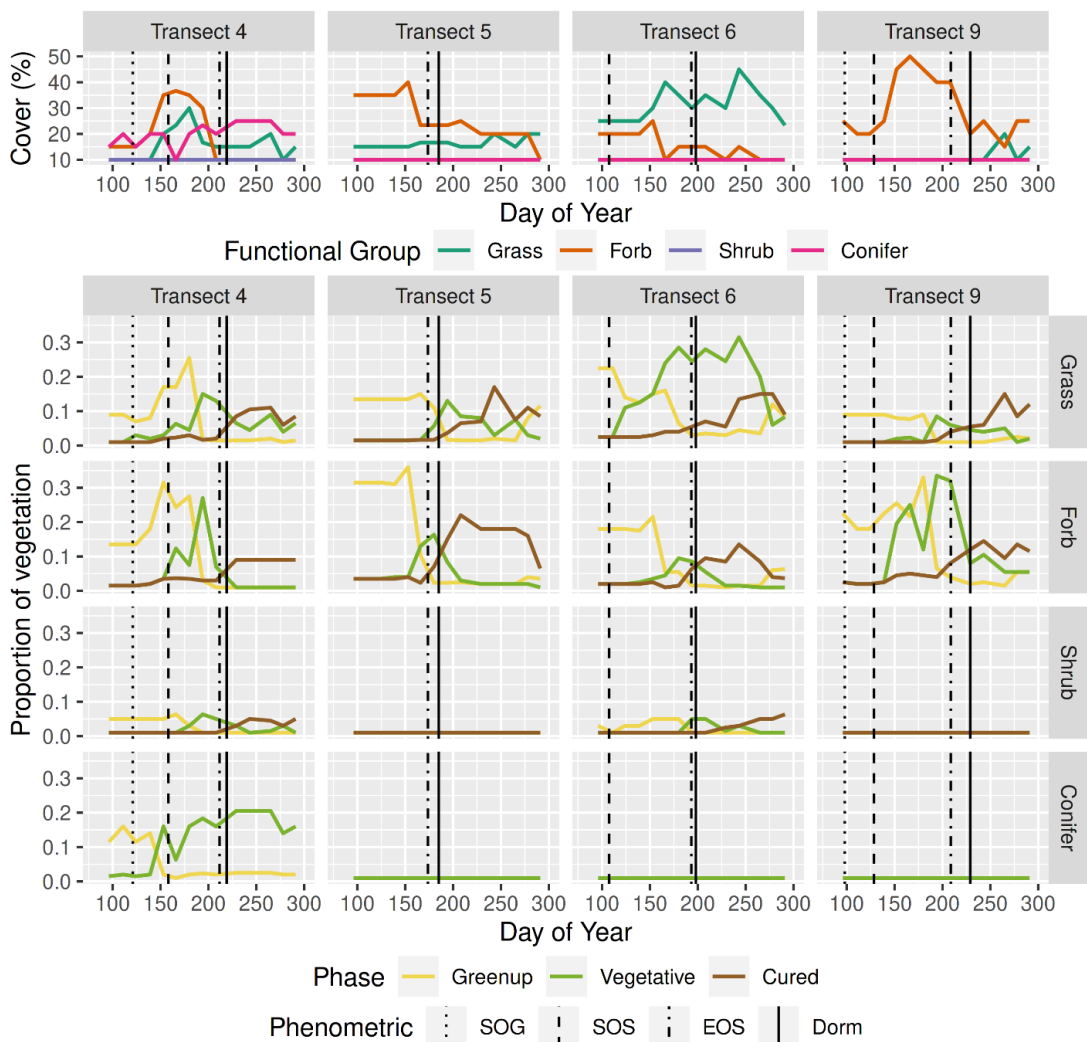


Figure 2.9. The SEFR transects sampled in open-pine sites for the 2017 growing season. The top panel shows percent cover by functional group at the four sites (transects). The bottom panel shows the proportion of vegetation in each phase by functional group. In both panels, vertical lines show the phenometrics estimated from the GEE image fusion's NDVI time-series, including start of green-up (SOG), start of season (SOS), end of season (EOS), and dormancy (Dorm). In both panels, lines may overlap for functional groups with little aerial cover (i.e., those with cover recorded in the 0-10 % class or low proportion in a given phase; e.g., shrub in transect 5 or, at day of year 100 in transect 5, grass in the cured phase).

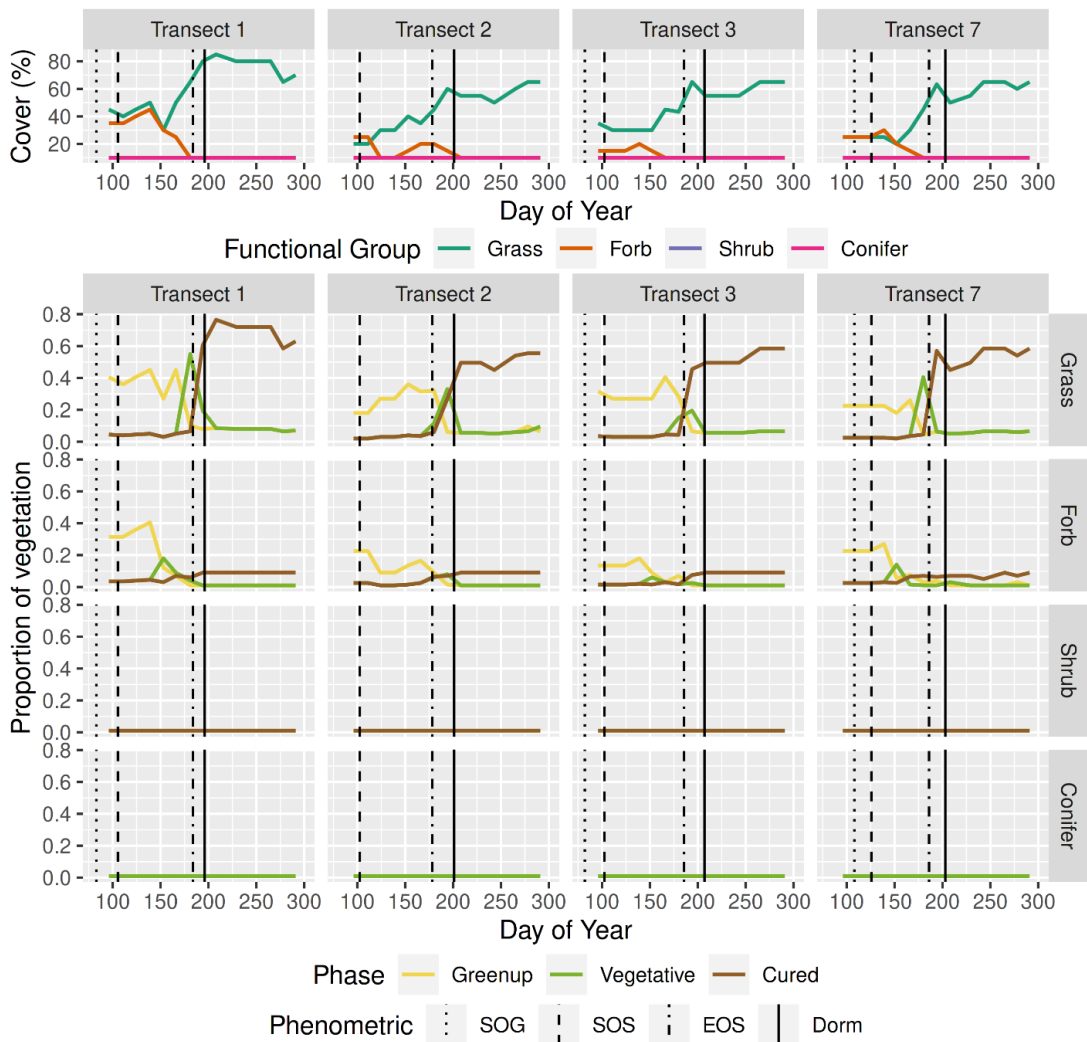


Figure 2.10. The SEFR transects sampled in grassland sites for the 2017 growing season. The top panel shows percent cover by functional group at the four sites (transects). The bottom panel shows the proportion of vegetation in each phase by functional group. In both panels, vertical lines show the phenometrics estimated from the GEE image fusion's NDVI time-series, including start of green-up (SOG), start of season (SOS), end of season (EOS), and dormancy (Dorm). In both panels, lines may overlap for functional groups with little aerial cover (i.e., those with cover recorded in the 0-10 % class or low proportion in a given phase; e.g., shrub in transect 5 or, at day of year 100 in transect 5, grass in the cured phase).

2.5 Discussion

This study explored the utility of GEE in implementing an ESTARFM-like image fusion technique that was applied to estimate LSP at a 30 m resolution. When estimates of LSP are derived exclusively from MODIS or Landsat, they are limited by

the spatial or temporal characteristics of these data. As a result, intraannual LSP from MODIS is limited to 250 to 500 m resolutions (Zhang et al., 2018, 2003), while higher spatial-resolution estimates from Landsat are often limited to multiyear averages (Melaas et al., 2016, 2013). Both approaches characterize different aspects of phenology but may be constrained in their application to processes that fit within their respective spatial or temporal domains. Recently launched satellites like Sentinel-2 and the creation of the Harmonized Landsat Sentinel dataset (Claverie et al., 2018) have created new opportunities for estimating LSP with high-spatial and high-temporal resolution (Bolton et al., 2020; Gao et al., 2020; Zhang et al., 2020). However, these data lack the long archive available with sensors like Landsat or MODIS, which allow for LSP estimates from the past two decades or more.

2.5.1 Spatio-temporal Image Fusion

This study demonstrated that spatio-temporal image fusion implemented on a cloud-computing platform can produce accurate image predictions throughout the growing season. Implementing image fusion in cloud-computing environments can increase the accessibility of image fusion datasets for enhanced prediction of intraannual phenology. The evaluation showed that our implementation of image fusion on GEE had similar accuracy to ESTARFM for a heterogenous landscape, both when considered as a whole and within particular vegetation classes. The accuracy reported in this study was also within the range of accuracy reported by other studies evaluating image-fusion algorithms (Chen et al., 2015; Liao et al., 2016). Early season predictions from GEE image fusion were the least correlated with true Landsat images, which is likely attributed to the rate of vegetation change in early season or the length of time between image pairs and predicted images (Figure 2.2, Appendix A). The linear-change assumption of the model is less reliable when the time between predictions is greater. Implementation on GEE also substantially decreases the processing time required for large-scale image-fusion tasks, processing evaluation images 2.8 times faster than the locally run ESTARFM

algorithm. In testing the GEE image fusion algorithm, a year and a half of image predictions completed in approximately the same time as reported for a year of image predictions produced with the STARFM algorithm (Gao et al., 2017); this is a significant reduction, considering that other comparisons show that ESTARFM processing takes longer than STARFM (Rao et al., 2015).

Unlike the ESTARFM algorithm, the GEE image fusion method uses all MODIS pixels with the moving window to determine the conversion coefficient. Predictive performance in heterogenous landscapes for ESTARFM draws from this conversion coefficient and its relation to principles of spectral unmixing (Zhu et al., 2010). Specifically, the conversion coefficient accounts for the land-cover rate of change by estimating change within a land-cover class relative to the change in an individual MODIS pixel. Instead of considering change relative to an individual MODIS pixel, our implementation determines this coefficient for the entire window. This allows the relative rate of change to remain local to the window while providing a more generalized approximation based on the relationship between all MODIS and Landsat pixels in a cover class.

2.5.2 Land Surface Phenology

The comparison between image-fusion and PhenoCam phenometrics showed mixed results. While general trends in phenology held for shrublands, phenometrics such as SOS and EOS were not similar between the datasets. In a worldwide study, Richardson et. al. (2018b) found that NDVI-derived estimates of the SOS from MODIS in agriculture and grassland differed by 25 and 11 days with standard deviations of 27 and 15 days, respectively. Differences in the spectra used for NDVI (image fusion) and G_{CC} (PhenoCam), sun-sensor angles, cloud- or snow-cover effects, and field-of-view could contribute to phenometric differences between the datasets.

This study's use of the MCD43A4 product could have also impacted the similarity of image-fusion-derived phenometrics and PhenoCam phenometrics or

field data. MODIS NBAR data are corrected to account for the pixel level anisotropy using a BRDF model calculated from a 16-day window (Schaaf et al., 2002). Accordingly, any surface changes (e.g., vegetation growth/senescence, disturbance) that may have occurred over this time frame could impact the BRDF model and the adjusted reflectance. Depending on the surface conditions over the 16-day window, the BRDF adjusted reflectance could result in earlier or later NBAR-based phenometrics compared to either PhenoCams or field observations. However, the benefits of correcting view angle effects outweighed the potential phenology related drawbacks.

A unique characteristic of the SEFR field data was that vegetation was assessed for functional groups instead of individual species. Temporal trends in functional groups coincided with LSP estimated from GEE image fusion at the grassland site and most of the open-pine sites. Additionally, EOS estimates derived from the GEE image fusion dataset closely corresponded with the dates when the dominant functional groups transitioned to a senescent state. Some LSP studies have found good SOS correspondence with field data but poorer correspondence with EOS estimates (Friedl et al., 2010; Ganguly et al., 2010). Field-based estimates of SOS and EOS typically do not account for herbaceous understory vegetation when making comparisons to satellite-based estimates (Nijland et al., 2016). In the SEFR open pine and grassland sites it appeared that this herbaceous component was indicative of the EOS and dormancy metrics estimated from the satellite data (Figure 2.9, Figure 2.10). However, this herbaceous understory signal was obscured when overtopped by high tree canopy cover (e.g., mixed-conifer sites; Appendix D).

Our validation with ground-based observations and near-surface camera data highlights some of the challenges and opportunities with applying these datasets for LSP studies. Comparisons between satellite LSP and PhenoCam estimates may also benefit from using sensors in PhenoCams that capture wavelengths more similar to those used in multispectral satellites. For example,

sensors with a near-infrared band are more capable of observing vegetation structural changes (Filippa et al., 2018, Luo et al., 2018, Petach et al., 2014), and these types of sensors have been demonstrated to provide reasonable correspondence with LSP from multispectral satellite observations (Eklundh et al., 2011).

The comparability of field-based observations to LSP has historically been limited due to mismatches in scale and observation method (Hufkens et al., 2012); for example, budburst of a species vs. aggregate vegetation within a pixel. Mismatches in scale and observation method may be partially resolved by downscaling LSP to resolutions more attainable by field studies. Correspondence between satellite LSP and functional group phenology warrant further investigation to assess if field data collection of functional groups is preferable to species-level assessments.

2.5.3 Future Directions and Potential Applications

Implementation of an ESTARFM-like image fusion algorithm in GEE was not without its challenges. Moving windows are not ideal for a platform designed to divide datasets into smaller units for parallel computation. Recently, Moreno-Martínez et al. (2020) implemented a bias-aware Kalman filter method in GEE for the fusion of Landsat and MODIS, which produces a monthly gap-filled 30 m product across the United States. The integration of deep learning libraries like TensorFlow (Abadi et al., 2015) with GEE also offers new possibilities for further innovation in image fusion methods, potentially building upon current deep learning methods for image fusion (Song et al., 2018), while taking advantage of the cloud computing infrastructure of GEE.

The phenometrics extracted from the GEE-image-fusion time series represented some grassland, shrubland, and open-pine patterns in this study. However, not all landcover types were adequately captured, such as dense conifer

forest and agriculture. Sensitivity of NDVI to fluctuations in vegetation biomass or the double logistic function's ability to adequately model the development patterns of vegetation may account for challenges in these landcover types. As opposed to using a single index like NDVI, a multivariate perspective of phenology could be considered, which would allow for temporal patterns of different spectral bands or indices to be captured simultaneously (Pasquarella et al., 2016). Many other methods for phenometric extraction exist (Zeng et al., 2020) and could be used for vegetation with temporal patterns that are difficult to characterize with a double-logistic function. For example, in agricultural areas, it may be necessary to employ a method capable of characterizing multiple crop cycles within a single year.

Capturing intraannual LSP may also help ecologists studying rapidly changing ecosystems, like those where species invasions lead to shifts in plant community composition (D'Antonio and Vitousek, 1992; Gunderson, 2000; Kerns et al., 2020). Phenometrics from GEE image fusion could be used to identify the distribution of exotic annual grasses. The distinct phenological traits (Wallace et al., 2015) and rapid colonization from *Ventenata dubia* in the interior Pacific Northwest (Kerns et al., 2020) may present this methodology's ideal application. Phenological patterns have been employed to identify and map populations of other invasive annual grasses in the western United States, however data used in these studies was limited in spatial resolution (Boyte and Wylie, 2016; Bradley et al., 2017). Limited spatial resolution presents a challenge in identifying small grass populations across spatially heterogeneous landscapes. Additionally, annual grass species strongly respond to year-to-year climatic variation (Pilliod et al., 2017) and represent a substantial proportion of surface canopy cover in some shrubland, grassland, and open pine communities (D'Antonio and Vitousek 1992). Thus, in temporally dynamic situations, intraannual LSP estimates may be useful. The availability of high-spatial and high-temporal resolution estimates of LSP over the last two decades may also provide an opportunity to track the unique characteristics of this rapid plant invasion over time.

2.6 Conclusions

This study addressed two challenges in estimating vegetation phenology at ecologically meaningful spatial and temporal scales. Employing spatio-temporal image fusion on a cloud-computing platform like GEE is feasible and can produce high-quality predictions in reasonable timeframes. We found that GEE image fusion predictions were accurate and similar to those produced by a locally run version of ESTARFM. Furthermore, using a time series enhanced with the additional data from the image-fusion process can lead to LSP estimates that coincide with plant development patterns in shrubland, grassland, and open-pine land-cover types. We showed that satellite-LSP estimates aligned with the phenology of dominant functional groups at some field sites. However, we found that NDVI-derived phenometrics from satellite data and G_{CC} -derived phenometrics from PhenoCam data did not closely align, which could be attributed to spectral, sun-sensor angle, and cloud-cover differences between the two datasets.

Characterizing LSP in semi-arid regions like the interior Pacific Northwest continues to be challenging, especially within conifer-dominated areas and when cloud cover prevents surface observation in the early growing season. Incorporating data from satellites like Sentinel-2 and continued efforts to improve image fusion on cloud-computing platforms can help overcome some current data limitations. Capturing intraannual vegetation development patterns can continue to provide insight into meaningful and useful processes as they play out across landscapes now and in the future.

2.7 Acknowledgements

This research was supported in part by the by the Joint Fire Science Program (Proposal ID: 16-1-01-21). For assistance with SEFR project management, fieldwork, and data collection, we thank P. K. Coe, B. K. Johnson, and D. A. Clark, and C. L. Brown. The code development for this project was made possible through open-source software and contributions from the Google Earth Engine community. We are

greatly appreciative of the anonymous reviewers that provided detailed and helpful feedback that improved this manuscript.

3 MAPPING THE INVASIVE ANNUAL GRASS *VENTENATA DUBIA* IN THE NORTHWESTERN UNITED STATES

3.1 Abstract

Since first being observed in the northwestern United States in the 1950s, *Ventenata dubia* (*ventenata*) has spread throughout much of the west, becoming particularly problematic in the Blue Mountains Ecoregion (BME). The rapid spread of this winter annual grass and its abundance in previously invasion-resistant areas warrants the development of information detailing this species' range and distribution. To complicate matters, *ventenata* is invading a region with a history of annual grass invasion by species such as cheatgrass (*Bromus tectorum*) and medusahead (*Taeniatherum caput-medusae*). We developed three models using climatic, topo-edaphic, and image fusion derived (30m) estimates of land surface phenology (LSP) to 1) provide the best possible estimate of *ventenata*'s distribution for management and policy decisions, and 2) examine the separability of this species from other known annual invaders based on the niche and remotely-sensed predictors. These models differed in their inclusion of predictor sets and are referred to as the 1) hybrid (LSP, climate, topo-edaphic), 2) bioclimatic (climate, topo-edaphic), and 3) phenology (LSP). The best performing hybrid model had a mean cross-validated AUC of 0.89. *Ventenata* (>20% cover) was commonly predicted in ecotones between forested and non-forested areas of the region and in shrub-grass openings of the forest matrix. Comparison of the hybrid and bioclimatic models showed that parts of the region with high environmental suitability have not yet been invaded. Comparison of the hybrid and phenology models showed that parts of the region with high probability from the phenology model align with previous predictions of cheatgrass presence and present populations of *ventenata*. We contend that, in some cases, incorporating LSP with climatic predictors can assist with model differentiation of invasive annual grasses where phenological patterns may be similar, but environmental niche requirements differ. Our models indicate that 7.7% (5,454 km²) of the BME may have contained robust populations of

ventenata in 2017. Our map estimates provide the first regional spatially explicit information about the ventenata invasion in the ecoregion. Given the distribution of this species, it will be important to consider the potential impacts of ventenata when making regional management and policy decisions.

3.2 Introduction

Numerous non-native annual grass species have been introduced to the North American west. Some of these introductions have led to extensive changes in ecosystem structure and function (Keeley et al., 2005; Levine et al., 2003; Simberloff et al., 2013). Of particular concern is these species' ability to alter regional fire regimes (Brooks et al., 2004; D'Antonio and Vitousek, 1992; Mack and D'Antonio, 1998). Winter annual grasses like cheatgrass (*Bromus tectorum*), medusahead (*Taeniatherum caput-medusae*), and buffelgrass (*Cenchrus ciliaris* L.) have long been recognized for their ecological effects (Knapp, 1996; Mack, 1981; Miller et al., 2010; Young, 1992; Young and Evans, 1970), but have recently been joined by other exotic annual grass species. Addressing the present and future implications of these species' invasions requires an understanding of their spatial and temporal distribution (Forsyth et al., 2012). When collected at a local and regional level, this information can help estimate spread rate, locate problematic populations, and determine site characteristics that influence spread or persistence (Funk et al., 2020). This study aims to understand the contemporary spatial distribution of a newly problematic annual grass species (*Ventenata dubia*) found in the northwestern US by developing and evaluating presence models based on remote sensing, climatic, and topo-edaphic predictors.

Ventenata dubia (wiregrass; henceforth ventenata) is a winter annual grass species from Mediterranean Eurasia and northern Africa (Wallace et al., 2015) and was first observed in eastern Washington state in the 1950's. The rapid expansion of this species over a short timespan has meant that the ecological and economic impacts are yet to be realized. Ventenata has been observed invading grasslands and shrublands (Averett et al., 2020; Endress et al., 2020; Jones et al., 2018) and has become abundant in non-forested openings within forested mosaics (Tortorelli et al., 2020). Cheatgrass has also been problematic in shrublands but less so at higher elevations because lower soil temperatures are known to restrict its growth and

reproduction (Chambers et al., 2014b, 2007). The presence of robust *ventenata* populations in forest openings appears to be unique compared to other annual grass species and is likely related to *ventenata*'s occupancy of distinctly different niche space (Tortorelli et al., 2020). Non-forest openings in this region provide unique habitats and have also served as fuel breaks in wildfire control efforts. The accumulation of fine fuel biomass in these openings may lead to fire behavior alterations in areas that have not already suffered impacts from cheatgrass invasion.

Concern over *ventenata*'s landscape-scale impacts and its potential to alter fire behavior necessitates the acquisition of cartographic information identifying invasion risk and the current invasion status and extent (Kerns et al., 2020). The development of management strategies and policies for invasive species is commonly hampered by a lack of necessary information about the range and abundance of newly introduced species (Funk et al., 2020). This information is critical for planning and allocating limited resources available to managers. As such, this data's precision and accuracy can substantially impact the long-term outcomes from management decisions (Cheney et al., 2018). Additionally, evaluating policy decisions and management actions also requires information quantifying the current status and trends of species invasion (Jetz et al., 2019). For developing this necessary information, traditional field sampling has been combined with remote sensing and climate data to inform invasion extent and potential risk, respectively (Jetz et al., 2019).

Advances in the detection and classification of plant species utilizing remote sensing have opened the door for rapid and accurate mapping (Bradley, 2014; Huang and Asner, 2009; Royimani et al., 2019). Winter annual grass species, like cheatgrass, have been mapped with land surface phenology (LSP) estimated from satellites like the Moderate Resolution Imaging Spectroradiometer (MODIS; Bradley and Mustard 2008; Boyte and Wylie 2016; Bradley et al., 2017; West et al., 2017). However, the introduction of new species that exhibit similar phenological attributes

may reduce confidence in models based solely on phenology. In regions with multiple winter annual grass species, models using LSP alone likely capture a combination of these grass species (Pastick et al., 2020).

An inherent challenge with using earth observation (EO) data to classify species presence is the discrepancy between the spatial grain of datasets like MODIS and the abundance of invasive populations. This difference may obfuscate the LSP signal exhibited by these species' presence, reducing the reliability of models based on this data. EO data with increased spatial or spectral resolution can more readily capture these populations (Irisarri et al., 2009; Noujdina and Ustin, 2008; Olsson et al., 2011; Rupasinghe and Chow-Fraser, 2021; Ustin et al., 2002), but cost and spatial and temporal coverage across large extents can become a more limiting factor. Another, more cost-effective, option to mitigate the spatial limitations of a sensor like MODIS is using spatio-temporal image fusion to blend the spatial characteristics of Landsat with the temporal characteristics of MODIS.

Improved annual grass species discrimination may also be possible by combining climatic and remote sensing predictors (Zimmermann et al., 2007). Environmental information is needed to draw relationships between the species and relatively stable features of the physical environment (Franklin, 2010). Habitat suitability models have routinely been employed to determine the potential distribution of invasive species by capitalizing on correlative relationships (Austin, 2007; Elith, 2016; Franklin, 2010). Remote sensing has also recently been used in habitat suitability models (He et al., 2015). Still, by using remote sensing data, these models may inadvertently be mapping something closer to the present distribution of the species (Bradley et al., 2012).

In this study, we developed and assessed three models to predict the presence of *ventenata* across the Blue Mountains Ecoregion (BME) of the interior Pacific Northwest, 1) a hybrid model that incorporates phenology, climatic, and topo-edaphic predictors, 2) a bioclimatic model using only climatic and topo-edaphic

predictors, and 3) a phenology model using only phenology predictors derived from a time series of Landsat images enhanced with images produced with image fusion. Henceforth, we refer to each of these as the hybrid, bioclimatic, and phenology models, respectively. Our objectives were to 1) produce a model with the best possible discrimination power to predict and map *ventenata* within the BME, 2) evaluate the discriminatory capacity of the three models, 3) determine which predictors of *ventenata* presence were most influential and how these relate to the probability of *ventenata* presence, and 4) compare and contrast the predictions between the three models.

3.3 Methods

3.3.1 Study Area

The BME is a complex of mountains, valleys, and plateaus covering approximately 71,000 km² of the interior Pacific Northwest (Figure 3.1; Omernik, 1987). The Cascade Mountains border this region to the west and the Rocky Mountains to the east. Consequently, the BME flora represents a transition between these major mountain ranges where the BME's unique geology drives local community composition. Grasslands, including remnants of Palouse Prairie, are mostly present in the northern portion of the ecoregion, while shrublands, dominated by sagebrush (*Artemisia spp.*) and Western juniper (*Juniperus occidentalis*) woodlands, are more common in the south. A large portion of the region is forested, of which the majority is dominated by ponderosa pine (*Pinus ponderosa*), but parts of the region also support dry and moist mixed conifer and subalpine forests. Elevation ranges from 235 m at the Snake River along the Washington-Idaho border to 2,997 meter at Sacajawea Peak in the Wallowa Mountains. The BME's climate varies widely in terms of annual temperature and precipitation but can generally be characterized by dry summers and cold winters. Precipitation is primarily received as snow and rain during the winter and spring seasons, with annual totals from 20 to 195 centimeters (PRISM Climate Group,

2012). Mean annual temperatures range from -1 to 13°C (PRISM Climate Group, 2012). Soil moisture regimes are xeric or aridic in the lower elevations and transition to udic in higher elevations. A low to high soil productivity gradient generally exists along the elevational gradient partially because of the change in erosion rate and partially from the higher abundance of volcanic ash residing in the region's higher elevations (Clarke and Bryce, 1997).

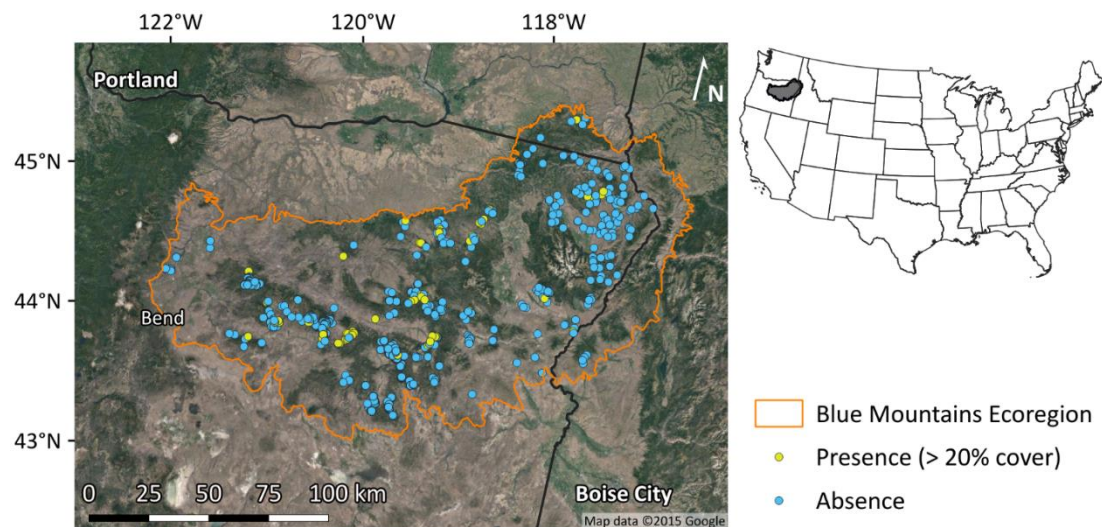


Figure 3.1. Location of *ventenata* presence and absence observations throughout the Blue Mountains Ecoregion.

3.3.2 Data

3.3.2.1 Field Observations

While the availability of spatially referenced species data has increased in recent past, acquiring an adequate number of observations for modeling across large spatial extents is still a challenge (Bradley et al., 2018). Since a sufficient sample size from a single sampling design was not available for the BME, we compiled records of *ventenata* presence, absence, and abundance from multiple sources. These data were evaluated for spatial accuracy and temporal proximity to the modeling time frame. Observations were retained if they were recorded within one year of 2017 and if the plot size was close to 900 m^2 . When multiple observations occurred within 30 m, the observation with the best combination of

temporal proximity to the focal year, spatial accuracy, and plot size was retained. The resulting dataset had 944 observations split between nine sources: the United States Forest Service (USFS; Forest Inventory and Analysis Program data), Bureau of Land Management (Greater Sage-Grouse monitoring data; A.E. Dean, unpublished), and Oregon State University (K. Hogrefe, unpublished; J.D. Johnston, unpublished; Lawrence, 2015; T.C. Nietupski, unpublished; Downing et al., 2019; Tortorelli et al., 2020).

To date, models of grass abundance or cover have achieved relatively minor success using moderate resolution LSP (Bradley et al., 2017). Previous studies have noted that phenological patterns are only discernable once populations reached a certain cover threshold. Similar to studies of cheatgrass, we classified ventenata observations with greater than 20 percent cover as presence (Bradley et al., 2017; West et al., 2017). Throughout the remainder of the manuscript, it is important to consider that this threshold was used to classify presence because presence in this case signifies a substantial level of invasion. This level of invasion can influence the local plant community composition, structure, and fire behavior (Bradley et al., 2017; Endress et al., 2020). The final dataset had 94 presences and 850 absences, 156 of which had ventenata cover between 0.1 and 20% (Figure 3.1).

3.3.2.2 Remote Sensing

Image fusion can be used to fill missing data in higher resolution EO datasets like Landsat (Belgiu and Stein, 2019), thus allowing for finer spatial resolution estimates of annual LSP (Gao et al., 2017). A time series of normalized difference vegetation index (NDVI) from Landsat 8 and images synthesized through image fusion were used to estimate LSP for 2017 (Nietupski et al., 2021). The combination of the Landsat 8 and fused images resulted in a near-daily observation interval at 30 m resolution. The time series was smoothed and annual phenometrics were extracted using a double logistic function. Phenometrics represent different aspects of the annual cycle, including the day of year (DOY) associated with transitions to

and from a dormant state, the NDVI related to different transition dates, and the rate of change at various transition points. These phenometrics vary from year to year as a result of the vegetation composition and yearly weather patterns. The smoothing and extraction process resulted in 11 phenometrics characterizing the seasonal pattern in reflectance. Further details on the methods used for image fusion and phenometric extraction can be found in Nietupski et al. (2021).

The cumulative growing degree days (GDD) from the beginning of the year were also determined at five transition dates (start of green-up, start of season, maturity, end of season, dormancy). These metrics account for temperature-driven plant development and may have lower interannual variability than DOY metrics (Russelle et al., 1984). Daily minimum and maximum temperatures were used to calculate GDD following

$$GDD = \begin{cases} (7 - T_{base}), & \text{if } (T_{max} + T_{min})/2 < 7 \\ (30 - T_{base}), & \text{if } (T_{max} + T_{min})/2 > 30 \\ (T_{max} + T_{min})/2 - T_{base}, & \text{otherwise} \end{cases} \quad (2.1)$$

where T_{max} is the maximum daily temperature in Celsius, T_{min} is the minimum daily temperature in Celsius, and T_{base} is the base temperature for ventenata in Celsius. The T_{base} (i.e, minimum temperature threshold) for ventenata is 7°C (Wallace et al., 2015). Mean daily temperatures outside a ventenata-specific range were censored because plant development is unlikely under these conditions (McMaster and Wilhelm, 1997). The maximum temperature threshold was set at 30°C. This threshold was determined for cheatgrass (Thill et al., 1984) and has been used as an approximation for ventenata (Wallace et al., 2015). The climate data used to calculate GDD metrics were acquired from the PRISM (Parameter-elevation Relationships on Independent Slopes Model) Climate Group, which provides daily gridded estimates of historic temperature and precipitation at 4 km resolution (PRISM Climate Group, 2012).

3.3.2.3 Climatic and Topo-edaphic

Climate, soils, and terrain data were used to define the relatively stable aspects of the physical environment. Climatic conditions were determined from long-term annual and monthly PRISM climate data (800 m; PRISM Climate Group, 2012). Seasonal climate was calculated from monthly data, where seasonal means were weighted by the days per month. The seasons were defined as spring (April-June), summer (July-September), fall (October-December), and winter (January-March). Within the BME, these seasons represent distinct periods of climatic condition from year to year. Climate metrics were resampled to a 30 m grid for prediction. Soil texture in the top 20 cm of the soil profile was derived from gridded Soil Survey Geographic Database (Soil Survey Staff 2015). The missing data was filled with Soil Resource Inventory data from the USFS. Only the top layer of the soil profile was considered due to its importance for shallow-rooted species. Terrain attributes, including slope percent, eastness, and northness were calculated from the National Elevation Dataset (NED; Gesch et al., 2018). Appendix E provides a summary of all predictors used in this study.

3.3.3 Modeling

3.3.3.1 Development

Supervised classification of *ventenata* presence for the three models was performed using the random forest (RF) algorithm. These models differed by their inclusion of different covariate groups and were split as follows: 1) hybrid (48 predictors), 2) bioclimatic (32 predictors), and 3) phenology (16 predictors). The RF classifier uses an ensemble of decision trees (CART) combined to form a prediction through a majority voting process (Breiman, 2001). The trees are created by employing bagging to randomly select training samples, with replacement, to create each tree. This method uses approximately two-thirds of the original observations in each sample and retains approximately one-third as 'out-of-bag' observations. Within each node of each tree, RF searches across a random subset of the features

and determines a binary partition to maximize the dissimilarity between classes (Cutler et al., 2007). The probability of each class is estimated by the proportion of out-of-bag predictions in each class.

The RF algorithm applied in this analysis was implemented through the Python package XGBoost (Chen and Guestrin, 2016). Tuning parameters were determined through cross-validated grid search to maximize discriminatory capacity and reduce overfitting. A few parameters must be set to fixed values to fit a RF-style model in XGBoost. Other parameters may be adjusted to control for overfitting or improve model performance for low prevalence data. Parameters were adjusted and determined in sequence and included the total number of trees (number estimators), the maximum depth of the trees (maximum depth), the minimum number of observations per node (minimum child weight), the minimum loss reduction required to make another partition (gamma), and the weight given to classes (scale positive weight). Applying this process ensured that the model would perform well with an unbalanced dataset.

Table 3.1. RF model parameters determined through grid search.

Parameter	Model		
	Hybrid	Bioclimatic	Phenology
Number Estimators	100	500	900
Max Depth	7	3	6
Min Child Weight	3	1	4
Gamma	0.1	0.4	0.1
Scale Positive Weight	9	11	13

3.3.3.2 Evaluation

Overall model performance was evaluated using k-fold cross validation (k=10). Multiple evaluation metrics were selected to characterize the model's discriminatory power with threshold independent and dependent approaches (Fielding, 2002). The area under the receiver operator characteristic curve (AUC) was

used to determine discriminatory power. Threshold dependent measures included accuracy, sensitivity, and specificity (Cohen, 1960; Fielding and Bell, 1997).

Determination of an appropriate probability threshold to distinguish presence and absence observations was required to assess the overall model performance using threshold-dependent metrics. To calculate the threshold for each of the three models, we simulated model performance 1,000 times with the parameters determined by the grid search process. Data were randomly partitioned into training and testing sets while preserving the prevalence of the original data. For each of these partitions, a model was fit on the training data (80 percent) using the three covariate combinations (hybrid, bioclimatic, phenology) and evaluated with the testing data (20 percent). The kappa statistic was calculated for each iteration at 0.01 increments across the probability range, and the median threshold that maximized kappa was retained to distinguish presence and absence (Freeman and Moisen, 2008). This process resulted in the thresholds of 0.58, 0.73, and 0.7 for the hybrid, bioclimatic, and phenology models. These values were used for all threshold dependent evaluations of the three models.

Elevation and vegetation classes were used to investigate patterns in the predictive performance that might not be captured by overall performance. The regional elevation range was evenly split into eight classes between 610 and 1,830 m, with two additional classes representing elevations below 610 or above 1,830 m. Vegetation classes were determined from the potential natural vegetation (PNV) type map developed by the USFS, Pacific Northwest Research Station (Simpson et al., 2019). Classes were associated with each record, and evaluation metrics were calculated from cross-validation datasets (1,000 random 80-20 partitions). Some vegetation classes contained few records. Therefore, model performance was evaluated in each class by aggregating evaluation metrics from 1,000 cross-validation datasets (80/20 train/test partitions).

3.4 Results

3.4.1 Model Performance

Model evaluation indicates that the hybrid model performed best in terms of threshold independent and threshold dependent metrics (Table 3.2). All three models resulted in a similar performance in accuracy and specificity but differed most substantially in sensitivity. The AUC resulting from the k-fold validation of these models indicates that all models achieved a relatively high-performance level in distinguishing the presence and absence of *ventenata* (Figure 3.2). However, when considering the variation in AUC, as indicated by the interquartile range (IQR) from the cross-validation, the hybrid model consistently performed slightly better than the other models.

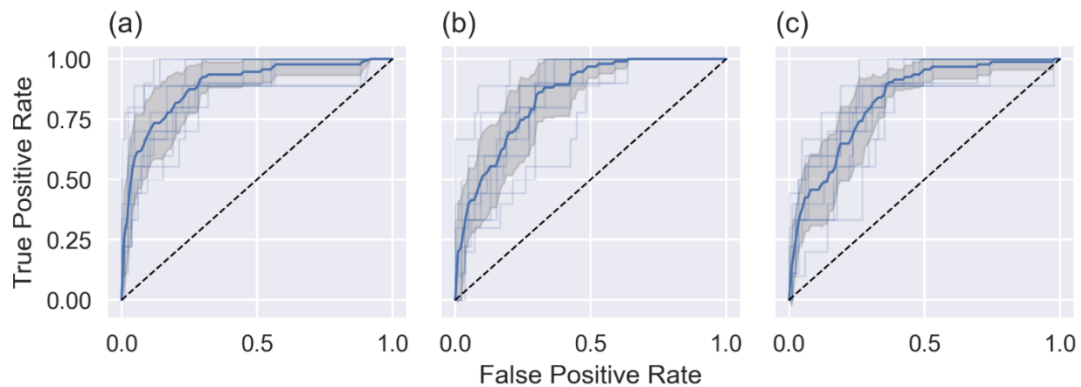


Figure 3.2. ROC curves for each of the (a) hybrid, (b) bioclimatic, and (c) phenology models. The bold blue line shows the mean ROC curve from the k-fold ($k=10$) cross validation. The light blue lines show the ROC curve for each fold and the grey band shows the variation in the ROC curves. The dashed line-of-equality represents an AUC of 0.5 and is interpreted as performance of a model with random predictions.

Table 3.2. Mean and IQR of evaluation metrics showing the overall model performance for each of the three models. Threshold-dependent metrics were calculated based on thresholds of 0.58 (hybrid), 0.73 (bioclimatic), and 0.7 (phenology).

Model	AUC	Accuracy	Sensitivity	Specificity
Hybrid	0.89 (0.044)	0.9 (0.021)	0.54 (0.275)	0.94 (0.032)
Bioclimatic	0.85 (0.041)	0.89 (0.038)	0.39 (0.347)	0.95 (0.041)
Phenology	0.83 (0.089)	0.88 (0.047)	0.41 (0.167)	0.94 (0.05)

Evaluation metrics within each elevation and vegetation class showed generally similar results to the overall model performance. However, evaluating performance by elevation revealed model differences that are not represented in the overall model performance. Notably, while the phenology model's performance is similar to the hybrid and bioclimatic models in the 915 to 1680 elevation range, its performance decreases below 915 m (Table 3.3). When evaluated by vegetation class, the hybrid model had higher accuracy than either of the other two models in scabland shrub and upland shrub types but lower accuracy in moist white fir – grand fir. The hybrid model also had higher sensitivity across all vegetation types, with the most noteworthy differences occurring in scabland shrub, upland shrub, xeric pine, and moist Douglas-fir. Measures of specificity were similar between the three models for most vegetation types but marginally higher for the hybrid model in scabland shrub and lower for moist white fir – grand fir. For further information about model performance by PNV type, see Table G.1 in Appendix G.

Table 3.3. Summary of model performance by elevation class with sample size, ventenata prevalence, and the percent area of the Blue Mountains Ecoregion. Models are abbreviated as HY (hybrid), BIO (bioclimatic), and PHEN (phenology). In some cases, sensitivity could not be calculated because the class did not have any presence observations. Interquartile range of accuracy, sensitivity, and specificity are in parenthesis.

Elevation Class	% of BME	n	Prevalence	Accuracy			Sensitivity			Specificity		
				HY	BIO	PHEN	HY	BIO	PHEN	HY	BIO	PHEN
< 610	2	2	0	1 (0)	1 (0)	0 (1)	-	-	-	1 (0)	1 (0)	0 (1)
610-762	3	7	0	1 (0)	1 (0)	1 (0.5)	-	-	-	1 (0)	1 (0)	1 (0.5)
762-914	7	22	0	1 (0)	1 (0)	1 (0)	-	-	-	1 (0)	1 (0)	1 (0)
914-1,067	12	36	0.19	0.71 (0.2)	0.71 (0.23)	0.71 (0.23)	0 (0)	0 (0.33)	0 (0)	0.89 (0.25)	0.86 (0.25)	0.9 (0.2)
1,067-1,219	15	45	0.09	0.9 (0.18)	0.78 (0.21)	0.83 (0.16)	1 (1)	0.5 (1)	0 (0.58)	1 (0.14)	0.82 (0.2)	0.89 (0.18)
1,219-1,372	18	131	0.15	0.84 (0.09)	0.77 (0.1)	0.82 (0.09)	0.67 (0.3)	0.5 (0.33)	0.5 (0.33)	0.88 (0.1)	0.82 (0.11)	0.89 (0.09)
1,372-1,524	18	238	0.22	0.83 (0.07)	0.83 (0.06)	0.8 (0.07)	0.58 (0.2)	0.45 (0.19)	0.43 (0.21)	0.9 (0.08)	0.94 (0.06)	0.91 (0.06)
1,524-1,676	12	307	0.03	0.96 (0.03)	0.97 (0.03)	0.97 (0.03)	0 (0.33)	0 (0)	0.4 (0.5)	0.98 (0.03)	1 (0)	0.98 (0.03)
1,676-1,829	6	156	0	1 (0)	1 (0)	1 (0)	-	-	-	1 (0)	1 (0)	1 (0)
> 1,829	6	0	0	-	-	-	-	-	-	-	-	-

3.4.2 Model Interpretation

Predictors shared between each of the three models had similar rank and importance in each model (Figure 3.3). The top ten predictors from the hybrid model were split between phenology and climate. The top few climate predictors were similar between the hybrid and bioclimatic models but without the phenology to help differentiate *ventenata* from the absence class, the soil predictors became more critical in the model (Appendix F). None of the terrain related metrics were ranked highly in either of the models in which they were included.

The phenology predictors with the greatest importance in the hybrid and phenology models were NDVI_min, SOG, GDD_at_EOS, and EOS (Figure 3.3). The climate predictors ranked as most important in the hybrid and bioclimatic models included Wint_Tmax, Fall_Tmax, Wint_Ppt, and Wint_MaxVPD. Appendix F provides importance plots for the bioclimatic and phenology models.

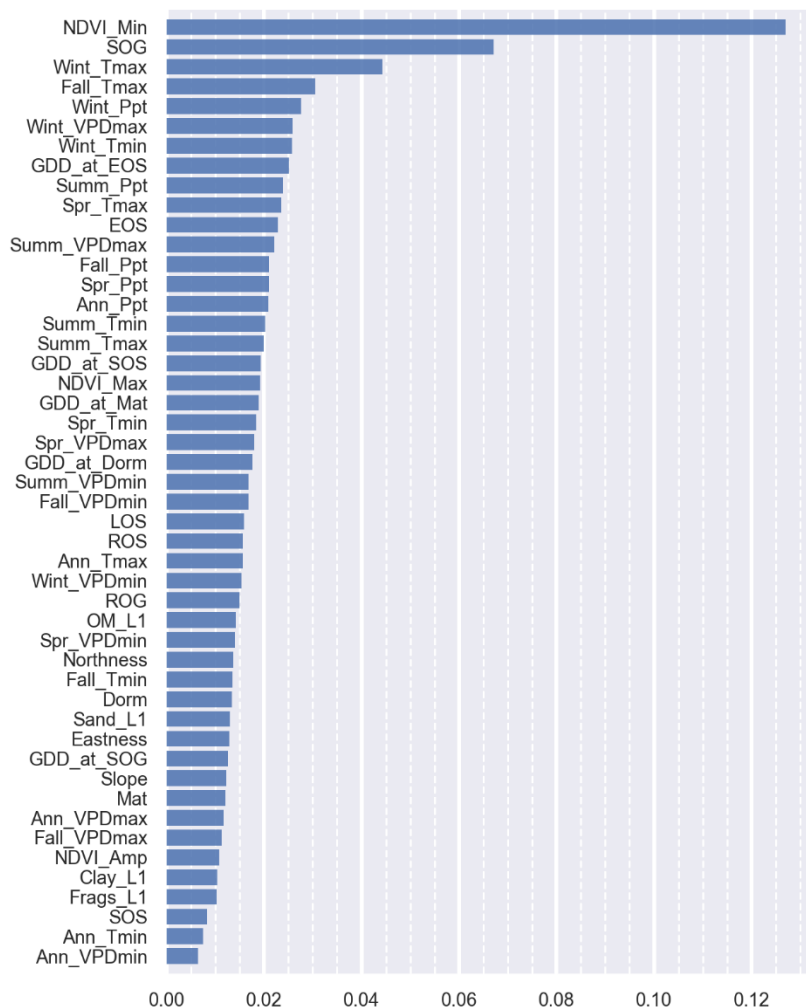


Figure 3.3. Importance and rank of the 48 predictors included in the hybrid model. Descriptions of the individual covariate codes can be found in Appendix E.

The hybrid model's partial dependence plots reveal the strength and direction of the relationship between the predictors and the probability of *Ventenata* presence. *Ventenata* presence was associated with lower baseline NDVI values, earlier start of green-up, and lower cumulative growing degree days at the end of the season (Figure 3.4). *Ventenata* was also associated with higher fall and winter maximum temperatures and relatively moderate winter precipitation. There appears to be a strong threshold for winter and fall temperatures below about 5.5 and 6.5 degrees, respectively.

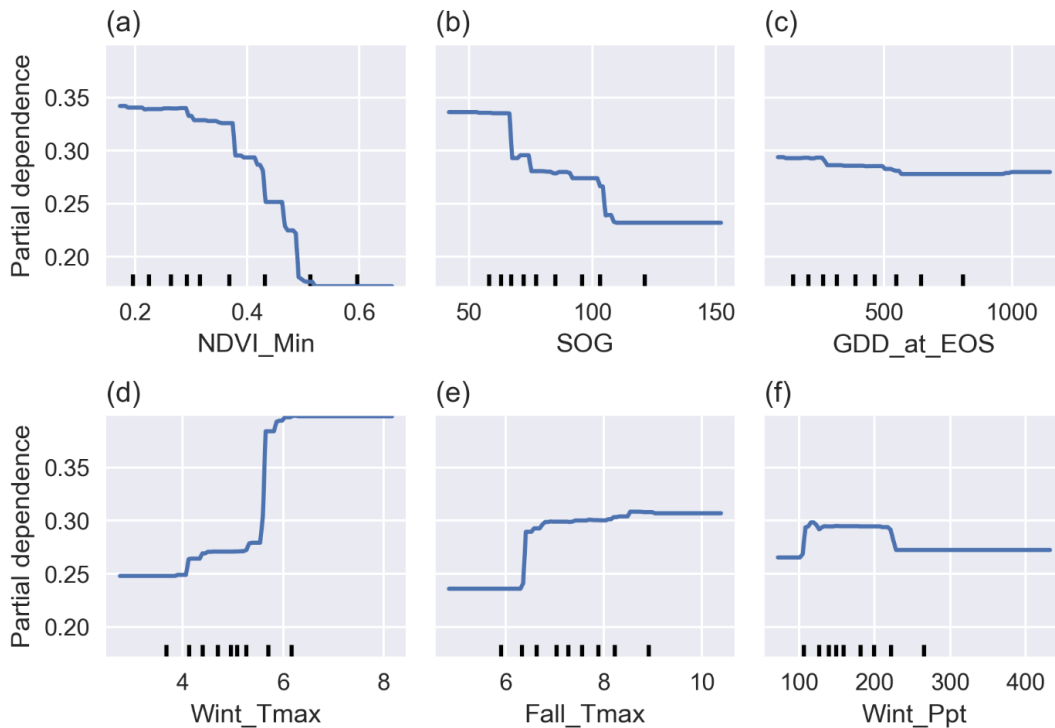


Figure 3.4. Partial dependence plots from the hybrid model indicating the average relationship between the probability of ventenata presence and the predictors. Tick marks in the rug plot along the x axis indicate deciles from the training dataset. Appendix E provides a description of each predictor. Units of the x-axes include a) NDVI, b) day of year, c) degrees Celsius, d) degrees Celsius, e) degrees Celsius, and f) millimeters.

3.4.3 Predicted Distribution

Based on the hybrid model, approximately 5,454 km² of the BME may have contained populations of ventenata in 2017 (Figure 3.5, top panel), equating to about 7.7 percent of the region. Both the bioclimatic and phenology models predicted greater area invaded with nearly 5,986 km² (8.4 percent) and 7,441 km² (10.5 percent), respectively.

There are a few notable differences in the predictions between the three models when focusing on the areas above the presence threshold (highlighted in yellow to red). A comparison between the hybrid and bioclimatic models shows that the hybrid model predicts presence (at greater than 20% cover) in a subset of the

area predicted by in the bioclimatic model. However, the inclusion of phenology in the hybrid model resulted in presence within the northwestern part of the BME and absence in the far eastern part of the region, along Hells Canyon. Comparison between the hybrid and phenology models also shows the hybrid model presence in a subset of the area predicted with the phenology model. In this case, the phenology model shows presence broadly, including lower elevations and substantial parts of the southern and western parts of the region. Figure 3.5 shows the prediction from each of the three models where areas considered presence, based on the threshold the maximizes kappa, are indicated by the yellow to red portion of the color ramp.

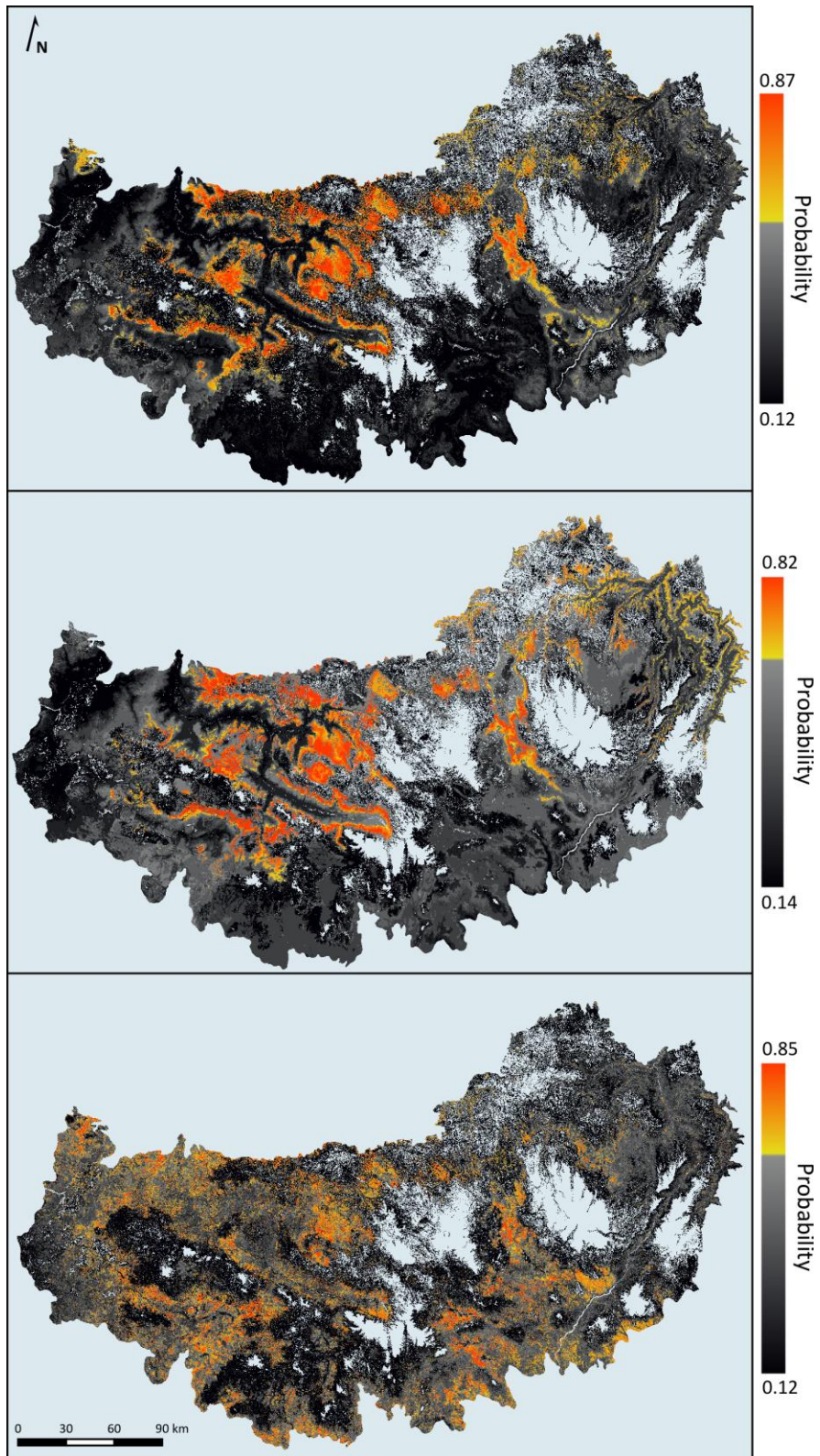


Figure 3.5. Predictions (probability) from the hybrid model (top panel), the bioclimatic model (middle panel), and the phenology model (bottom panel). The

color ramp is split at the presence threshold (i.e., the threshold that maximizes kappa; hybrid=0.58, bioclimatic=0.73, phenology=0.7), where areas above the threshold (presence) are colored in yellow to red and areas below the threshold (absence) are colored in grey to black. Masked areas are outside the BME or are presumed to be currently uninhabitable due to high elevation, high forest canopy cover, or perennial water.

Calculating the probability difference between the hybrid model and the other two models also illustrates the effect of including both predictor sets (top panel, Figure 3.6). The bioclimatic model generally predicted a higher probability across much of the BME. Within the higher elevation areas across the region, locations with high conifer canopy cover had much higher probability in the bioclimatic model (see Figure 3.1 for the location of forested areas). In contrast, some forest openings had higher probability in the hybrid model. In general, the hybrid model predicted higher probability across the higher elevations and lower probability across lower elevations when compared to the phenology model. The greatest differences in probability between the hybrid and phenology models were located along the southern and northwestern portions of the BME. The spatial patterns of negative difference (phenology greater than hybrid) between these models closely align with the area predicted as cheatgrass by another recent phenology modeling effort (bottom panel, Figure 3.6).

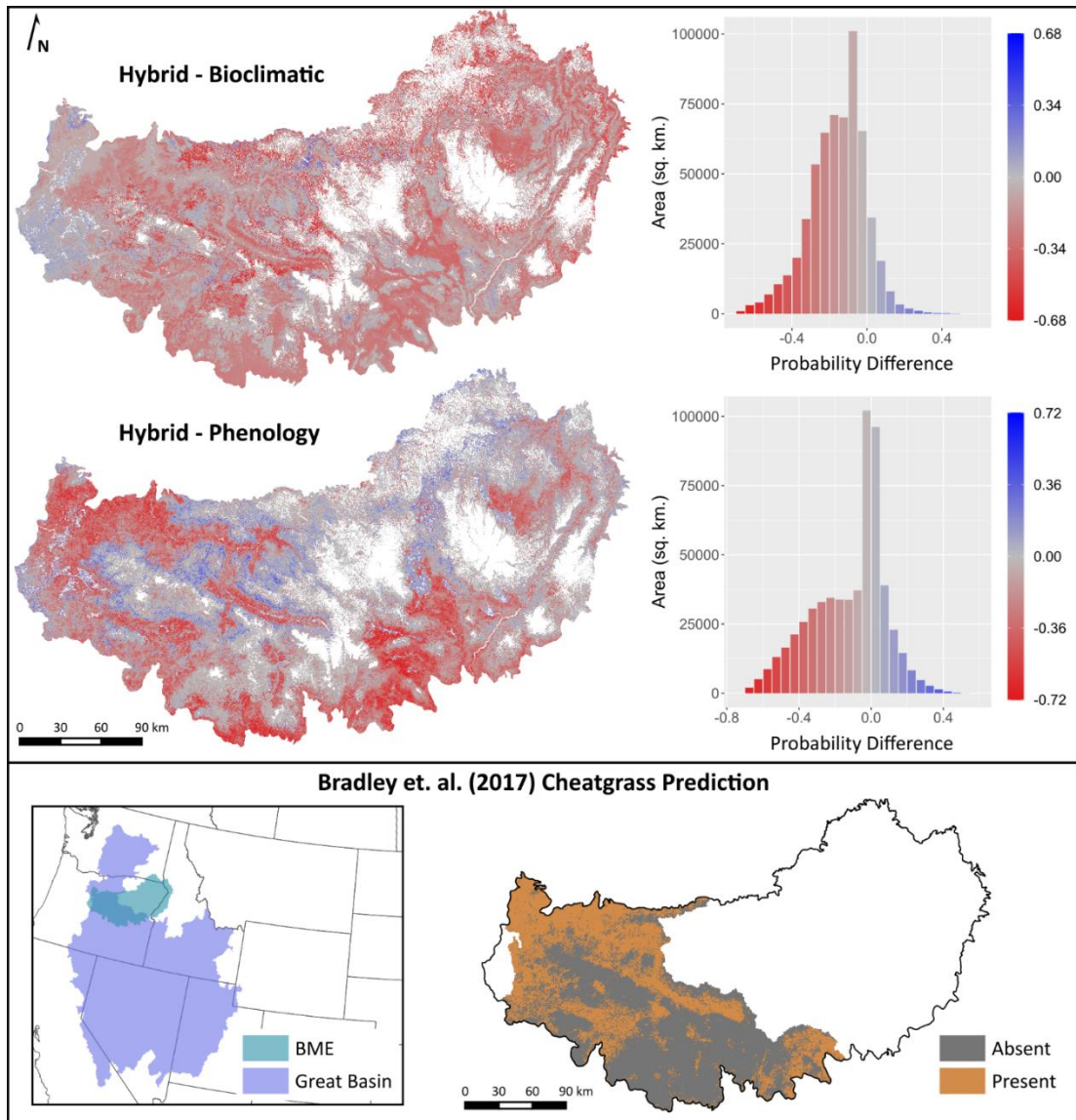


Figure 3.6. The difference between probability where the bioclimatic and phenology models are subtracted from the hybrid model (Top panel). Blue colors indicate that the hybrid model predicts higher probability while red colors indicate that the bioclimatic or phenology model predict higher probability. Predicted cheatgrass presence within a subset of the BME showing the similarity of spatial patterns to the difference between the hybrid and phenology model (Bottom panel).

3.4.4 Elevation and Vegetation Associations

Presence from the hybrid model was primarily located within the elevation range of 946 and 1,451 m (90 percent quantile interval, Table 3.4). The elevational range for the bioclimatic model was also similar but the lower bound of the

elevations associated with ventenata presence were shifted down in the phenology model (753 to 1,495). Based on the hybrid model, approximately 73 percent of ventenata presence is found within upland shrub, juniper woodland, xeric pine, and dry ponderosa pine PNV types. Although upland shrub and juniper woodlands have the greatest area of ventenata invasion, the proportion of these classes invaded by ventenata is lower than dry ponderosa pine and xeric pine (Figure 3.7).

Table 3.4. Summary of total area and percentiles of elevation for six probability classes for the hybrid model. The probability range above and below the threshold that maximizes kappa was split into three equal classes.

Threshold	Probability Class	Area (km ²)	Percent of BME Area	5 th	95 th
				Percentile of Elevation (m)	Percentile of Elevation (m)
Absence	0.12 – 0.27	34,191	48.2	700	1,725
	0.27 – 0.42	12,895	18.2	686	1,559
	0.42 – 0.58	6,212	8.8	823	1,504
Presence	0.58 – 0.67	2,016	2.8	888	1,476
	0.67 – 0.76	1,637	2.3	969	1,450
	0.76 – 0.86	1,801	2.5	1,061	1,419

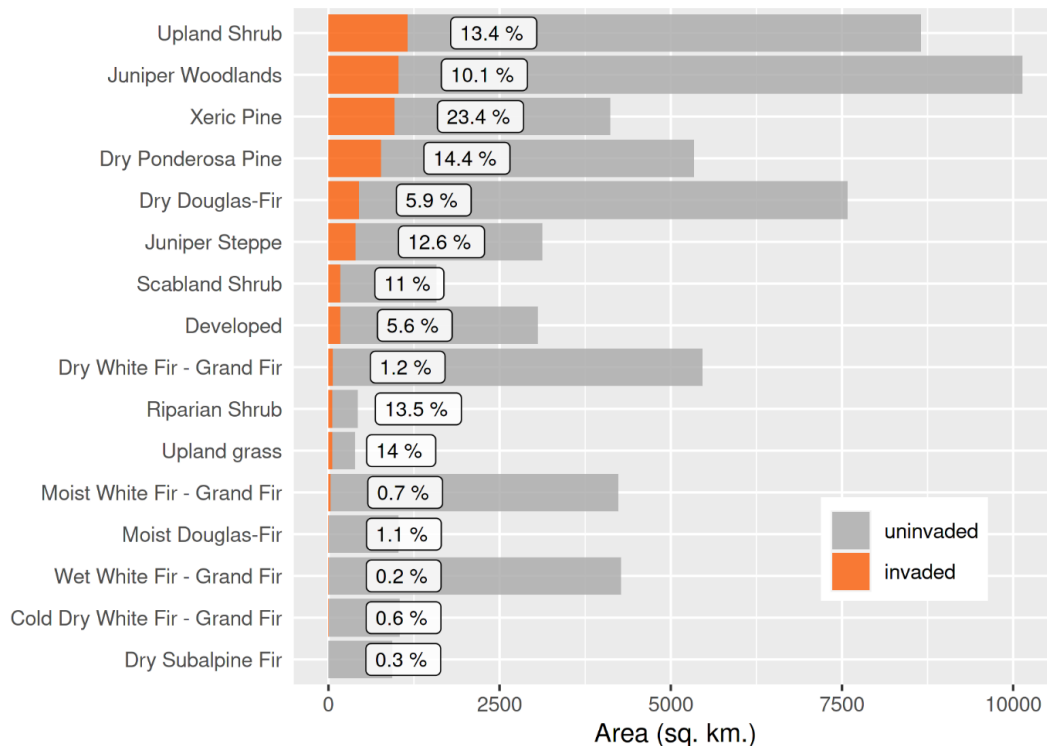


Figure 3.7. PNV types with greater than 0.1 percent area of ventenata and greater than 0.5 percent area of the BME. The invaded area (orange) and uninvaded area (grey), according to the hybrid model (greater than 0.58 probability), is shown for each PNV type. The percent of each PNV type invaded by ventenata is reported as an inset. PNV types are presented in descending order by proportion of total invaded area.

3.5 Discussion

3.5.1 Regional Assessment

The best performing model (hybrid) of ventenata in the Blue Mountains Ecoregion illustrates that there may be a significant portion of the region (7.7 %) already invaded. Unlike previously published maps of cheatgrass for this same region, the hybrid model predicts that many of the invaded areas are found in openings within forested areas and along the forest and shrublands' ecotones (Figures 3.1, 3.5, and 3.6). This pattern expands the potential impact of annual grass invasion in the region and may have broad implications across the western US where ventenata is currently invading.

Our bioclimatic model also shows that a substantial portion of the region is vulnerable to future invasion, and output from this model conceptually represents potential suitable habitat for *ventenata*. Albeit, by constraining the ground truth data (e.g., greater than 20 % *ventenata* cover, scale, etc.), the model is likely restricted to a narrower representation of *ventenata*'s realized environmental niche. Areas with low probability in the hybrid model and higher probability in the bioclimatic model are found throughout the Malheur National Forest's southern extent, indicating that this part of the region may be especially susceptible to future invasion. The inclusion of phenological predictors in the hybrid model constrains the output to actual ground conditions and species occurrence. Therefore, the hybrid model represents our best estimate of actual *ventenata* occurrence and invasive impact in the region. There are also known populations of *ventenata* that the bioclimatic model did not capture when the probability threshold was applied (i.e., higher omission error). The model that included phenology and climatic predictors (hybrid model) helped identify these areas as having higher probability because the observed phenological patterns were not unlike other locations in the region with *ventenata* presence.

One potential issue with using phenology alone to predict *ventenata* is the coexistence of other annual grasses with similar life cycles. This has not typically been addressed in other studies (Peterson 2005; Clinton et al., 2010; Boyte and Wylie 2016; Bradley et al., 2017), although recent work has recognized the separability issues between multiple collocated invasive annual grasses (Pastick et al., 2020). As a result, relying on phenological predictors alone would likely overestimate the current range and abundance of *ventenata*.

Our comparison with an independently derived model of cheatgrass (Bradley et al., 2017) indicated that reliance on phenology alone might not adequately differentiate *ventenata* and cheatgrass. Areas with the greatest difference between the hybrid and phenology models overlapped with much of the area predicted as

cheatgrass (Figure 3.6). The inclusion of climatic predictors may have helped the hybrid model differentiate between ventenata and cheatgrass in areas where differentiation was not possible based on phenology alone. Conversely, Bradley et al. (2017) predicted cheatgrass in parts of the region known to be dominated by ventenata, such as the eastern Ochoco National Forest and western Malheur National Forest. Although cheatgrass and ventenata exist side-by-side in some locations, it is pertinent to consider that the cheatgrass and ventenata models were based off of relatively high cover thresholds (i.e., 15 percent cover of cheatgrass and 20 percent cover of ventenata) and it is unclear how frequently these species coexist at high cover.

3.5.2 Model Performance

The overall model performance between all three models was similar, but closer examination shows that the hybrid model has some advantages. Similar accuracy between the models was not surprising because low prevalence in training data often leads to models with high accuracy (Fielding and Bell 1997). When training datasets have low prevalence, the overall accuracy can still be high even if the model's ability to identify presence correctly is low because the disproportionate number of absences will increase specificity. In other words, if the dataset had 10 percent prevalence and the model predicted absence in all cases, the overall accuracy would still be 90 percent. It is also worth considering that the probability threshold for presence was not the same for each model. The bioclimatic and phenology models required a much higher probability threshold to discriminate presence and absence. Therefore, the dissimilarity in performance would be greater if all three models were evaluated at the same threshold.

The most notable dissimilarity between the three models was found in the omission error (i.e., false negative rate). Both the bioclimatic and phenology models have overall omission errors 15 and 13 percent higher than the hybrid model, respectively, indicating that these models are less effective at correctly identifying

ventenata presence and more likely to classify an observed presence as an absence. When predicting the extent of an invasive species exclusively with a bioclimatic predictors (i.e., traditional species distribution models), omission errors are considered the most problematic because it is assumed that commission errors will occur simply because the species has yet to spread across the entire landscape (Guisan and Thuiller 2005). Two factors may explain the lower omission error in the hybrid model. First, the hybrid model is likely to predict presence in locations deemed somewhat suitable, that exhibit similar phenological characteristics to ventenata. Especially at the early stages of invasion, it is improbable that samples will be collected across the full range of conditions environmentally suitable to a new invader, so the environmental niche characterized by these models is probably more narrow than the actual suitable range of conditions. Second, the hybrid model will likely predict presence in locations where the phenology is moderately similar to ventenata, but the environmental suitability is high. This scenario could occur when the abundance of ventenata at a particular location is low and thus, the suite of accompanying vegetation has a substantial impact on the phenological pattern, leading to a weaker phenological signal.

At the region level, all three models had similar commission error rates (i.e., false positive rate). However, when assessed by elevation and land cover, there were cases where the bioclimatic commission error rate exceeded that of the phenology and hybrid methods. The bioclimatic model commission error rate was lower for elevations above 1,370 m but higher in elevations between 915 and 1,370 m (Table 3.3). Similarly, the bioclimatic model had lower commission error in dry and moist Douglas-fir (*Pseudotsuga menziesii*) and higher omission error in scabland shrub, upland shrub, and wet meadow vegetation classes (Appendix G). This may reflect the general habitat suitability of these areas leading the bioclimatic model to predict presence, whether or not ventenata had reached these particular locations in 2017.

Conversely, one might expect that excluding bioclimatic and topo-edaphic data altogether would lead to a model with the lowest commission. This did not turn out to be true for the phenology model. The higher commission error produced by the phenology model aligns with our assertion that including environmental data would improve the predictions because it would enhance differentiation of the other winter annual grass species present in the region. Model performance in the lower elevations of the region for the phenology model supports the expectation that environmental information would improve predictive performance. These elevation classes contain much more sagebrush steppe, which has abundant populations of cheatgrass. However, estimating model performance within these parts of the region is comparatively less reliable than other locations as they were sampled less intensively.

3.5.3 Phenological and Climatic Relationships

Concerning the most influential phenology predictors, the partial dependence of SOG further confirms the importance of early plant growth in distinguishing ventenata from native species because the probability of presence increased as the SOG decreased (highest probability below approximately DOY 60). Partial dependence of growing degree days at the end of season also indicated that lower accumulated heat units were associated with the senescence process for ventenata. This relatively early end of season was theorized as a potentially separable feature of ventenata in previous research (Noone, 2013). However, minimum NDVI had the greatest impact on classifying this species. This metric is influenced by the combination of soil, photosynthetically active vegetation, and surface moisture (Nicholson and Farrar 1994). Low minimum NDVI is associated with low vegetation biomass, distinguishing ventenata from the forest, shrub dominated, and riparian areas. In addition to the other phenometrics, these phenological attributes help clarify the annual cycle associated with ventenata in satellite observed LSP.

The climatic predictors that corresponded with *ventenata* populations help define its limiting environmental conditions. The predictors most strongly associated with robust populations of *ventenata* (i.e., greater than 20 percent cover) included average winter maximum temperature, average fall maximum temperature, total winter precipitation, and average winter maximum vapor pressure deficit. As indicated by the partial dependence plots, the probability of *ventenata* sharply increased above 5.5°C for average winter maximum temperature and above 6.5°C for average fall max temperature. Probability of *ventenata* also increases between about 100 and 220 mm of total winter precipitation. Fall and winter temperature and precipitation are vital for winter annual grasses. The fall-winter period is when germination and initial leaf elongation occur, corresponding to the time that plants are most vulnerable (Meyer et al., 1997). While winter maximum temperature was also found to be an important predictor of cheatgrass in this region, it was found that winter precipitation was one of the worst predictors of cheatgrass (Bradley 2009). This, in addition to other observations indicating that *ventenata* is more commonly found in relatively wet locations of sagebrush ecosystems (Jones et al., 2018), may suggest that *ventenata* has higher moisture requirements than cheatgrass during the germination and initial growth period. Wallace et al. (2015) also found that *ventenata* seedling emergence was enhanced by litter cover, which locally increased soil moisture.

3.5.4 Interpretation and Challenges

Based on this study's results, using phenology and bioclimatic predictors together led to the best discrimination of *ventenata* within the BME, a region occupied by a variety of winter annual grasses. However, we note a couple of caveats. First, some spatial patterns are likely related to the mismatch in resolution between the phenology (30 m) and the climate (800 m) datasets. While some spatial patterns may not represent fine scale patterns on the ground, much of the broad-scale patterns portray the distribution *ventenata* populations. Second, the effect of

mixed vegetation on *ventenata* detection is not entirely clear. The influence of *ventenata* presence on observed phenology in a mixed pixel at the start of the season could be disproportionate because many other species are dormant. Conversely, the senescence of *ventenata* may not contribute to the end of season signal because other vegetation within a pixel would still be at an earlier development stage and thus dominate the observed phenology.

3.6 Conclusion

The methods employed in this research advance the capability of predicting higher resolution estimates of the distribution of invasive grasses at a regional scale. This kind of information is critical for effective planning and management of species invasions in an ever-changing socio-ecological landscape (Cheney et al., 2018; Jetz et al., 2019; Funk et al., 2020). The invasion of *ventenata* in relatively small forest openings is now more directly observable because of the high spatial and temporal estimates of land surface phenology. Based on our estimates, *ventenata* may already have populations in as much as 7.7 percent (5,454 km²) of the Blue Mountains Ecoregion. However, substantial portions of the region contain habitable conditions for this species, so continued monitoring will be necessary. Knowledge of the present distribution and suitable habitat of *ventenata* may help create a more realistic prediction of future risk within this and neighboring regions.

Moreover, by applying this modeling method to the historic satellite record we may be able to discern invasion trends over time. The presence of this species within the forest matrix and along ecotones could lead to fire behavior changes in these areas. In serving as a fire vector between forested areas, the long-term impacts of *ventenata* invasion could also lead to region-wide fire behavior changes. When combined with the potential effects of climate change, a grass-fire cycle could develop, leading to alterations to ecosystem state and long-term stability (Kerns et al., 2020). The severity of the potential outcomes of this grass invasion warrants

further investigation to quantify the rate and pattern of spread in addition to testing the fire effects and relationships.

3.7 Acknowledgements

This research was supported in part by the Joint Fire Science Program (Proposal ID: 16-1-596 01-21). Part of the land surface phenology processing done for this research was made possible through a Google Cloud Platform Research Credits grant. We would like to thank those who contributed data to our ventenata database, including numerous members of the Oregon State University community and employees of the USDA Forest Service. We would also like to express gratitude to Bridgett Naylor and Kent Coe for assistance with planning and executing field sampling in 2017 and to Michelle Day for assistance with field sampling and data management.

4 SPATIAL DYNAMICS AND PATTERNS OF RECENT *VENTENATA DUBIA* INVASION IN THE BLUE MOUNTAINS ECOREGION OF THE PACIFIC NORTHWEST

4.1 Abstract

The spatial dynamics of a species invasion can provide essential information about the processes driving the invasion and its potential outcomes or impacts. Invasion patterns may be expressed differently throughout the invaded area depending on environmental conditions and disturbances. Wildfire disturbances, in particular, are noteworthy for their promotion of annual grass invasion in ecosystems across the planet. We used remote sensing to map, characterize, and examine the spatial and temporal trends related to the invasion of *Ventenata dubia* in the Blue Mountains Ecoregion of the Pacific Northwest United States. After controlling for the impact of annual weather conditions on vegetation development, we used remote-sensing-derived land surface phenology to estimate the probable distribution of *ventenata* in 2006 and 2017. Our objectives were to 1) characterize the change in *ventenata*'s distribution both regionally and at a finer scale within two subregions, 2) investigate the landscape characteristics (elevation and vegetation) associated with the expansion, persistence, or contraction of *ventenata* populations, and 3) explore the potential impact of large-wildfire occurrence and severity on *ventenata*'s expansion. Between 2006 and 2017, the total area occupied by *ventenata* increased by more than 40% (378,000 ha to 545,000 ha). During these 11 years, the total number of patches decreased and mean patch size increased, indicating that radial spread was more common than discontinuous expansion. The majority of expansion occurred at higher elevations (> 1,300 m) and within forested and ecotonal environments. Large wildfires within dry-forest and highly mixed forest/non-forest experienced a greater increase in the probability of *ventenata* than similar areas that did not experience large wildfires. High burn severity (RdNBR) was also associated with an increase in the probability of *ventenata* in some parts of the region. These findings provide insight into the spatio-

temporal patterns of the *ventenata* invasion in this region over recent past and suggest that there may be an association between wildfire and this invasion, likely related to the opening of canopy cover in burned areas. However, *ventenata* also expanded in much of the region in the absence of wildfire. The unique information garnered from our analytical approach demonstrates the utility of this type of analysis in providing a backward glance at a relatively recent invasion.

4.2 Introduction

As non-native plant species pass through the stages of invasion, they must establish persistent, self-sustaining populations before spreading to and colonizing new areas (Richardson et al., 2000). Characterizing the spatial dynamics of these species' persistence and spread can provide essential information about processes driving an invasion (Ellner and Schreiber 2012; Mcgeoch and Latombe 2016; Santos et al., 2016) and give insight into potential future outcomes (Giometto et al., 2014). Given the socio-economic impacts of non-native plant invasion (Pimentel et al., 2005; Xu et al., 2006; Scalera 2010), expedient acquisition and synthesis of such information is vital. The study of invasive species distribution change has been and will continue to be improved by the development of technologies and techniques to observe and map species distributions through time (Jetz et al., 2012, 2019; Hardisty et al., 2019).

The impacts that invasive annual grasses have on ecosystem function, composition, and associated fire regimes have been well documented around the world (D'Antonio and Vitousek 1992; Brooks et al., 2004; Kerns et al., 2020). However, studies of invasive plants' impacts rarely last more than a few years and are commonly limited in spatial extent (Stricker et al., 2015). Recently, Balch et al. (2013), Bradley et al. (2017) and Fusco et al. (2019) turned to remote sensing to examine relationships between invasive grass species and fire over larger spatial extents. Although these three authors leveraged long-term records of fire, they were limited to a single snapshot of the invasive grass' distribution and focused on the impact of invasive grass presence on fire occurrence or behavior.

Assessing the change in an invasive species' distribution over time may provide insight into the processes influencing invasion and help to determine whether newly introduced species will influence regional fire behavior. Additionally, examining the relationship between fire occurrence or severity and the change in

invasion patterns or extent may help determine whether fire promotes the invasion of a particular species.

In the western United States, historical fire suppression and land-use practices have already altered forest structure and fire regimes, resulting in larger (Littell et al., 2009; Dennison et al., 2014) and sometimes more severe (Stephens et al., 2014) wildfires. When high-severity wildfire occurs in forested areas, the opening of the forest canopy can in turn expose areas to a greater risk of invasion (Keeley and Brennan 2012; Peeler and Smithwick 2018). If non-native grasses invade these areas, disturbances may occur at an interval frequent enough to suppress forest regeneration, particularly in drier forest stands along ecotones. Ecotones between landscape patches can serve to connect processes occurring in neighboring ecosystems. Therefore, the additional fine fuels in these areas may lead to increased fire spread.

The invasion of *ventenata* (*Ventenata dubia*) in the Blue Mountains Ecoregion (BME) of the Pacific Northwest presents an opportunity to examine the dynamics of spread and persistence of an invasive species. The presence and abundance of this species in forest (Kerns et al., 2020; Tortorelli et al., 2020), shrubland (Jones et al., 2018), and grassland (Averett et al., 2020; Endress et al., 2020) communities of the BME makes *ventenata* a potential threat to these ecosystems and a new source of fine fuels in some of these systems that were historically pyroresistant (Kerns et al., 2020). Until recently, many of the grass invasions documented for their fire-altering effects have occurred within the relatively warmer shrubland ecosystems (Chambers et al., 2007, 2014a) and populations are somewhat limited in the higher elevation forest ecosystems. Within the BME, variation in topo-edaphic and climate conditions has resulted in a heterogeneous arrangement of vegetation patches with abundant ecotonal-edges. The presence of a new source of fine fuels in such areas may increase the risk of future fire-behavior changes (Kerns et al., 2020).

The value of developing an early assessment of the spatial and temporal patterns of ventenata invasion is essential for future planning and research endeavors. Therefore, we examined changes in ventenata's distribution within the BME to identify trends and patterns occurring within environmental associations and to assess whether ventenata responds to wildfire occurrence or severity. The overall objectives of our study were to 1) quantify the spread and persistence of ventenata between 2006 and 2017, 2) characterize the differences between these time points in terms of biophysical associations (elevation and potential natural vegetation), and 3) investigate the relationship between change in the ventenata's distribution and the occurrence and satellite observed severity (RdNBR) of large wildfires within the BME.

4.3 Methods

4.3.1 Study Area

The BME (Figure 4.1; Omernik 1987) is located in the intermountain Pacific Northwest between the Cascade and Rocky Mountains. This region covers approximately 7 million ha of forest, range, and developed land managed by public and private stakeholders. The variation of soil, weather, and terrain within this region are expressed through a complex and heterogeneous composition of forested and non-forested areas with elevations ranging from 235 to 2,997 m. The BME's climate is characterized by dry summers and cold winters, although parts of the region are maritime influenced and receive moisture channeled through the Columbia River Gorge. Precipitation is received during the winter and spring seasons as snow and rain, with annual total precipitation ranging from 20 to 195 cm (PRISM Climate Group, 2012). Mean annual temperatures range from -1 to 13° C (PRISM Climate Group, 2012). A low-to-high soil-productivity gradient exists along the elevational gradient, influencing the plant community composition in concert with climatic conditions (Clarke and Bryce 1997).

Western juniper (*Juniperus occidentalis*) woodlands, shrublands dominated by sagebrush species (*Artemisia spp.*), and grasslands occupy most of the lower elevations of the region. Mid-elevations are split between dry and moist conifer forests and mainly dominated by ponderosa pine (*Pinus ponderosa*), Douglas-fir (*Pseudotsuga menziesii*), and grand fir (*Abies grandis*). The higher elevations are dominated by forests of subalpine fir (*Abies lasiocarpa*), Engelmann spruce (*Picea engelmannii*), and whitebark pine (*Pinus albicaulis*). Less abundant tree species in the region include western larch (*Larix occidentalis*) and lodgepole pine (*Pinus contorta*).

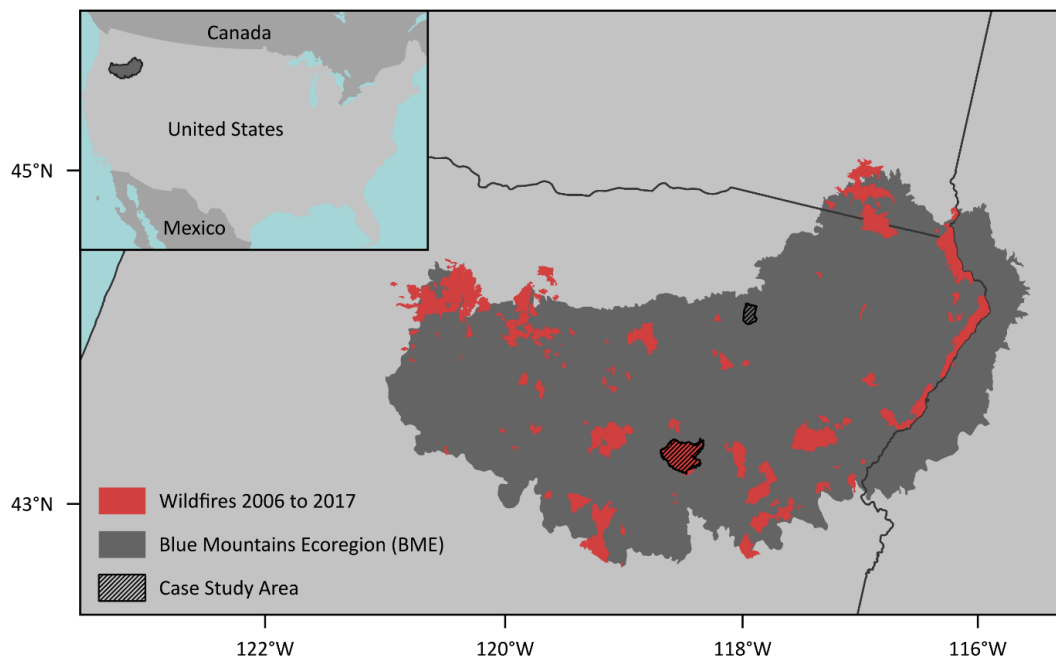


Figure 4.1. The Blue Mountains Ecoregion with case-study areas and wildfires that occurred in Oregon and Washington between 2006 and 2017. Wildfire perimeters were provided by the Monitoring Trends in Burn Severity database (Eidenshink et al., 2007).

4.3.2 Predicting *Venttenata*

4.3.2.1 *Venttenata* Model

We used a random forests (RF) model developed in Chapter 3 to predict the 2017 distribution of *venttenata* within the BME. The model used phenology and

environmental covariates (the hybrid model) to predict the probability of *ventenata* at greater than 20% cover within a given pixel (30 m x 30 m). The model was developed with 944 observations of *ventenata* where presence was classified for all observations with greater than 20% cover. Phenology variables were estimated using a time series of 30 m imagery that spanned the growing season in 2017. Climate variables were determined from annual and monthly PRISM data (PRISM Climate Group, 2012). Seasonal climate variables were calculated from monthly data, where seasons were defined as spring (April-June), summer (July-September), fall (October-December), and winter (January-March); seasonal means (e.g., mean summer maximum temperature) were calculated as weighted averages based on the number of days in each month. Climate variables were then resampled to a 30 m grid for prediction. Soil variables of texture in the top 20 cm of the soil profile were derived from gridded Soil Survey Geographic Database (gSSURGO; Soil Survey Staff 2015). Any missing soils data was filled in with Soil Resource Inventory data from the USFS. Terrain attributes, including slope percent, eastness, and northness were calculated from the National Elevation Dataset (NED; Gesch et al., 2018). A detailed explanation of the data and methods used to train, test, and evaluate this model can be found in Chapter 3. All variables used in the RF model and their descriptions can be found in Appendix E.

An assessment of the RF model's ability to discriminate *ventenata* indicated an overall accuracy of 90%, AUC of 0.89, sensitivity of 0.54, and specificity of 0.94. To classify predictions as presence or absence, we used a threshold of 0.58 (probability). This threshold was found to maximize discrimination between presence and absence (i.e., kappa; Freeman and Moisen 2008) in a simulation during which the model was iteratively re-fit based on a random bootstrap of the modeling dataset.

4.3.2.2 Historical Prediction

To predict the distribution of *ventenata* within the BME for a time prior to 2017, we needed to estimate phenometrics for a year to be used in place of the 2017 phenometrics. We considered years between 2000 and 2016 as MODIS (Moderate Resolution Imaging Spectroradiometer) imagery (used in estimating phenology) is only available after 2000. Through the analysis described below, we determined 2006 to be the most appropriate year. We assumed that all other predictors (i.e., climate normals, topography, and soils) remained constant.

Annual weather patterns are an important driver of plant phenology (Stenseth and Mysterud 2002; Badeck et al., 2004; Penuelas et al., 2010) and have an established relationship with NDVI (Paruelo and Lauenroth 1998; Potter and Brooks 1998; Peters et al., 2002). Therefore, we needed to control for this potential source of variation in our phenological metrics when predicting the distribution of *ventenata* at multiple time points. To control for annual weather patterns, we selected the year from 2000 to 2016 with the closest observed weather similarity to the model development year (2017). To determine similarity, we used monthly time-series data from five RAWS (Remote Automated Weather Stations) stations (<https://wrcc.dri.edu/wraws/orF.html>) and monthly Palmer Drought Severity Index (PDSI) data derived from the nClimDiv dataset (Vose et al., 2014). Within the BME, we selected one RAWS station at every 305 m interval across the elevation gradient for a total of five stations (Board Creek, Flagstaff Hill, Hehe 1, La Grande 1, and Pittsburg Landing). These stations had minimal missing precipitation, relative humidity, and air temperature data. Weather variables were summarized annually and by season and the multivariate Euclidean distance between 2017 and each previous year was calculated for all five RAWS stations' weather data. The monthly time series of PDSI was calculated for climate divisions (<https://www.ncdc.noaa.gov/monitoring-references/maps/us-climate-divisions.php>) from gridded temperature and precipitation data that were interpolated from a

network of weather monitoring stations (excluding RAWS). The climate divisions overlapping the BME were examined and the nearest neighbor (multivariate Euclidean distance) of the monthly PDSI time-series was also calculated.

The year 2006 was determined to be the most similar year to 2017 (Figure 4.2). Although 2013 was slightly more similar to 2017 according to the RAWS data, the preceding year's weather of 2006 (i.e., 2005) was closer to 2017 (i.e., 2016). The preceding years' weather is important for annual grasses like *ventenata* because germination typically starts in the fall and continues through the winter and spring (Wallace et al., 2015). Furthermore, the weather in a given year will influence the seed crop produced by annual species and, therefore, the amount available for germination in following years (Pilliod et al., 2017). In addition to similar RAWS data, 2006 was the most similar to 2017 based on PDSI.

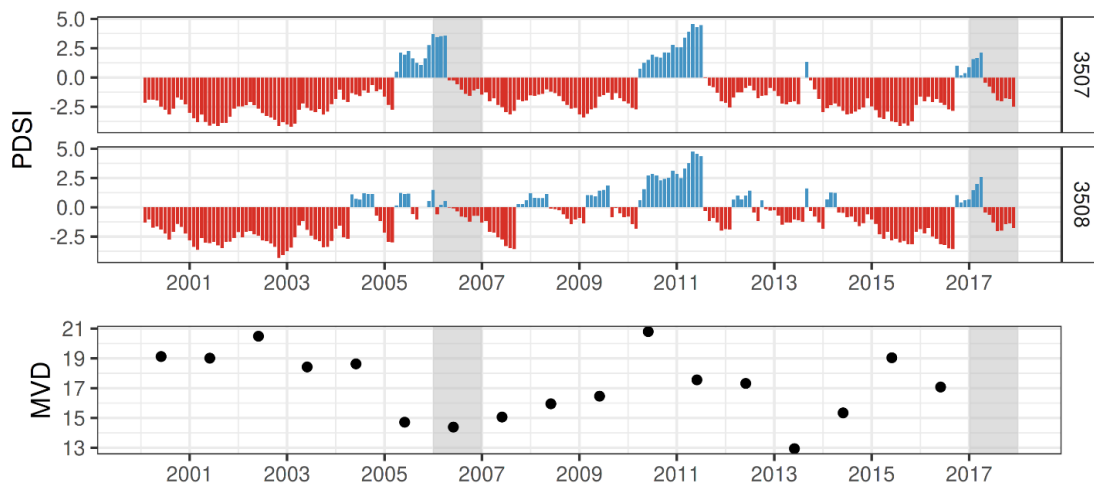


Figure 4.2. Weather similarity between the model development period (2017) and the year selected for historic *ventenata* prediction (2006); the years 2017 and 2006 are shaded by grey bands in each panel. The top two panels show the monthly Palmer Drought Severity Index (PDSI) from 2000 through 2017 within the two climate divisions covering approximately 80 percent of the BME (3507, 3508). Climate division 3507 covers the western BME, and climate division 3508 covers the central to northeastern BME. Positive PDSI values (blue) indicate that the region is in a wet period, while negative values (red) indicate that the region is experiencing drought. The bottom panel depicts the multivariate Euclidean distance (MVD) from 2017 to each year between 2000 and 2016 based on weather data from the five

RAWS stations. Smaller MVD values indicate greater similarity with weather conditions in 2017.

To estimate historic phenology, Landsat 5 surface reflectance and MODIS NBAR (MCD43A4) imagery were acquired for all scenes overlapping the BME and processed using the image fusion and phenometric extraction techniques of Nietupski et al. (2021). These methods produce a daily, 30 m resolution time-series of normalized difference vegetation index (NDVI) by performing an ESTARFM-like image fusion process. This time series was then smoothed with a double-logistic function, from which 11 phenometrics were calculated based on rates-of-change and inflection points. These phenometrics characterized intraannual patterns of vegetation development, including dates of phenophase transition (e.g., start-of-season) and characteristics of the annual curve (e.g., the amplitude of NDVI). To control for minor differences between the Landsat 8 data used for 2017 phenometrics and the Landsat 5 data used for 2006 phenometrics, we applied the linear transformation of Roy et al. (2016) to all Landsat 5 images before image fusion and phenometric extraction. Five additional phenometrics were calculated as the cumulative growing-degree-days at phenophase-transition dates (i.e., SOG, SOS, Mat, EOS, Dorm; Appendix E) based on daily temperature data from PRISM (Parameter-elevation Relationships of Independent Slopes Model; PRISM Climate Group, 2012).

4.3.3 Regional Change

We assessed regional-level change between 2006 and 2017 in terms of changes in probability, spread, and persistence. We evaluate the change in probability by examining the change in probability between 2017 and 2006 (i.e., $probability_{2017} - probability_{2006}$) and the percent-change in probability (i.e., $\left(\frac{change\ in\ probability}{probability_{2006}}\right) \times 100$). To assess spread and persistence, we thresholded 2006 and 2017 predictions (i.e., values $> 0.58 = present$) and classified the difference between these predictions as either locations of absence (where *ventenata* was

absent in both years), expansion (absent in 2006 and present in 2017), persistence (present in both years), and contraction (present in 2006 and absent in 2017). We then summarized the 2006 distribution, 2017 distribution, expansion, persistence, and contraction by total area, number of patches, and patch size. A patch was defined as a contiguous cluster of pixels of the same class (e.g., present in 2006, expansion, persistence, contraction) that included all pixels with one edge or vertex adjacent to another pixel in the same class.

4.3.3.1 Phenology and Biophysical Setting

We assessed changes in *ventenata*'s distribution with respect to phenology, elevation, and potential natural vegetation (PNV; Simpson et al. 2019). Evaluating the phenology shift allowed us to quantify some of the phenology changes leading to predictions for the expansion, persistence, or contraction of *ventenata* populations. We controlled for the effect of weather in the model so large changes in the phenology are likely to be associated with changes in the vegetation composition. We chose phenology predictors highly ranked by variable importance to limit the number of phenology variables examined. We used these phenology predictors to explore the type of phenological change associated with expansion, contraction, and persistence. These variables included start-of-greenup, minimum-NDVI, and end-of-season. This assessment can serve as either a form of model check (e.g., was the expansion associated with earlier greening, as we would expect?) or explanation of factors that led to expansion or contraction (e.g., was contraction associated with increasing minimum NDVI and ingrowth of other vegetation?).

We used elevation and PNV data to assess the changes that occurred in the biophysical setting of *ventenata* invasion between 2006 and 2017. We summarized the elevation associated with expansion, persistence, and contraction using the National Elevation Dataset (NED; Gesch et al., 2018). We used the (PNV) subzones developed by Simpson et al. (2019). The gridded (30 m) PNV dataset covers Oregon and Washington and was developed by the USFS. These data represent the expected

vegetation-community that would develop in a given environment without human intervention or disturbance. Although this dataset does not directly relate to present vegetation communities, we use PNVs to help indicate the long-term habitat associated with the ventenata invasion. To assess the change by PNV, we calculated the total area of ventenata in 2006 and 2017 in each PNV and the entire area of expansion, persistence, and contraction in each PNV. We also calculated the average change in probability by PNV.

4.3.3.2 *Wildfire*

To investigate the relationship between large wildfires (i.e., wildfires > 405 ha) and ventenata populations, we examined how ventenata predictions differed with respect to wildfire occurrence and how predictions changed with increasing burn severity (RdNBR). Although there is concern that ventenata invasion could lead to the development of a grass-fire-cycle (Kerns et al., 2020), we chose to examine only one side of this relationship (i.e., the potential influence of fire on ventenata invasion).

The occurrence of large wildfires was determined from the burned-area boundaries provided by Monitoring Trends in Burn Severity (MTBS) program (downloaded from <https://www.mtbs.gov/direct-download>; Eidenshink et al., 2007). This dataset includes fire perimeters detected using dNBR (delta normalized burn ratio) and RdNBR (relativized delta normalized burn ratio) for fires with a size greater than 405 ha (1,000 ac). From this dataset, we selected wildfires that burned between 2006 and 2017 and had a boundary that overlapped that of the BME. Because ventenata populations are unlikely to be sustained above 1,829 m (Scheinost et al., 2008), we dropped any wildfires with greater than 75 percent of its area above this elevation. This selection process resulted in a total of 119 wildfires (Figure 4.1). For the resulting 119 wildfires, burn severity (RdNBR) was calculated in Google Earth Engine for each wildfire using the methods described in Parks et al. (2018). In short, these methods use a mean-composite calculation of RdNBR and an

offset to improve the reliability of comparing burn severity among fires by accounting for phenological differences between pre- and post-fire imagery.

To examine the relationship between wildfire occurrence and *ventenata*, we first compared wildfire and non-wildfire areas. To identify non-wildfire areas for comparison, we randomly sampled with replacement from the area within the Oregon and Washington portion of the BME that was not included in the MTBS dataset between 2006 and 2017. Although there are small fires within this non-wildfire portion of the BME that burned during this time frame, we chose to focus on large wildfires in our study. We randomly sampled from this non-wildfire area, where each sample was a square in shape and 7,060 ha in size (the median fire size of the 119 wildfires). We also dropped any non-wildfire sample from the analysis if more than 75 percent of its area was above 1,829 m. This resulted in a random sample that covered a total of 83% of the non-burned area of the BME.

The effect of fire occurrence or severity on *ventenata* may change depending on the biotic and abiotic conditions present at the location of the fire. Therefore, to control for the influence of vegetation on the interaction between wildfire and *ventenata*, wildfires and non-wildfire samples were grouped into one of eight fire-vegetation groups (hereafter, fire-veg groups). Each wildfire or non-wildfire sample was assigned to a fire-veg group by first reclassifying PNV subzones as either 'forest' or 'nonforest', where nonforest included shrub, grass, and woodland PNV subzones. Next, to quantify the abundance of ecotones, each wildfire or non-wildfire sample was assigned into one of three categories based on the proportion of its area classified as forest or nonforest: nonforested (more than 75% nonforest), mixed (75-25% nonforest), and forested (less than 25% nonforest). These three groups (i.e., non-forested, mixed, and forested) were then subdivided into 2-3 groups based on the dominant PNV subzone (i.e., the greatest number of pixels) within that wildfire or non-wildfire sample. The resulting eight fire-veg groups were shrubland, woodland, mixed/shrubland, mixed/woodland, mixed/dry-forest, dry-forest, mixed-

conifer, and subalpine. For each wildfire or non-wildfire sample, we then calculated the mean percent-change in the probability of ventenata and compared the distribution of these statistics within a given fire-veg group.

To investigate how increasing burn severity (RdNBR) related to changes in ventenata predictions, we first classified predictions of the percent-change in probability of ventenata into six change classes: less than -50%, three evenly spaced classes between -50% and 100%, 100% to 200%, and greater than 200% increase in the probability of ventenata. Then, to assess how burn severity broadly related to change-class in a fire-veg group, we calculated the median and interquartile range (IQR) of RdNBR by change-class for each wildfire and summarized the distribution of these medians and IQRs for each change-class by the fire-veg group. This calculation aimed to see if, regardless of a particular fire, an increase in RdNBR was broadly associated with increasing ventenata predictions in each of the fire-veg groups.

However, we also wanted a more direct comparison within fire-veg groups of how burn severity compared between change-classes. For example, in the dry-forest group, how does the median burn severity compare between areas with a 50% vs. 200% increase in the probability of ventenata? We again examined the median and IQR of RdNBR by change-class for each wildfire to answer this question. To control for the effect an individual wildfire may have on the difference between change-classes, for each wildfire, we then calculated the pairwise difference in the median and IQR between all change-classes (e.g., the median of the greater than 200% change-class minus that of the less than -50% change-class). For each fire-veg group we then reported the average (mean) difference in the median and IQR between all pairs of change-classes as heatmaps. If ventenata predictions increased with increasing burn severity, we expect to see a larger increase in the mean difference of the median RdNBR for change-classes that are further apart. This allowed us to assess whether, at the fire level, there was an increase in burn severity associated with higher probability areas of ventenata vs lower probability areas.

4.3.4 Case Studies

Given the large extent of the study area, we were interested in examining the spatial patterns of change at a finer scale to explore the change in 1) a typical patchy forest setting and 2) within a recent large wildfire. The first of these case studies is the Starkey Experimental Forest and Range (SEFR). The SEFR represents a typical example of the spatial complexity of forested areas in the BME and can be characterized by stands of conifer trees interspersed with generally long, narrow openings dominated by bunch grasses. Additionally, the SEFR is a long-term study area and *ventenata* has been present in this area since at least the early 2000's (personal communication with Bridgett Naylor, USFS). The SEFR covers approximately 10,125 ha of the north-central part of the BME within the Wallowa-Whitman National Forest (Figure 4.1). Elevation within SEFR ranges from 1,200 to 1,500 m, mean annual precipitation ranges from 52 to 70 cm, and mean annual temperature ranges from 6.5 to 7.5°C.

The second case study is the Canyon Creek Complex that burned approximately 44,400 ha of the Malheur National Forest in the south-central part of the BME (Figure 4.1). The Canyon Creek Complex represents one scenario of the effect of fire occurrence on *ventenata* invasion in a part of the region covering a wide range of vegetation communities from shrubland to subalpine forest. This fire also encompasses ecotonal areas between shrubland and forested areas. The Canyon Creek Complex primarily burned over three weeks starting on August 12th, 2015. Within the burned area, elevation ranges from 1,000 to 2,500 m, mean annual precipitation ranges from 39 to 112 cm, and mean annual temperature ranges from 2 to 8.7°C.

For each case study, we examined the invasion between 2006 and 2017 by summarizing the change using the same methods as the region level and by examining landscape pattern indices. To describe change patterns observed within a landscape, it has been recommended that a range of landscape pattern metrics be

chosen (Gillanders et al., 2008). We decided to include the number of patches, mean patch area, mean minimum distance between patches, and a patch-shape index calculated as the ratio between the width and height of the minimum oriented bounding box (RMOBB). The RMOBB provides a basic assessment of the elongation of patches where values close to 0 represented narrow, long patches and values close to 1 represent square patches. In addition to these measures, we also calculated the mean minimum-distance between expansion and contraction patches and persistence patches. These metrics, in combination, characterize the pattern in the invasion between 2006 and 2017.

4.4 Results

4.4.1 Regional Change

In 2006, an estimated total of 378,000 ha (5.33%) of the BME contained populations of *ventenata* (i.e., greater than 20% areal cover of *ventenata* within a given 900 m² area). By 2017, this increased to a total of 545,000 ha (7.69%) with persistent populations accounting for 320,000 ha (4.55 %). Between 2006 and 2017, *ventenata* expanded into more than 220,000 ha (3.13 %), while only contracting by 55,000 ha (0.78 %). For nearly 14,000 ha of the BME, the probability of *ventenata* populations more than doubled during this period, with some areas having a 570% increase in probability.

Across the BME, there were 15,640 fewer *ventenata* patches in 2017 (140,000 total) than in 2006 (155,000 total). Mean patch size increased from 5.5 ha in 2006 to nearly 7.6 ha in 2017. At both time points, the observed distribution of patch sizes across the region was heavily skewed towards a smaller patch size. When patches of less than 0.09 ha (i.e., single pixel patches) were excluded, the median patch-size was 0.27 ha in 2006 and 0.36 ha in 2017. When populations were grouped into patches based on their categorical classification (i.e., expansion, persistence, contraction), persistent populations accounted for the largest (6.9 ha) and fewest

patches (102,000) when compared to areas that expanded (1.8 ha, 238,000) and contracted (0.6 ha, 184,000).

4.4.1.1 Phenology and Biophysical Setting

The phenological change associated with expansion and contraction was highlighted by differences in some of the most influential phenology predictors (Figure 4.3). On average, expansion populations were associated with an earlier start-of-greenup in 2017 (Figure 4.3B), similar minimum-NDVI (Figure 4.3C), and similar end-of-season (Figure 4.3D). In contrast, contraction populations were associated with a higher minimum-NDVI in 2017, similar or later start-of-greenup, and similar end-of-season. Persistence populations were not associated with substantial phenological change, except for an earlier end-of-season in 2017 that was also observed in expansion and contraction populations.

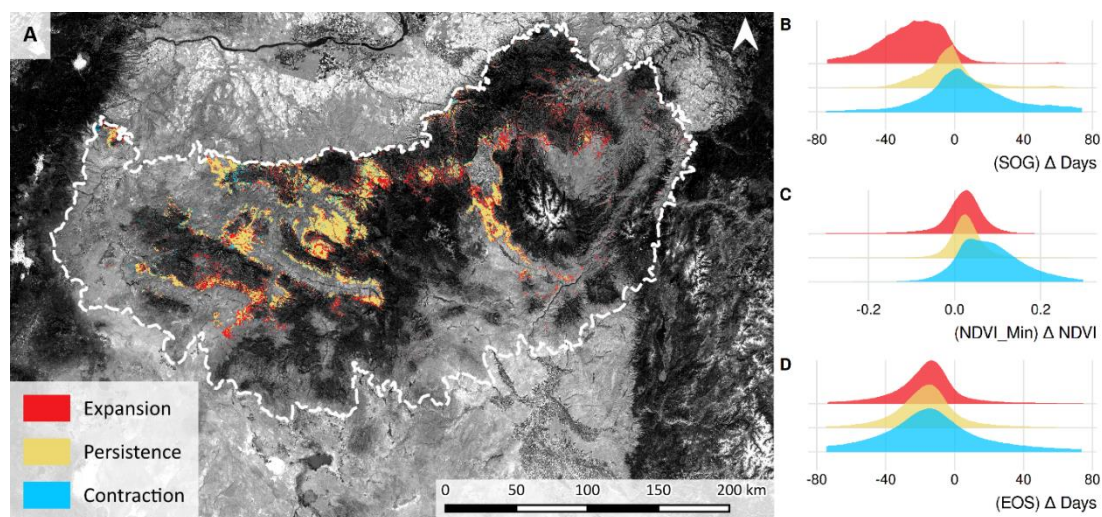


Figure 4.3. Contraction, expansion, and persistence of *ventenata* populations from 2006 to 2017 throughout the BME. In A, the categorical change in *ventenata*'s distribution is mapped across the region. In B-D, the distribution of change in phenometrics between 2006 and 2017 is shown for the start-of-greenup (B), minimum-NDVI (C), and end-of-season (D), where change is calculated as 2017 value – 2006 value. The density plots in B-D are scaled to show equal area for visibility. Positive values indicate that: vegetation greening was later in 2017 (B), minimum-NDVI was higher in 2017 (C), end-of-season was later in 2017 (D).

Despite overlap in the elevational range associated with expansion, persistence, and contraction populations, there are notable differences among the elevation ranges in which these populations are most common (Figure 4.4). The area of expansion, persistence, and contraction occupies a relatively small portion of the entire elevation gradient of the BME (Figure 4.4A). Ventenata expansion was more heavily concentrated at the higher end of the invaded elevation-range (>1,300 m; Figure 4.4B-C). The middle fifty percent of persistent populations were concentrated between 1,091 and 1,285 m (25th and 75th quantiles, respectively). Contraction populations were concentrated in a similar range as persistent populations and occurred almost proportionally to persistence across the invaded elevation range (Figure 4.4B).

Between 2006 and 2017, expansion accounted for a considerable proportion of the change in ventenata's distribution, ranging from around 0.22 to 0.95 of the invaded area across the elevation gradient (Figure 4.4C). The expansion was greatest at approximately 1,325 m and accounted for most of the change above this elevation (Figure 4.4C). Below 500 m, the proportion of expansion and contraction becomes nearly equal. However, the total area of ventenata at these lower elevations is relatively small compared to the rest of the invaded elevation range.

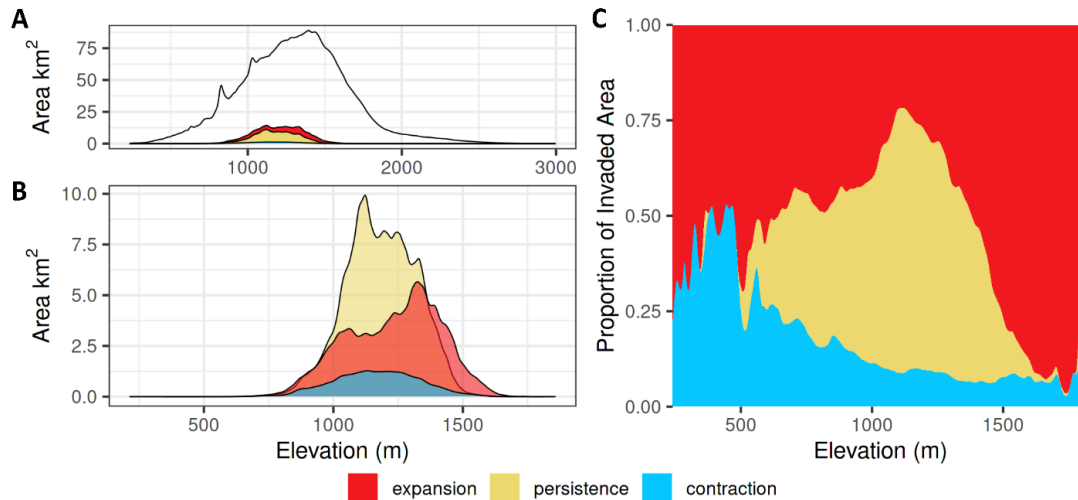


Figure 4.4. Elevation summaries by expansion, persistence, and contraction. The top left panel (A) shows the total invaded area within the context of the elevation of the Blue Mountains Ecoregion, while the bottom left panel (B) shows the area associated with each of the invasion classes across the elevation gradient. The right panel (C) shows the proportion of the invaded area for each of the invasion classes.

Between 2006 and 2017, *ventenata* expansion was associated more strongly with some PNV subzones than others (Table 4.1). In most PNV subzones, *ventenata* was either present both years or absent both years. The only exception was moist meadow, which had no *ventenata* populations in 2006 but contained *ventenata* populations by 2017. Notable PNV subzones associated with *ventenata* invasion during this period include Xeric Pine, Upland Shrub, Juniper Woodlands, Scabland Grass, and Dry Ponderosa Pine. Across PNV subzones, Xeric Pine had both the greatest proportion of its area (i.e., percent-of-subzone) classified as containing persistent (14.6% of the subzone) and expansion (9.3%) populations. In both 2016 and 2017, Upland Shrub and Juniper Woodlands were the two subzones with the greatest total area invaded. These two subzones occupy the greatest area in the BME and, also had the greatest total area invaded across time. However, they ranked lower than other PNV subzones in terms of the percent-of-subzone invaded. Although Scabland Grass did not represent a large portion of the region's area, the invaded area in this class nearly doubled over the 11 years, it had one of the highest percent-of-subzone invaded in 2017, and it exhibited the greatest median change in

relative probability between 2006 and 2017 (Figure 4.5). Dry Ponderosa Pine experienced the greatest expansion in terms of total area and a substantial increase relative to both the area invaded in 2006 and the area of persistent populations.

Table 4.1. Regional change in ventenata area for potential natural vegetation (PNV) subzones in which ventenata occupied greater than one percent of the PNV in 2017. PNV subzones are sorted in descending order by the percent

Subzone Name	PNV		VEDU 2006		VEDU 2017		VEDU Persistent		VEDU Expansion		VEDU Contraction	
	Unmasked Area (km ²)	Percent of BME	Area (km ²)	Percent of Class	Area (km ²)	Percent of Class	Area (km ²)	Percent of Class	Area (km ²)	Percent of Class	Area (km ²)	Percent of Class
Xeric Pine	4,119.29	6.42	705.14	17.12	984.26	23.89	602.02	14.61	382.25	9.28	103.12	2.50
Montane Shrub	250.59	0.39	22.19	8.86	39.21	15.65	20.32	8.11	18.89	7.54	1.87	0.75
Scabland grass	0.23	<0.01	0.02	7.57	0.03	14.74	0.02	7.17	0.02	7.57	0.00	0.40
Dry Ponderosa Pine	5,336.57	8.32	493.12	9.24	769.62	14.42	382.96	7.18	386.65	7.25	110.16	2.06
Upland grass	389.26	0.61	40.02	10.28	53.88	13.84	38.49	9.89	15.38	3.95	1.53	0.39
Riparian Shrub	426.13	0.66	34.40	8.07	57.35	13.46	31.76	7.45	25.59	6.00	2.65	0.62
Upland Shrub	8,656.85	13.50	841.20	9.72	1,150.87	13.29	814.02	9.40	336.85	3.89	27.18	0.31
Juniper Steppe	3,121.59	4.87	271.86	8.71	363.26	11.64	254.79	8.16	108.47	3.47	17.07	0.55
Scabland Shrub	1,582.30	2.47	125.13	7.91	174.30	11.02	122.38	7.73	51.93	3.28	2.75	0.17
Juniper Woodlands	10,133.99	15.81	782.44	7.72	1,043.41	10.30	695.57	6.86	347.83	3.43	86.87	0.86
Ponderosa Pine-Lodgepole	69.80	0.11	2.70	3.87	5.95	8.53	2.07	2.96	3.89	5.57	0.63	0.91
Moist Ponderosa Pine	46.16	0.07	2.24	4.84	3.45	7.48	1.23	2.66	2.22	4.81	1.01	2.18
Moist Meadow	0.67	<0.01	0.00	0.00	0.05	6.88	0.00	0.00	0.05	6.88	0.00	0.00
Dry Douglas-Fir	7,578.38	11.82	288.74	3.81	463.62	6.12	156.40	2.06	307.22	4.05	132.33	1.75
Developed	3,054.65	4.76	101.57	3.33	170.71	5.59	76.60	2.51	94.11	3.08	24.97	0.82
Dry Lodgepole Pine	33.30	0.05	0.08	0.25	0.87	2.60	0.02	0.06	0.85	2.54	0.06	0.19
Ponderosa Pine-White Oak	18.64	0.03	0.92	4.92	0.48	2.55	0.19	1.04	0.28	1.51	0.72	3.88
Riparian Hardwood Forest	66.82	0.10	0.24	0.36	0.90	1.34	0.17	0.25	0.73	1.09	0.07	0.11
Dry White Fir - Grand Fir	5,464.50	8.52	27.99	0.51	58.32	1.07	14.68	0.27	43.64	0.80	13.31	0.24

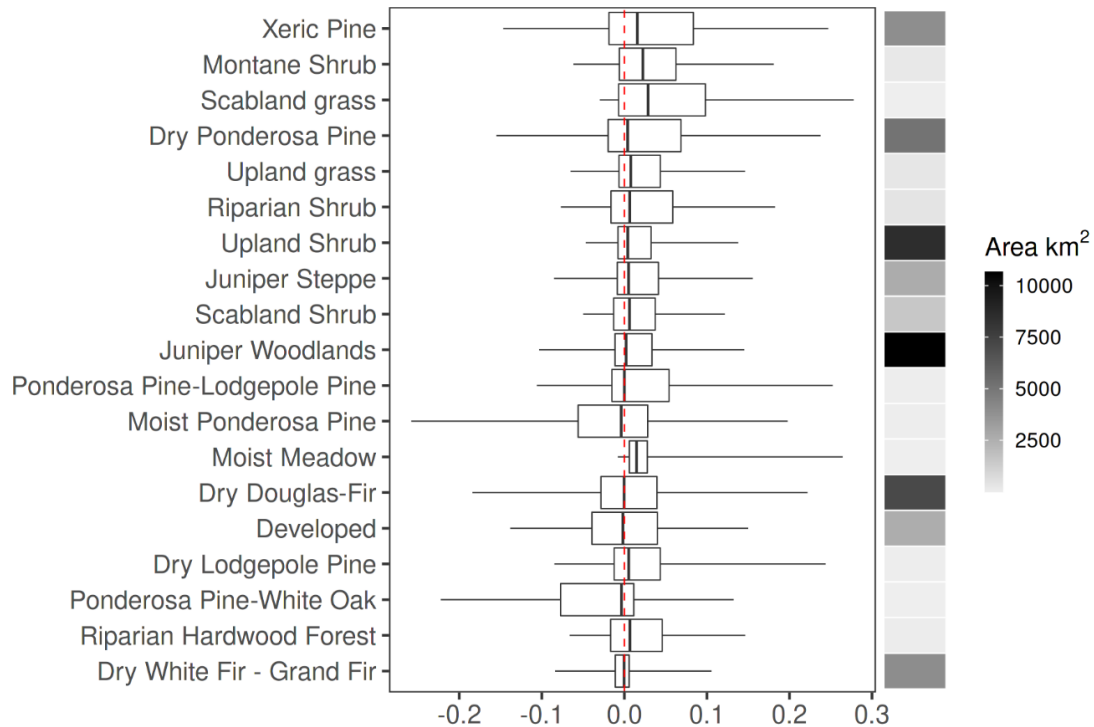


Figure 4.5. Summary of the difference in probability between 2017 and 2006 for the potential natural vegetation (PNV) subzones presented in Table 4.1. Boxplot summaries of the probability differences include the median (middle line segment), the 25th and 75th percentile (the upper and lower hinges), and the 5th and 95th percentile (the whiskers). The heatmap on the right shows the total area per PNV subzone within the study area of the BME.

4.4.1.2 Wildfire

Across both wildfire and non-wildfire areas, the probability of ventenata generally increased between 2006 and 2017. Some wildfires in the dry-forest fire-veg group saw greater than a 50% increase in probability on average (i.e., mean percent-change in probability greater than 50%; Figure 4.6). There were notable differences in ventenata predictions between wildfire and non-wildfire areas for three fire-veg groups: mixed/woodland, dry-forest, and mixed-conifer (Figure 4.6). Wildfires in dry-forest had the largest increase in the mean percent-change in probability (median of 28%) and the greatest variability (IQR of 43%) and the least overlap with the mean percent-change in probability from non-wildfire areas. In the mixed/woodland group, wildfires had a median increase of 23% (IQR of 25%), while

non-wildfire areas had a median increase of 5% (IQR of 13%). Mixed-conifer wildfires had a median increase of 14% (IQR of 22%) and non-wildfire areas had a median increase of only 1% (IQR of 8%).

In shrubland and woodland, which had the most large wildfires of the fire-veg groups between 2006 and 2017 (Table 4.2), the mean percent-change in probability was minimal for both wildfires and non-wildfire areas. The mean percent-change was also low in non-wildfire wildfires and regions of the subalpine group, which was the only fire-veg group where the mean percent-change in probability decreased in the absence of fire.

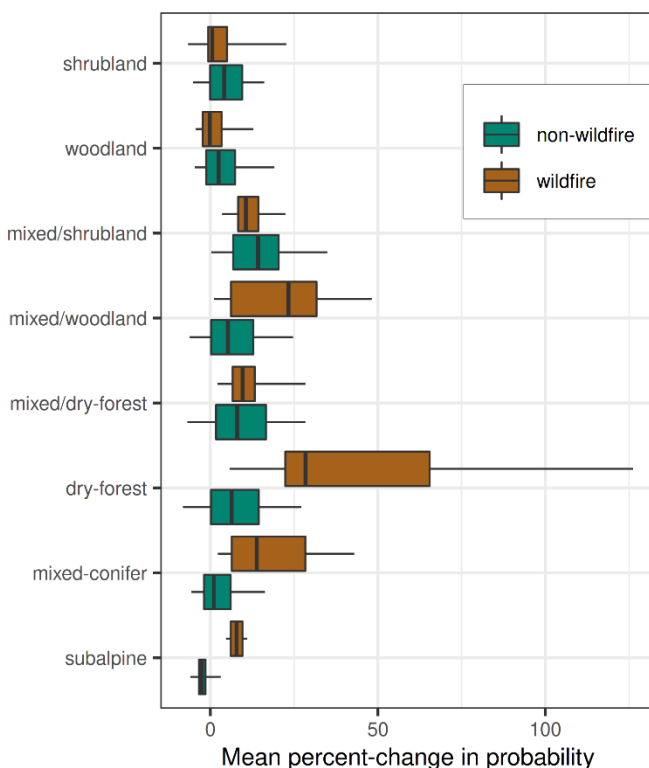


Figure 4.6. Summaries by fire-veg group for the mean percent-change in the probability of ventenata within wildfires and non-wildfire areas. Boxplot summaries include the median (middle line segment), the 25th and 75th percentile (the upper and lower hinges), and the 5th and 95th percentile (the whiskers).

Table 4.2. Number of wildfires, median fire size by fire-veg group, and number of non-wildfire samples.

Fire-veg group	Number of wildfires	Median fire size (ha)	Number of non-wildfire Samples
shrubland	42	1,686	706
woodland	31	1,596	1,058
mixed/shrubland	4	6,892	254
mixed/woodland	8	8,022	351
mixed/dry-forest	12	15,424	837
dry-forest	5	1,534	922
mixed-conifer	15	2,727	1,492
subalpine	2	1,621	83

The relationship between median burn severity (RdNBR) and change-class of ventenata predictions (percent-change in probability of ventenata) varied by fire-veg group, as did the variability (IQR) in burn severity (Figure 4.7). There was no clear relationship between burn severity and increase or decrease in ventenata predictions for wildfires in the subalpine group. Although shrubland and woodland did not have a strong increasing or decreasing trend in burn severity as change-class increased, there was generally an increase in the variability of median RdNBR with increasing change-class in shrubland. Apart from these three fire-veg groups, all other groups suggested a positive relationship between burn severity and change in the probability of ventenata. In the mixed/woodland group, there was a general rise in the median and IQR of RdNBR with increasing change-class. For mixed/woodland and mixed/dry-forest, the increasing median RdNBR was more exponential than linear as change-class increased.

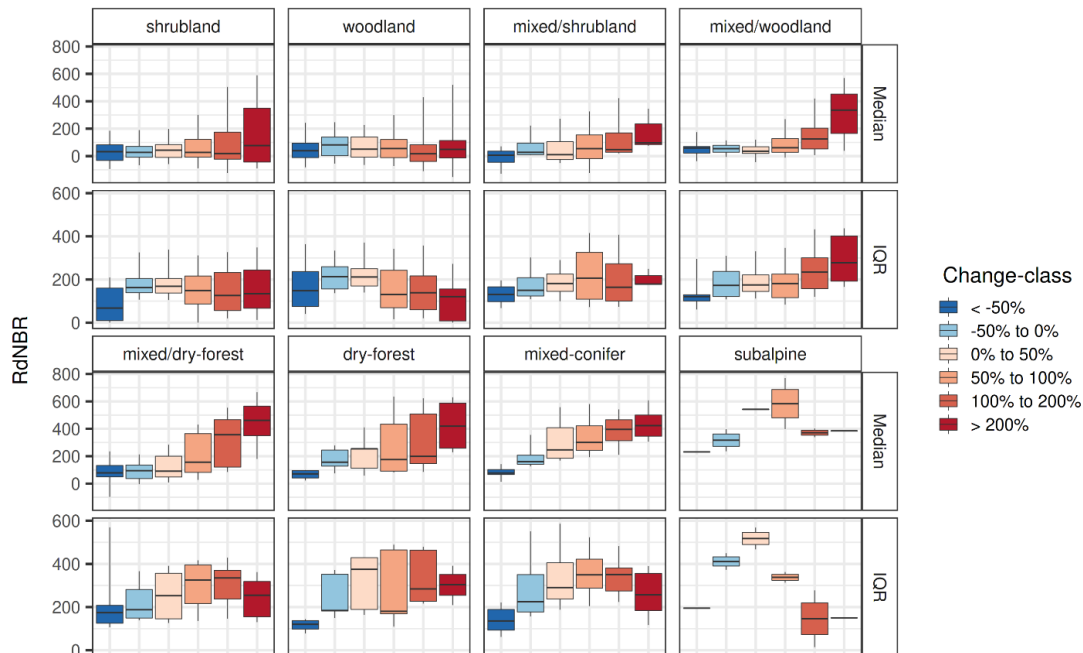


Figure 4.7. Summary of the median and IQR of burn severity (RdNBR) within wildfires by change-class (percent-change in probability of ventenata) and fire-veg group. For example, in the mixed/woodland group and median statistic, boxplots summaries for the > 200% change-class are based on the median of RdNBR in the > 200% change-class for each wildfire in that fire-veg group. Boxplot summaries include the median (middle line segment), the 25th and 75th percentile (the upper and lower hinges), and the 5th and 95th percentile (the whiskers).

When burn severity within a wildfire was compared across change-classes, all fire-veg groups tended to show that an increase in ventenata change-class was associated with increased burn severity (Figure 4.8, all mean-differences of median RdNBR positive). The one exception was the subalpine group, which had a small number of fires (Table 4.2) and no discernible trend (Figure 4.8). For most fire-veg groups, the magnitude of the difference in burn severity (median RdNBR) was also associated with an increase in change-class (e.g., mixed/dry-forest in Figure 4.8, warmer tones moving left-to-right and top-to-bottom). The average difference in the IQR of RdNBR generally followed a similar pattern, again with the exception of the subalpine group.

Similar to results in Figure 4.7, the largest differences in severity between change-classes were in wildfires that occurred in the mixed ecotones and in forested areas dominated by dry-forest or mixed-conifer (Figure 4.8). On average, in the mixed/dry-forest, mixed/woodland, and shrubland, the difference in median RdNBR between any pair of change-classes was greatest when compared with the highest change-class, which represents areas where there the probability of ventenata more than doubled between 2006 and 2017 (Figure 4.8, warmest tones found in the right-most column). For the average wildfire in mixed-conifer or mixed/shrubland, comparisons of median RdNBR were the greatest magnitude when change-classes were compared with the lowest change-class (i.e., locations where the probability of ventenata in 2017 decreased by 50% from 2006; Figure 4.8, warmest tones found along the bottom row).

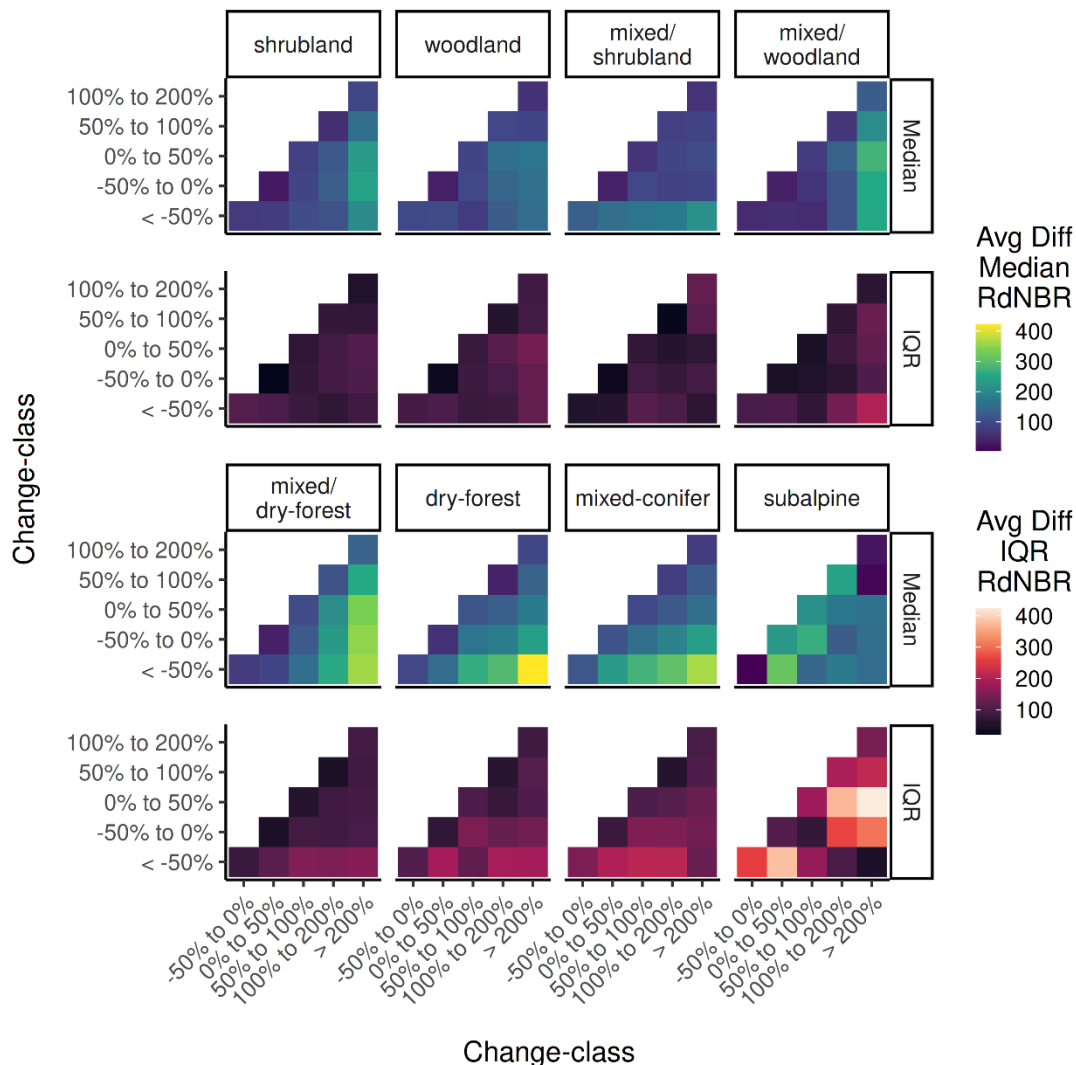


Figure 4.8. Heatmap of the average (mean) difference in the median and IQR of burn severity (RdNBR) between change-classes (percent-change in probability of ventenata) within wildfires for each fire-veg group. For example, in the dry-forest group and median statistic, the right-most column of the heatmap shows the average difference in the median RdNBR between the > 200% change-class and progressively smaller change-classes (i.e., lower percent-change in probability) moving down the column, where the greatest average difference in median burn severity is between the >200% and the < -50% change-classes (differences in this cell are calculated at the wildfire-level first, before the average taken at the fire-veg level).

4.4.2 Case Studies

4.4.2.1 Starkey Experimental Forest and Range

In 2006, Starkey Experimental Forest and Range (SEFR) had a total of 718 ha of ventenata (7% of the SEFR) that increased to nearly 2,086 ha (20%) by 2017. During this time period, the mean patch-size increased from 1.4 ha to 2.3 ha and the total number of patches increased from 512 to 918. By 2017, the average minimum-distance between patches had decreased from 129 m to 87 m. Additionally, patches became more elongated in 2017 (average RMOBB of 0.86 in 2006 vs. 0.77 in 2017).

Many forest openings within SEFR had a large percentage-increase in ventenata probability between 2006 and 2017 (i.e., positive percent-change in probability; Figure 4.9). However, because some of the larger relative-increases occurred in locations where the probability of ventenata was very low probability in 2006, only some of these areas were classified as ventenata expansion (Figure 4.10; e.g., lower-right corner of Figure 4.9D vs. Figure 4.10B). Decreased probability of ventenata was generally associated with forested areas, especially along the edges of forests and meadows (Figure 4.9D), where it was associated with an increase in the minimum-NDVI (Figure 4.9C). This increase in minimum-NDVI was confirmed by tree ingrowth evident in NAIP imagery in these areas (Figure 4.9A-B).

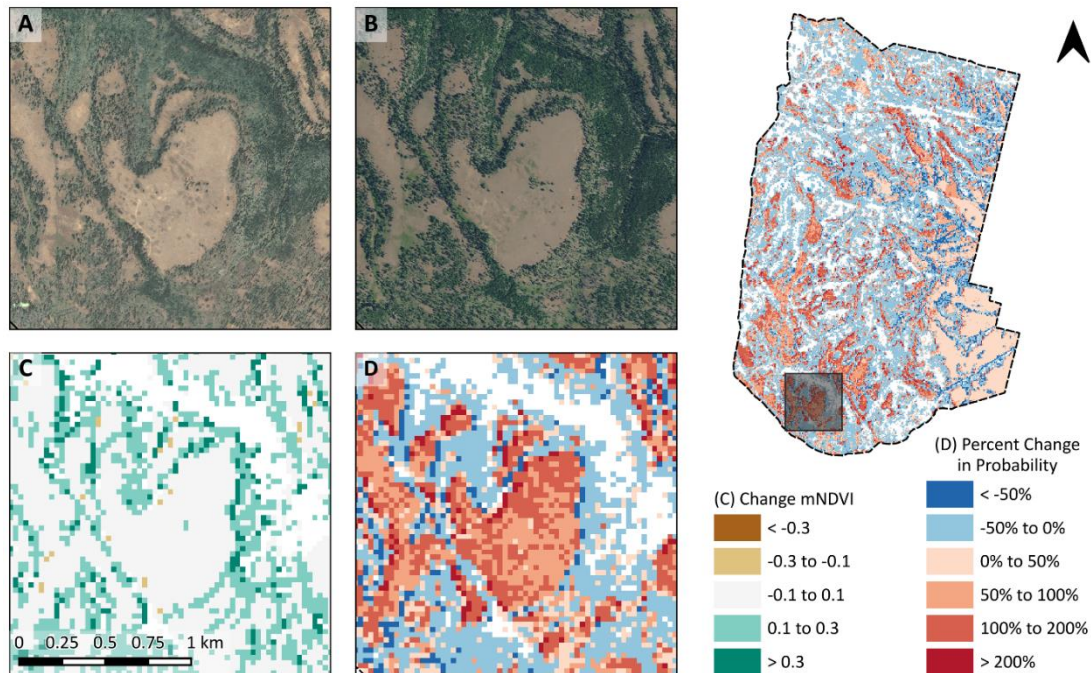


Figure 4.9. Change in vegetation (A-B), minimum-NDVI (C), and ventenata predictions (D; percent-change in ventenata probability) across the Starkey Experimental Forest and Range (SEFR) from 2006 to 2017. The percent-change in probability of ventenata is shown for all of SEFR in the right panel, with a dark-grey square corresponding to the location of the zoomed-in panels A-D. Change in vegetation for the nearest dates to 2006 and 2017 are shown as NAIP imagery from 2005 (A) and 2016 (B).

Locations with persistent ventenata populations on the eastern side of SEFR showed little to no increase in probability (Figure 4.9). In contrast, several nearby-areas showed relatively large decreases in probability, many of which were associated with contraction (Figure 4.10). Persistent ventenata populations were primarily located in the large forest openings found on the eastern side of the region (Figure 4.10). The elongation of persistent patches (RMOBB = 0.85) tended to be much less than that of expansion patches (RMOBB = 0.77). Persistent patches totaled 323 with a mean patch-size of 1.9 ha. Ventenata expanded into many of the openings throughout SEFR, but there was less expansion in the northwestern corner of SEFR. Expansion patches totaled 1,197 with a mean patch-size of 1.2 ha. In contrast, the contraction of ventenata generally occurred along the border of forest openings and in closer proximity to persistent populations (average minimum-

distance of 115 m) than expansion (389 m). In total, there were 563 contraction patches and the mean patch-size was 0.2 ha.

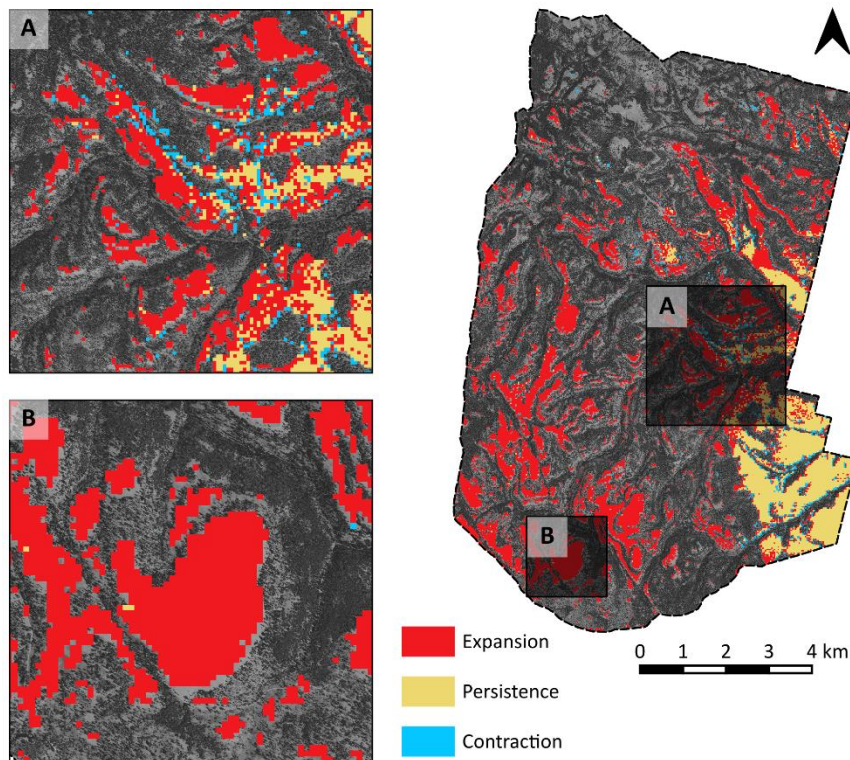


Figure 4.10. Change in *ventenata*'s distribution across the Starkey Experimental Forest and Range (right panel) between 2006 and 2017, illustrated by contraction, expansion, and persistence of *ventenata* populations. In the right panel, the location of panels A-B are indicated by the dark-grey squares. The example in panel A illustrates how contraction generally occurred along the border of forest openings close to persistent patches. The location of panel B is the same as Figure 4.9, panels A-D. In the background of all images is a grey-toned NAIP image from 2016 showing the configuration of forested and non-forested areas within the SEFR.

4.4.2.2 Canyon Creek Complex

The large wildfire known as the Canyon Creek Complex (CCC) was included in the dry-forest fire-veg group. Burn severity was highly variable within the burned areas, with RdNBR ranging from -360 to 1,100 (median = 225; Figure 4.11B). Many of the areas that experienced higher severity (>700 RdNBR) were associated with a large relative increase in probability of *ventenata* between 2006 and 2017 (i.e., >100 percent-change in probability). However, not all areas with high severity showed a

large increase in probability. This region is notable when compared to the rest of the BME because many locations within this wildfire's burn perimeter had a substantial percentage increase in probability (i.e., percent-change in probability): a total of 289 ha (0.7%) within the burn perimeter had greater than 400% increase in probability between 2006 and 2017.

In 2006, 9 years before the wildfire, the area had a total of 1,799 ha of ventenata (4% of the area). Two years after the wildfire, this increased to 5,667 ha (13% of the area in 2017). The mean patch-size increased from 1.1 ha in 2006 to 4 ha in 2017, while the total number of patches decreased from 1,583 to 1,421. The average minimum-distance between patches of ventenata also reduced from 105 m to 97 m in 2017. The average shape of patches was similar between periods, with an average RMOBB of 0.86 in 2006 and 0.82 in 2017.

The largest persistent ventenata population within the CCC was in the northeastern corner of the burn perimeter. Although, several persistent populations were also located within the canyon running north to south along the western side of the burn perimeter (Figure 4.11, C). There were 1,238 persistent patches with a mean patch-size of 1.3 ha. In terms of average patch-shape, persistent patches (RMOBB = 0.86) were not substantially different from expansion (RMOBB = 0.82) or contraction (RMOBB = 0.88) patches. Compared to SEFR, expansion of ventenata within the CCC was more radial than saltatorial. There were 1,676 expansion patches (mean patch-size of 2.4 ha), with expansion primarily concentrated along the northern and western sides of the burned area. Contraction patches totaled 816 with a mean patch-size of 0.2 ha. Ventenata contraction primarily occurred along the Canyon Creek, which runs north to south on the west side of the burn, with patches of contraction generally closer to persistent populations (average minimum-distance of 143 m) than expansion patches (414 m).

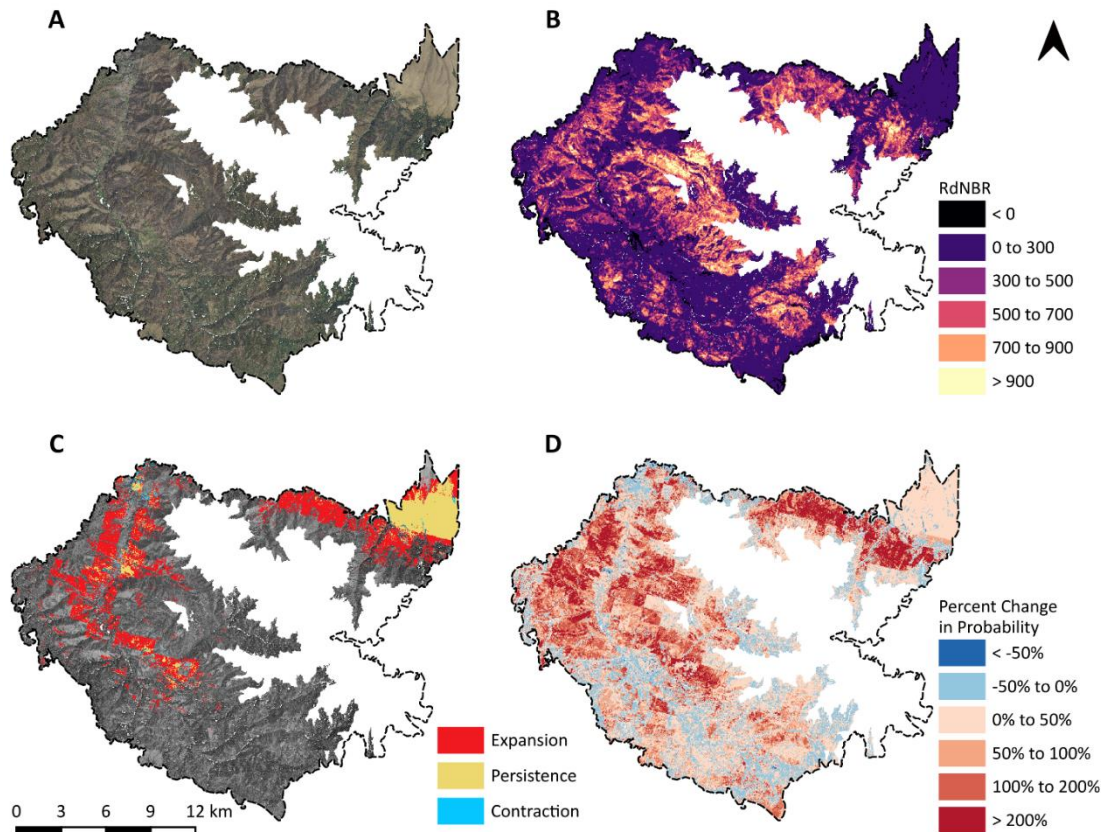


Figure 4.11. The Corner Creek Complex wildfire's burn perimeter, including NAIP imagery from 2016 (A), burn severity (B; RdNBR), and the change in *ventenata*'s distribution between 2006 and 2017 (C-D). Panel C shows *ventenata* expansion, contraction, and persistence, while panel D shows percent-change in *ventenata* probability (percent-change in probability between 2006 and 2017). White-area within the burn perimeter indicates locations masked from the analysis because the elevation was above 1,829 m.

4.5 Discussion

Between 2006 and 2017, *ventenata* spread widely throughout the Blue Mountains Ecoregion (BME). Although this invasion only occupies a relatively small proportion of the region, our estimates indicate that the total area of *ventenata* with cover greater than 20% increased by 44% in little more than a decade (378,000 ha to 545,000 ha); an average yearly increase of 15,200 ha/yr. *Ventenata* has been documented in a variety of plant communities of the BME (Wallace et al., 2015). Still, some parts of this region have only just recently observed *ventenata* for the

first time (Nicolli et al., 2020). Considering the progression of invasion and breadth of ecosystems suitable for invasion in the BME, this region appears to be at high risk for future potential impacts of *ventenata*.

The spread of invasive species is driven by a hierarchy of processes occurring at multiple scales of time and space (Pyšek and Hulme, 2005). Seed rain and local dispersal (e.g., wind or water transport) in combination with microsite characteristics drives the local diffusion of populations into areas surrounding a population, while long-distance dispersal (e.g., ungulate or vehicle transport) to new locations drives the establishment of new populations. Over time, these processes result in the region-level patterns of invasion. On average, much of the *ventenata* invasion spread radially from patches present in 2006 (decreasing number of patches and increasing mean patch-size), and this regional trend also occurred within the bounds of the Canyon Creek Complex (CCC). This higher frequency of radial expansion over saltatorial expansion (i.e., leaping or discontinuous spread) runs counter to the bias Pyšek and Hulme (2005) proposed would occur when using distribution maps to estimate spread.

Nevertheless, there were also many cases of saltatorial expansion in the BME, especially within forest openings, as demonstrated in the Starkey Experimental Forest and Range (SEFR). This resulted in the SEFR having a different patch-size trend (increasing number of patches and increasing patch size) compared to the entire BME and a different patch shape (lower RMOBB) than the CCC. Within the SEFR, radial expansion primarily occurred within large, lower elevation open areas to the east, while saltatorial expansion was common throughout the area, owing to the highly fragmented forest/non-forest patch configuration.

4.5.1 Phenology and Biophysical Setting

Within rangelands of the BME, *ventenata* seedling emergence starts in the late fall (October) and will typically continue through spring (March), with the exact

timing of this process being governed by the timing and amount of precipitation (Wallace et al., 2015). As with other invasive annual species, the germination strategy of *ventenata* likely provides a competitive advantage over native species, which tend to germinate and grow later in the year (Hardegree et al., 2010; Harris and Wilson, 1970; Thill et al., 1979; Wilson et al., 1974). We found the *ventenata* expansion and the increased probability between 2006 and 2017 were often associated with earlier start-of-greenup (median of 24 days earlier in 2017; Figure 4.3). Given that we controlled for the climatic influence on phenology, the earlier start-of-greenup may indicate *ventenata* populations increased within these areas. *Ventenata* expansion and probability increase was frequently observed in forest openings, within some wildfires, and along major ecotones between forested and non-forested. Although the probability of *ventenata* generally increased region-wide, some areas had decreases in probability that led to a contraction of some populations (Figure 4.3; Appendix H). This process was demonstrated in the SEFR, where *ventenata* contraction and decreasing probability of *ventenata* were commonly associated with forested areas and increasing minimum NDVI and canopy cover (Figure 4.9).

A wide range of plant communities and elevations have been previously reported as being at high risk of *ventenata* invasion (Jones et al., 2018; Nicolli et al., 2020; Tortorelli et al., 2020). We found that 50% of persistent populations were located between 1,091 and 1,285 m (IQR), an elevation range that overlaps many areas dominated by sagebrush steppe and juniper woodlands within the BME. Accordingly, we found that the PNV subzones with the greatest area of persistent populations were split between Upland Shrub (814 km²) and Juniper Woodland (696 km²). However, more than 40% of *ventenata* expansion within the BME occurred above 1,300 m. At elevations greater than 1,300 m, the prevalence of dry conifer forest and transition zones (e.g., the Xeric Pine subzone) between dry forest, woodlands, and shrublands increases within the BME. PNV subzones with the

greatest expansion included Dry Ponderosa Pine (387 km²) and Xeric Pine (382 km²).

Our findings suggest that *ventenata* may have initially established sustaining populations within the BME in mid-elevation sagebrush-steppe communities and has since largely spread to higher elevations, connecting the ecotonal-transition between shrubland ecosystems and dry conifer-dominated ecosystems at higher elevation. These findings were corroborated by a recent study reporting heavy *ventenata*-invasion in the 1,250 to 1,665 m elevation range of the BME (Tortorelli et al., 2020). Together, these observations contrast with the observed pattern of cheatgrass invasion in the Great Basin, where cheatgrass was initially introduced at a relatively high elevation and expanded to lower elevations (Bradley and Mustard, 2006). Additionally, areas of the BME with shallow soils, such as parts of the Xeric Pine and Scabland Grass subzones, have recently experienced substantial invasion (Table 4.1). Compared to areas with deeper soils, areas with shallower, less productive soils have been considered ‘invasion resistant’ to other invasive grasses present throughout this part of the Pacific Northwest (Johnson and Swanson 2005). *Ventenata*’s presence in these locations may be pushing resistance boundary of these less productive sites.

4.5.2 Wildfire

Fire occurrence is known to promote many invasive grasses (Brooks 2008). We found evidence that wildfire occurrence and severity was related to an increased probability of *ventenata* in many vegetation types throughout the BME. Wildfires that alter plant-community structure or the physical environment in a way that promotes *ventenata*, may increase the connectivity of *ventenata* populations, thereby increasing fine fuel connectivity across the landscape. A grass-fire-cycle could develop if connectivity of fine fuels promotes future fires.

The grass-fire-cycle is well documented for cheatgrass (Brooks et al., 2004; D'Antonio and Vitousek, 1992). However, cheatgrass has historically not been as problematic in some plant communities in which *ventenata* has recently become abundant. *Ventenata*'s trend of invading forested and ecotonal areas may become especially problematic if the *ventenata* invasion increases fuel connectivity between forest stands. Regional approaches to assessing fire behavior, as it relates to grass invasion, have reported the influence of cheatgrass and other invasive annual grass species on fire frequency, size, and ignitions (Balch et al., 2013; Bradley et al., 2017; Fusco et al., 2019). However, these large-scale analyses have only looked at one side of the grass-fire cycle and have not examined the influence of wildfires on grass invasion.

We found that the probability of *ventenata* generally increased between 2006 and 2017, both in areas with and without wildfire, in all but the non-wildfire subalpine fire-veg group. However, some fire-veg groups that burned during the study period had a higher percent increase in the probability of *ventenata* than non-wildfire areas (Figure 4.6). This association was observed for wildfires in areas dominated by woodlands with a high mixture of forest and nonforest (mixed/woodland) and forested areas dominated by dry-forest or mixed-conifer. In these three settings, *ventenata* probability may have increased because nearby populations of *ventenata* in open areas were provided with the opportunity to spread to previously unsuitable areas (e.g., high canopy cover). The only other study to examine the relationship between fire and *ventenata* in forested areas is Tortorelli et al. (2020). They found evidence that wildfire in mixed forest and shrubland may have influenced the relationship between *ventenata* cover and plant species richness (Tortorelli et al., 2020). While grass invasion is typically thought to be less problematic in forests, there is some evidence that positive invasion-fire feedbacks can develop in forest ecosystems (Wagner and Fraterrigo, 2015).

In contrast with forested areas, the shrubland and woodland fire-veg groups had relatively small increases in probability and were similar in both areas with wildfire and those without. Ridder et al. (2021) examined the relationship between ventenata and historical fire occurrence in a grassland of the BME (shrubland or mixed/shrubland fire-veg group). They reported that although ventenata generally increased during their study period, there was no substantial impact of fire occurrence on ventenata's invasion. Our results corroborate this observation in non-forested parts of the region. Likewise, similar results have been reported for cheatgrass growing in the grasslands on the western edge of the Great Plains, suggesting that some grasslands are less susceptible to developing a positive feedback between invasive annual grasses and fire (Porensky and Blumenthal, 2016).

In all fire-veg groups except for subalpine, we found that areas with a higher change-class (percent-change in probability) for ventenata also had higher burn severity (Figure 4.7). Although, the strength of this relationship varied by fire-veg group. Between neighboring change-classes (e.g., an increase of 50-100% vs. 100-200%), differences in burn severity were greatest for wildfires in mixed/woodlands, mixed/dry-forest, dry-forest, and mixed-conifer (Figure 4.8). Of these four fire-veg groups, the mixed/dry-forest was the only group with no association between wildfire occurrence and ventenata probability. This may suggest that ventenata is invading these areas regardless of wildfire occurrence, but when wildfire does occur, areas with a greater percent-increase in ventenata tend to have burnt at higher severity (Figure 4.8).

The potential for fire to connect and expand patches of ventenata in this region was recently proposed (Kerns et al., 2020) and the patterns observed in the CCC provide some support for this idea. We found that burn severity within the CCC wildfire likely influenced ventenata invasion. Spatial patterns of increased probability corresponded in many instances to the spatial patterns of high burn-

severity (Figure 4.11). However, within the wildfire's perimeter, there are many areas that burned at high severity and were not invaded by *ventenata* post-fire, indicating that these areas may have experienced a reduction in canopy but had not yet been invaded. This suggests that, while wildfire does not always lead to *ventenata* invasion, *ventenata* can establish if the niche space is suitable and wildfire sufficiently reduces canopy cover. Additionally, in comparison with SEFR (which did not burn), expansion in the CCC tended to be more radial, where the mean patch-size increased, and the number of patches decreased between 2006 and two years post fire (2017). These changes in patch metrics may relate to the consumption of canopy cover in high-intensity burn areas, thereby connecting and expanding previously established *ventenata* populations.

To date, no other studies have investigated the relationship between burn severity and *ventenata*. While our findings represent an important first look at the fire relationship across vegetation types, the need exists for further research in this direction. Our study has the advantage of incorporating all large wildfires between 2006 and 2017, covering various plant communities and vegetation spatial configurations. In looking to the future, it was recently reported that increased temperatures and atmospheric carbon dioxide concentrations may provide an advantage to *ventenata* over cheatgrass under climate change conditions (Harvey et al., 2020). Along with the potential for forest treatments to introduce exotic species (Abella and Springer, 2015; Keeley, 2006) and the promotion of *ventenata* by fire, the future of forests in this region may be negatively impacted by *ventenata* invasion.

4.5.3 Caveats and Considerations

The analysis of remote-sensing derived maps of species presence can be impacted by the accuracy of the model from which they were produced (Langford et al., 2006; Liu et al., 2007). In this study we attempted to control for climatic impacts on phenology by selecting years with similar local weather patterns, but given the

variability of weather across the ecoregion, we cannot completely control for the influence of weather on phenology. Classification error from weather variation and other sources will inevitably have an impact on the spatial patterns observed in model predictions. There are invasive annual grasses present within the BME that may have similar phenology to *ventenata*. Therefore, there may be locations the model predicted as *ventenata* that also contain other annual grasses. However, misclassification in this context was likely reduced by the inclusion of other climate and biophysical data in the model that assisted in differentiating the environmental niches of these species.

Future studies would benefit by considering additional factors related to wildfire. Given the complex processes happening on the ground, we cannot conclude with certainty that changes in the probability of *ventenata* are directly related to wildfire occurrence or severity. Firstly, because we only examined large wildfires (i.e., > 405 ha), we cannot guarantee that 'non-wildfire' areas did not burn during this period. Not accounting for smaller wildfires or prescribed fire could be confounding some of the results we observed between 'wildfire' and 'non-wildfire' areas for these fire-veg groups. Secondly, there are known accuracy issues related to using RdNBR to characterize the severity of fires (Miller et al., 2009). Additionally, we did not explicitly review the relationship between time since fire and the difference in *ventenata* probability or occurrence. For example, the Canyon Creek Complex occurred within 2 years of 2017. The abundance or prevalence of *ventenata* will likely change across the landscape as the forest within this wildfire's burn perimeter regenerates (Flory et al., 2017). This study intended to provide a first look at the region-wide relationship between fire and *ventenata*. Therefore, additional research on fire and *ventenata* is warranted.

4.6 Conclusion

Our findings represent the first region-level assessment of the invasion progression of *Ventenata dubia*. To our knowledge, this is also the first examination

of the response of an invasive annual grass to large wildfires at a regional scale. We utilized land surface phenology in conjunction with climatic predictors to examine change in the spatial distribution of *ventenata* across a 7 million ha region of the interior Pacific Northwest. We controlled for climatic impacts on this species' phenology to minimize error related to weather's influence on vegetation development. Our findings indicate that *ventenata* has expanded from lower elevation shrublands into the ecotone between shrublands, woodlands, and open pine forests of the Blue Mountains Ecoregion. This invasion of higher elevations within the region may be catalyzed by the occurrence or severity of large wildfires that have occurred in the 11-year period between our observations, but the impact of wildfire on the invasion seems to differ by the proportion of ecotone within the burn perimeter in addition to the dominant vegetation type. While this study is limited in extent to the Blue Mountains Ecoregion, it is not unreasonable to infer other dry interior forests may also be at risk of *ventenata* invasion, which could be catalyzed by fire. Given the potential negative impacts of grass-fire-cycles, the results of this study provide supporting evidence to focus future research and management on *ventenata* within the Blue Mountains and more broadly within the continental, western United States.

5 CONCLUSION

Ecosystems across the planet have experienced changes resulting from the behaviors of humans. In conjunction with climate change and land use and land cover change, the transport and invasion of nonnative species has resulted in substantial impacts to the world's ecosystems (Pyšek and Richardson, 2010). Therefore, it is critical to track and quantify the status and impacts of nonnative species introductions (Latombe et al., 2017). This dissertation sought to develop and apply tools to track the present and past distribution of an invasive annual grass, providing insight into the relationships and potential drivers of this invasion. First, this research focused on developing tools to estimate the temporal patterns of vegetation development that can be used to detect species with unique phenology. I then tested whether these estimates in conjunction with abiotic environmental characteristics could adequately estimate the present distribution of an invasive annual grass species. Finally, I expanded the analysis temporally to encompass two time periods to examine the progression of the invasion in the context of the biophysical relationships and the occurrence and severity of large wildfires.

In Chapter 2, I addressed two challenges related to the detection and mapping of an invasive annual grass. I focused on quantifying vegetation phenology at ecologically meaningful spatial and temporal scales by 1) implementing a spatio-temporal image fusion algorithm in Google Earth Engine (GEE) and 2) using the resulting time series to estimate intraannual phenological patterns. I found that employing spatio-temporal image fusion on a cloud-computing platform like GEE is feasible and can produce high-quality predictions in reasonable timeframes. The algorithm implemented on GEE resulted in accurate predictions of similar quality to those produced by an older, locally run algorithm. I showed that land surface phenology estimates derived from this time series corresponded with plant development patterns in shrubland, grassland, and open-pine land-cover types. This work also indicated that our land surface phenology estimates aligned with the

phenological patterns of dominant functional groups at some field sites. However, I found that phenometrics from the satellite data did not correspond well with phenometrics from near-surface sensors commonly used to evaluate satellite-based phenology.

The data produced from this research may help those studying rapidly changing ecosystems (Gunderson, 2000). I found that these data were instrumental in identifying annual grass species because shifts in plant community composition appear to lead to differences in the annual phenological pattern. Phenological patterns have been employed to identify and map populations of other invasive annual grasses in the western United States, however, data used in these studies were limited in spatial resolution (Boyte and Wylie, 2016; Bradley et al., 2017). Additionally, annual grass species strongly respond to year-to-year climatic variation (Pilliod et al., 2017) and represent a substantial proportion of surface canopy cover in some shrubland, grassland, and open pine communities (D'Antonio and Vitousek 1992). Thus, in temporally dynamic situations, intraannual LSP estimates may be useful. The added benefit of using two satellite data sources to quantify the land surface phenology could possibly help in the study of climate change induced changes to phenology.

Estimating intraannual phenology in semi-arid regions at 30 m resolution with image-fusion-derived time series presents many challenges and opportunities. While the development of cloud computing infrastructure has improved access and processing power for some image processing tasks, spatial operations are not ideal for platforms designed to divide datasets into smaller units for parallel computation. Other recent advances in developing spatio-temporal image fusion algorithms in GEE (Moreno-Martínez et al., 2020) promise to continue advancing processing techniques to avoid limitations of the GEE platform. Additionally, the integration of deep learning libraries like TensorFlow (Abadi et al., 2015) with GEE also offers new possibilities for further innovation in image fusion methods, potentially building

upon current deep learning methods for image fusion (Song et al., 2018), while taking advantage of the cloud computing infrastructure of GEE. My phenology estimates were limited within areas of high conifer cover and when cloud cover prevented surface observation at critical times. Incorporating data from recently launched satellites and continued efforts to improve image fusion on cloud-computing platforms may help overcome some of these limitations.

In Chapter 3, I investigated the use of 30 m land surface phenology and environmental variables for modeling and mapping the distribution of ventenata (*Ventenata dubia*) in the Blue Mountains Ecoregion (BME) of the interior Pacific Northwest. The methods employed in this research support the idea that including remote sensing attributes directly related to a species presence will represent the present distribution of that species (Bradley et al., 2012). Previous estimates of other invasive annual grasses in the western US have focused on using lower resolution land surface phenology, restricting the utility and application of these maps. Spatial information of species presence and abundance is critical for managing invasive species (Cheney et al., 2018; Funk et al., 2020). I found that the invasion of ventenata in relatively small forest openings was picked up with my model that included phenology and environmental predictors. Model comparisons also showed that ventenata does not appear to be distinguishable based on phenology alone. By adding environmental information I was able to use the species niche to distinguish ventenata from other species with similar phenology. Based on these estimates, ventenata may already have robust populations in 7.7 percent (5,454 km²) of the BME. I also found that substantial portions of the region contain suitable conditions for the future establishment of ventenata. Knowledge of the present distribution and suitable habitat of ventenata may help create a more realistic prediction of future risk within this and neighboring regions.

These models of ventenata's distribution require a nuanced interpretation. I had to use phenology and bioclimatic predictors to achieve the best discrimination

of *ventenata* within the BME. Using the data sources in combination has its issues. First, some of the spatial patterns predicted by the model are likely related to the spatial grain mismatch between the phenology (30 m) and climate (800 m) datasets. Second, the mixed pixel effect (Chen et al., 2018) on *ventenata* detection has not been evaluated. The influence of *ventenata* on the phenology when growing in a highly mixed vegetation composition could be disproportionate in the early season because of other species dormancy. Conversely, the senescence of *ventenata* may be captured because other vegetation may still be active when *ventenata* ends its life cycle.

Chapter 4 provided insight into the temporal patterns of the *ventenata* invasion in the BME. The results of this study represent the first region-level assessment of the invasion progression of *ventenata*. To my knowledge, this is also the first examination of the response of an invasive annual grass to large wildfires at a regional scale. I utilized land surface phenology in conjunction with climatic predictors to examine change in the spatial distribution of *ventenata* across the BME, while controlling for climatic influence on the phenology. The difference between the *ventenata*'s distribution in 2006 and 2017 indicates that *ventenata* has primarily advanced from lower elevation shrublands into the ecotone between shrublands, woodlands, and open-pine forests. This is a cause for concern because the fine fuels from the addition of this species to the ecotone and forests may connect plant communities with a highly flammable fine fuel source. I also found that the occurrence or severity of large wildfires may be impacting the probability of *ventenata* presence in dry forest and ecotonal forest/nonforest settings.

Mapping the progression of an invasion from early stages to present is inherently challenging for several reasons. These analyses are useful, but the lag in wide-spread invasion (Aikio et al., 2010) and recognition from managers and policymakers present challenges in attaining observations from the earlier stages of invasion. The lack of early field data may be supplemented if remote sensing can

detect the species, but it also limits the ability of studies to field validate mapped results. The analyses of remote-sensing derived maps of species presence are also impacted by the model's accuracy from which they were produced (Langford et al., 2006; Liu et al., 2007). Classification error will impact the spatial patterns observed in model predictions. For this reason, I focused much of the analysis on broad scale trends across the BME. Future studies would benefit by considering additional factors related to wildfire. The complex processes related to fire and plant community response prevent the conclusive attribution of fire as the catalyst of *ventenata* spread. There were also limitations to the information I could derive from the data I employed to estimate fire occurrence and severity. I only examined large wildfires (i.e., > 405 ha), so I cannot guarantee that unburned areas did not burn during this period. Therefore, smaller wildfires or prescribed fire could be confounding some of the results I observed between 'wildfire' and 'non-wildfire' areas.

This dissertation has explored the use of multiple satellite data sources to detect and characterize the invasion of an annual grass in the interior Pacific Northwest. I identified both opportunities to refine land surface phenology estimates and limitations to the suite of ecosystems that can be accurately characterized with these data. The future of the *ventenata* invasion in the BME is presently uncertain, and information regarding this species is still in the early stages of development. However, the tools developed in this research to characterize the distribution of this species have provided evidence for its unique phenological and environmental characteristics. In addition, this allowed the exploration of changes in *ventenatas* biophysical and wildfire relationships through time. Given the progression of this invasion into the forested areas of the BME and the evidence of fire in these areas increasing the probability of this species, future research will need to focus on the mechanisms that promote or allow the establishment of this species in forested areas and post-fire environments.

BIBLIOGRAPHY

- Abadi, M., Agarwal, A., Barham, P., Brevdo, E., Chen, Z., Citro, C., Corrado, G.S., Davis, A., Dean, J., Devin, M., Ghemawat, S., Goodfellow, I., Harp, A., Irving, G., Isard, M., Jia, Y., Jozefowicz, R., Kaiser, L., Kudlur, M., Levenberg, J., Mane, D., Monga, R., Moore, S., Murray, D., Olah, C., Schuster, M., Shlens, J., Steiner, B., Sutskever, I., Talwar, K., Tucker, P., Vanhoucke, V., Vasudevan, V., Viegas, F., Vinyals, O., Warden, P., Wattenberg, M., Wicke, M., Yu, Y., Zheng, X., 2015. TensorFlow: Large-scale machine learning on heterogenous distributed systems. Software available from tensorflow.org.
- Abella, S.R., Springer, J.D., 2015. Effects of tree cutting and fire on understory vegetation in mixed conifer forests. *For. Ecol. Manage.* 335, 281–299. <https://doi.org/10.1016/j.foreco.2014.09.009>
- Aikio, S., Duncan, R.P., Hulme, P.E., 2010. Lag-phases in alien plant invasions: Separating the facts from the artefacts. *Oikos* 119, 370–378. <https://doi.org/10.1111/j.1600-0706.2009.17963.x>
- Andrew, M.E., Ustin, S.L., 2008. The role of environmental context in mapping invasive plants with hyperspectral image data. *Remote Sens. Environ.* 112, 4301–4317. <https://doi.org/10.1016/j.rse.2008.07.016>
- Anwar, M.R., Liu, D.L., Farquharson, R., Macadam, I., Abadi, A., Finlayson, J., Wang, B., Ramilan, T., 2015. Climate change impacts on phenology and yields of five broadacre crops at four climatologically distinct locations in Australia. *Agric. Syst.* 132, 133–144. <https://doi.org/10.1016/j.agsy.2014.09.010>
- Asner, G.P., Knapp, D.E., Kennedy-Bowdoin, T., Jones, M.O., Martin, R.E., Boardman, J., Hughes, R.F., 2008. Invasive species detection in Hawaiian rainforests using airborne imaging spectroscopy and LiDAR. *Remote Sens. Environ.* 112, 1942–1955. <https://doi.org/10.1016/j.rse.2007.11.016>
- Austin, M., 2007. Species distribution models and ecological theory: A critical assessment and some possible new approaches. *Ecol. Modell.* 200, 1–19. <https://doi.org/10.1016/j.ecolmodel.2006.07.005>
- Averett, J.P., Morris, L.R., Naylor, B.J., Taylor, R. V., Endress, B.A., 2020. Vegetation change over seven years in the largest protected Pacific Northwest Bunchgrass Prairie remnant. *PLoS One* 15, 1–20. <https://doi.org/10.1371/journal.pone.0227337>
- Badeck, F.-W., Bondeau, A., Böttcher, K., Doktor, D., Lucht, W., Schaber, J., Sitch, S., 2004. Responses of spring phenology to climate change. *New Phytol.* 162, 295–309. <https://doi.org/10.1111/j.1469-8137.2004.01059.x>
- Balch, J.K., Bradley, B.A., D'Antonio, C.M., Gómez-Dans, J., 2013. Introduced annual grass increases regional fire activity across the arid western USA (1980–2009). *Glob. Chang. Biol.* 19, 173–183. <https://doi.org/10.1111/gcb.12046>

- Barkworth, M.E., Capels, K.M., Long, S., 1993. Ventenata, in: Flora of North America: Volume 24: Magnoliophyta: Commelinidae (in Part): Poaceae, Part 1: North of Mexico. Oxford University Press, New York and Oxford, pp. 683–684.
- Beck, P.S.A., Atzberger, C., Høgda, K.A., Johansen, B., Skidmore, A.K., 2006. Improved monitoring of vegetation dynamics at very high latitudes: A new method using MODIS NDVI. *Remote Sens. Environ.* 100, 321–334. <https://doi.org/10.1016/j.rse.2005.10.021>
- Belgiu, M., Stein, A., 2019. Spatiotemporal image fusion in remote sensing. *Remote Sens.* 11, 818. <https://doi.org/10.3390/rs11070818>
- Blaschke, T., 2010. Object based image analysis for remote sensing. *ISPRS J. Photogramm. Remote Sens.* 65, 2–16. <https://doi.org/10.1016/j.isprsjprs.2009.06.004>
- Bolton, D.K., Gray, J.M., Melaas, E.K., Moon, M., Eklundh, L., Friedl, M.A., 2020. Continental-scale land surface phenology from harmonized Landsat 8 and Sentinel-2 imagery. *Remote Sens. Environ.* 240, 111685. <https://doi.org/10.1016/j.rse.2020.111685>
- Boyd, I.L., Freer-Smith, P.H., Gilligan, C.A., Godfray, H.C.J., 2013. The consequence of tree pests and diseases for ecosystem services. *Science* (80-.). 342. <https://doi.org/10.1126/science.1235773>
- Boyte, S.P., Wylie, B.K., 2016. Near-Real-Time Cheatgrass percent cover in the northern Great Basin, USA, 2015. *Rangelands* 38, 278–284. <https://doi.org/10.1016/j.rala.2016.08.002>
- Bradley, B.A., 2014. Remote detection of invasive plants: A review of spectral, textural and phenological approaches. *Biol. Invasions* 16, 1411–1425. <https://doi.org/10.1007/s10530-013-0578-9>
- Bradley, B.A., 2009. Regional analysis of the impacts of climate change on cheatgrass invasion shows potential risk and opportunity. *Glob. Chang. Biol.* 15, 196–208. <https://doi.org/10.1111/j.1365-2486.2008.01709.x>
- Bradley, B.A., Allen, J.M., O’Neill, M.W., Wallace, R.D., Barger, C.T., Richburg, J.A., Stinson, K., 2018. Invasive species risk assessments need more consistent spatial abundance data. *Ecosphere* 9, e02302. <https://doi.org/10.1002/ecs2.2302>
- Bradley, B.A., Curtis, C.A., Fusco, E.J., Abatzoglou, J.T., Balch, J.K., Dadashi, S., Tuanmu, M.-N., 2017. Cheatgrass (*Bromus tectorum*) distribution in the intermountain Western United States and its relationship to fire frequency, seasonality, and ignitions. *Biol. Invasions* 20, 1493–1506. <https://doi.org/10.1007/s10530-017-1641-8>
- Bradley, B.A., Mustard, J.F., 2006. Characterizing the landscape dynamics of an invasive plant and risk of invasion using remote sensing. *Ecol. Appl.* 16, 1132–1147. [https://doi.org/10.1890/1051-0761\(2006\)016\[1132:CTLDOA\]2.0.CO;2](https://doi.org/10.1890/1051-0761(2006)016[1132:CTLDOA]2.0.CO;2)

- Bradley, B.A., Mustard, J.F., 2008. Comparison of phenology trends by land cover class : a case study in the Great Basin , USA. *Glob. Chang. Biol.* 14, 334–346. <https://doi.org/10.1111/j.1365-2486.2007.01479.x>
- Bradley, B.A., Olsson, A.D., Wang, O., Dickson, B.G., Pelech, L., Sesnie, S.E., Zachmann, L.J., 2012. Species detection vs. habitat suitability: Are we biasing habitat suitability models with remotely sensed data? *Ecol. Modell.* 244, 57–64. <https://doi.org/10.1016/j.ecolmodel.2012.06.019>
- Breiman, L., 2001. Random forests. *Mach. Learn.* 45, 5–32.
- Brooks, M.L., 2008. Plant invasions and fire regimes. In: Zouhar, K., KaplerSmith, J., Sutherland, S., Brooks, M.L. (Eds.). *Wildland fire in ecosystems: fire and nonnative invasive plants*. RMRS-GTR-42-volume 6. Ogden, UT: USDA Forest Service, Rocky Mountain Research Station. p 33–46.
- Brooks, M.L., Brown, C.S., Chambers, J.C., D’Antonio, C.M., Keeley, J.E., Belnap, J., 2016. Exotic Annual Bromus Invasions: Comparisons Among Species and Ecoregions in the Western United States. https://doi.org/10.1007/978-3-319-24930-8_2
- Brooks, M.L., D’Antonio, C.M., Richardson, D.M., Grace, J.B., Keeley, J.E., DiTomaso, J.M., Hobbs, R.J., Pellant, M., Pyke, D., 2004. Effects of Invasive Alien Plants on Fire Regimes. *Bioscience* 54, 677–688. [https://doi.org/10.1641/0006-3568\(2004\)054\[0677:eoiapo\]2.0.co;2](https://doi.org/10.1641/0006-3568(2004)054[0677:eoiapo]2.0.co;2)
- Cai, Z., Jönsson, P., Jin, H., Eklundh, L., 2017. Performance of smoothing methods for reconstructing NDVI time-series and estimating vegetation phenology from MODIS data. *Remote Sens.* 9, 1271. <https://doi.org/10.3390/rs9121271>
- Chambers, J.C., Bradley, B.A., Brown, C.S., D’Antonio, C., Germino, M.J., Grace, J.B., Hardegree, S.P., Miller, R.F., Pyke, D.A., 2014a. Resilience to stress and disturbance, and resistance to *Bromus tectorum* L. invasion in cold desert shrublands of western North America. *Ecosystems* 17, 360–375. <https://doi.org/10.1007/s10021-013-9725-5>
- Chambers, J.C., Miller, R.F., Board, D.I., Pyke, D.A., Roundy, B.A., Grace, J.B., Schupp, E.W., Tausch, R.J., 2014b. Resilience and Resistance of Sagebrush Ecosystems: Implications for State and Transition Models and Management Treatments. *Rangel. Ecol. Manag.* 67, 440–454. <https://doi.org/10.2111/REM-D-13-00074.1>
- Chambers, J.C., Roundy, B.A., Blank, R.R., Meyer, S.E., Whittaker, A., 2007. What makes Great Basin sagebrush ecosystems invasible by *Bromus tectorum*? *Ecol. Monogr.* 77, 117–145. <https://doi.org/10.1890/05-1991>
- Chen, T., Guestrin, C., 2016. XGBoost: A Scalable Tree Boosting System, in: *Proceedings of the 22nd ACM SIGKDD International Conference on Knowledge Discovery and Data Mining*. San Francisco, CA, pp. 785–794. <https://doi.org/http://dx.doi.org/10.1145/2939672.2939785>

- Chen, B., Huang, B., Xu, B., 2015. Comparison of spatiotemporal fusion models: A review. *Remote Sens.* 7, 1798-1835. <https://doi.org/10.3390/rs70201798>
- Chen, X., Wang, D., Chen, J., Wang, C., Shen, M., 2018. The mixed pixel effect in land surface phenology: A simulation study. *Remote Sens. Environ.* 211, 338–344. <https://doi.org/10.1016/j.rse.2018.04.030>
- Cheney, C., Esler, K.J., Foxcroft, L.C., van Wilgen, N.J., McGeoch, M.A., 2018. The impact of data precision on the effectiveness of alien plant control programmes: a case study from a protected area. *Biol. Invasions* 20, 3227–3243. <https://doi.org/10.1007/s10530-018-1770-8>
- Cho, M.A., Mathieu, R., Asner, G.P., Naidoo, L., van Aardt, J., Ramoelo, A., Debba, P., Wessels, K., Main, R., Smit, I.P.J., Erasmus, B., 2012. Mapping tree species composition in South African savannas using an integrated airborne spectral and LiDAR system. *Remote Sens. Environ.* 125, 214–226. <https://doi.org/10.1016/j.rse.2012.07.010>
- Clarke, S.E., Bryce, S.A., 1997. Hierarchical Subdivisions of the Columbia Plateau and Blue Mountains Ecoregions, Oregon and Washington, Agriculture. Portland, OR. <https://doi.org/10.1029/2010WR009341>. Citation
- Clinton, N.E., Potter, C., Crabtree, B., Genovese, V., Gross, P., Gong, P., 2010. Remote Sensing–Based Time-Series Analysis of Cheatgrass (*L.*) Phenology. *J. Environ. Qual.* 39, 955. <https://doi.org/10.2134/jeq2009.0158>
- Cohen, J., 1960. A coefficient of agreement for nominal scales. *Educ. Psychol. Meas.* 37–46.
- Colautti, R.I., Ågren, J., Anderson, J.T., 2017. Phenological shifts of native and invasive species under climate change: Insights from the Boechera-Lythrum model. *Philos. Trans. R. Soc. B Biol. Sci.* 372, 20160032. <https://doi.org/10.1098/rstb.2016.0032>
- Coops, N.C., Hilker, T., Bater, C.W., Wulder, M.A., Nielsen, S.E., McDermid, G., Stenhouse, G., 2012. Linking ground-based to satellite-derived phenological metrics in support of habitat assessment. *Remote Sens. Lett.* 3, 191–200. <https://doi.org/10.1080/01431161.2010.550330>
- Cutler, D.R., Jr., T.C.E., Beard, K.H., Cutler, A., Hess, K.T., Gibson, J., Lawler, J.J., 2007. Random forests for classification in ecology. *Ecology* 88, 2783–2792.
- D’Antonio, C., Vitousek, P., 1992. Biological invasions by exotic grasses, the grass/fire cycle, and global change. *Annu. Rev. Ecol. Syst.* 23, 63–87. <https://doi.org/10.1146/annurev.es.23.110192.000431>.
- Dalponte, M., Bruzzone, L., Gianelle, D., 2012. Tree species classification in the Southern Alps based on the fusion of very high geometrical resolution multispectral/hyperspectral images and LiDAR data. *Remote Sens. Environ.* 123, 258–270. <https://doi.org/10.1016/j.rse.2012.03.013>

- de Beurs, K.M., Henebry, G.M., 2004. Land surface phenology, climatic variation, and institutional change: Analyzing agricultural land cover change in Kazakhstan. *Remote Sens. Environ.* 89, 497–509. <https://doi.org/10.1016/j.rse.2003.11.006>
- Dennison, P.E., Brewer, S.C., Arnold, J.D., Moritz, M.A., 2014. Large wildfire trends in the western United States, 1984–2011 *Philipp. Geophys. Res. Lett.* 41, 2928–2933. <https://doi.org/10.1002/2014GL059576>
- Dixit, A., Goswami, A., Jain, S., 2019. Development and evaluation of a new “Snow Water Index (SWI)” for accurate snow cover delineation. *Remote Sens.* 11, 2774. <https://doi.org/10.3390/rs11232774>
- Downing, W.M., Krawchuk, K.A., Meigs, G.W., Haire, S.L., Coop, J.D., Walker, R.B., Whitman, E., Chong, G., Miller, C., 2019. Influence of fire refugia spatial pattern on post-fire forest recovery in Oregon’s Blue Mountains [Dataset]. *Landsc. Ecol.* 34, 771–792. <https://doi.org/10.1007/s10980-019-00802-1>
- Eidenshink, J., Schwind, B., Brewer, K., Zhu, Z.-L., Quayle, B., Howard, S., 2007. A project for monitoring trends in burn severity. *Fire Ecol.* 3, 3–21. <https://doi.org/10.4996/fireecology.0301003>
- Eklundh, L., Hongxiao, J., Schubert, P., Radoslaw, G., Heliasz, M., 2011. An optical sensor network for vegetation phenology monitoring and satellite data calibration. *Sensors.* 11, 7678–7709. <https://doi.org/10.3390/s110807678>
- Eferink, E., van der Weijden, W., 2011. Ecoterrorism and biosecurity, in: Simberloff, D., Rejmanek, M. (Eds.), *Encyclopedia of Biological Invasions*. University of California Press, Berkeley, pp. 183–187.
- Elith, J., 2016. Predicting distributions of invasive species. pp. 1–28.
- Ellner, S.P., Schreiber, S.J., 2012. Temporally variable dispersal and demography can accelerate the spread of invading species. *Theor. Popul. Biol.* 82, 283–298. <https://doi.org/10.1016/j.tpb.2012.03.005>
- Elmore, A.J., Asner, G.P., Hughes, R.F., 2005. Satellite monitoring of vegetation phenology and fire fuel conditions in hawaiian drylands. *Earth Interact.* 9. <https://doi.org/10.1175/EI160.1>
- Emelyanova, I. V., McVicar, T.R., Van Niel, T.G., Li, L.T., van Dijk, A.I.J.M., 2013. Assessing the accuracy of blending Landsat-MODIS surface reflectances in two landscapes with contrasting spatial and temporal dynamics: A framework for algorithm selection. *Remote Sens. Environ.* 133, 193–209. <https://doi.org/10.1016/j.rse.2013.02.007>
- Endress, B.A., Averett, J.P., Naylor, B.J., Morris, L.R., Taylor, R. V., 2020. Non-native species threaten the biotic integrity of the largest remnant Pacific Northwest Bunchgrass prairie in the United States. *Appl. Veg. Sci.* 23, 53–68. <https://doi.org/10.1111/avsc.12464>

- Fielding, A.H., 2002. What are the appropriate characteristics of an accuracy measure?, in: Scott, J.M., Heglund, P.J., Morrison, M.L., Haufler, J.B., Raphael, M.G., Wall, W.A., Samson, F.B. (Eds.), *Predicting Species Occurrences: Issues of Accuracy and Scale*. Island Press, Covelo, CA, pp. 271–280.
- Fielding, A.H., Bell, J.F., 1997. A review of methods for the assessment of prediction errors in conservation presence/absence models. *Environ. Conserv.* 38–49.
- Filippa, G., Cremonese, E., Migliavacca, M., Galvagno, M., Sonnentag, O., Humphreys, E., Hufkens, K., Ryu, Y., Verfaillie, J., Morra di Cella, U., Richardson, A.D., 2018. NDVI derived from near-infrared-enabled digital cameras: Applicability across different plant functional types. *Agric. For. Meteorol.* 249, 275–285. <https://doi.org/10.1016/j.agrformet.2017.11.003>
- Fisher, J.I., Mustard, J.F., Vadeboncoeur, M.A., 2006. Green leaf phenology at Landsat resolution: Scaling from the field to the satellite. *Remote Sens. Environ.* 100, 265–279. <https://doi.org/10.1016/j.rse.2005.10.022>
- Flory, S.L., Bauer, J., Phillips, R.P., Clay, K., 2017. Effects of a non-native grass invasion decline over time. *J. Ecol.* 105, 1475–1484. <https://doi.org/10.1111/1365-2745.12850>
- Flory, S.L., Clay, K., Emery, S.M., Robb, J.R., Winters, B., 2015. Fire and non-native grass invasion interact to suppress tree regeneration in temperate deciduous forests. *J. Appl. Ecol.* 52, 992–1000. <https://doi.org/10.1111/1365-2664.12437>
- Foga, S., Scaramuzza, P.L., Guo, S., Zhu, Z., Dilley, R.D., Beckmann, T., Schmidt, G.L., Dwyer, J.L., Hughes, M.J., Laue, B., 2017. Cloud detection algorithm comparison and validation for operational Landsat data products. *Remote Sens. Environ.* 194, 379–390. <https://doi.org/10.1016/j.rse.2017.03.026>
- Forkel, M., Carvalhais, N., Rödenbeck, C., Keeling, R., Heimann, M., Thonicke, K., Zaehle, S., Reichstein, M., 2016. Enhanced seasonal CO₂ exchange caused by amplified plant productivity in northern ecosystems. *Science*. 351, 696–699. <https://doi.org/10.1126/science.aac4971>
- Forsyth, G.G., Le Maitre, D.C., O’Farrell, P.J., van Wilgen, B.W., 2012. The prioritisation of invasive alien plant control projects using a multi-criteria decision model informed by stakeholder input and spatial data. *J. Environ. Manage.* 103, 51–57. <https://doi.org/10.1016/j.jenvman.2012.01.034>
- Franklin, J., 2010. *Mapping Species Distributions: Spatial Inference and Prediction*. Cambridge University Press, Cambridge, UK.
- Freeman, E.A., Moisen, G.G., 2008. A comparison of the performance of threshold criteria for binary classification in terms of predicted prevalence and kappa. *Ecol. Modell.* 217, 48–58. <https://doi.org/10.1016/j.ecolmodel.2008.05.015>
- Friedl, M.A., Sulla-Menashe, D., Tan, B., Schneider, A., Ramankutty, N., Sibley, A., Huang, X., 2010. MODIS Collection 5 global land cover: Algorithm refinements

- and characterization of new datasets. *Remote Sens. Environ.* 114, 168–182.
<https://doi.org/10.1016/j.rse.2009.08.016>
- Funk, J.L., Parker, I.M., Matzek, V., Flory, S.L., Aschehoug, E.T., D'Antonio, C.M., Dawson, W., Thomson, D.M., Valliere, J., 2020. Keys to enhancing the value of invasion ecology research for management. *Biol. Invasions* 22, 2431–2445.
<https://doi.org/10.1007/s10530-020-02267-9>
- Fusco, E.J., Finn, J.T., Balch, J.K., Nagy, R.C., Bradley, B.A., 2019. Invasive grasses increase fire occurrence and frequency across US ecoregions. *Proc. Natl. Acad. Sci. USA* 116, 23594–23599. <https://doi.org/10.1073/pnas.1908253116>
- Galvão, L.S., Formaggio, A.R., Tisot, D.A., 2005. Discrimination of sugarcane varieties in Southeastern Brazil with EO-1 Hyperion data. *Remote Sens. Environ.* 94, 523–534. <https://doi.org/10.1016/j.rse.2004.11.012>
- Ganguly, S., Friedl, M.A., Tan, B., Zhang, X., Verma, M., 2010. Land surface phenology from MODIS: Characterization of the Collection 5 global land cover dynamics product. *Remote Sens. Environ.* 114, 1805–1816.
<https://doi.org/10.1016/j.rse.2010.04.005>
- Gao, F., Anderson, M., Daughtry, C., Karnieli, A., Hively, D., Kustas, W., 2020. A within-season approach for detecting early growth stages in corn and soybean using high temporal and spatial resolution imagery. *Remote Sens. Environ.* 242, 111752. <https://doi.org/10.1016/j.rse.2020.111752>
- Gao, F., Anderson, M.C., Zhang, X., Yang, Z., Alfieri, J.G., Kustas, W.P., Mueller, R., Johnson, D.M., Prueger, J.H., 2017. Toward mapping crop progress at field scales through fusion of Landsat and MODIS imagery. *Remote Sens. Environ.* 188, 9–25. <https://doi.org/10.1016/j.rse.2016.11.004>
- Gao, F., Hilker, T., Zhu, X., Anderson, M., Masek, J., Wang, P., and Yang, Y. 2015. Fusing Landsat and MODIS data for vegetation monitoring. *IEEE Geosci. Remote Sens.* 3, 47-60. <https://doi.org/10.1109/MGRS.2015.2434351>
- Gao, F., Masek, J., Schwaller, M., Hall, F., 2006. On the blending of the Landsat and MODIS surface reflectance: predicting daily Landsat surface reflectance. *IEEE Trans. Geosci. Remote Sens.* 44, 2207–2218.
<https://doi.org/10.1109/TGRS.2006.872081>
- Gavier-Pizarro, G.I., Kuemmerle, T., Hoyos, L.E., Stewart, S.I., Huebner, C.D., Keuler, N.S., Radeloff, V.C., 2012. Monitoring the invasion of an exotic tree (*Ligustrum lucidum*) from 1983 to 2006 with Landsat TM/ETM+ satellite data and Support Vector Machines in Córdoba, Argentina. *Remote Sens. Environ.* 122, 134–145.
<https://doi.org/10.1016/j.rse.2011.09.023>
- Gesch, D.B., Evans, G.A., Oimoen, M.J., Arundel, S., 2018. The National Elevation Dataset, in: *Photogrammetric Engineering & Remote Sensing*. American Society of Photogrammetry and Remote Sensing, pp. 83–110.

- Gillanders, S.N., Coops, N.C., Wulder, M.A., Gergel, S.E., Nelson, T., 2008. Multitemporal remote sensing of landscape dynamics and pattern change: Describing natural and anthropogenic trends. *Prog. Phys. Geogr.* 32, 503–528. <https://doi.org/10.1177/0309133308098363>
- Giometto, A., Rinaldo, A., Carrara, F., Altermatt, F., 2014. Emerging predictable features of replicated biological invasion fronts. *Proc. Natl. Acad. Sci. USA* 111, 297–301. <https://doi.org/10.1073/pnas.1321167110>
- Gorelick, N., Hancher, M., Dixon, M., Ilyushchenko, S., Thau, D., Moore, R., 2017. Google Earth Engine: Planetary-scale geospatial analysis for everyone. *Remote Sens. Environ.* 202, 18–27. <https://doi.org/10.1016/j.rse.2017.06.031>
- Große-Stoltenberg, A., Hellmann, C., Werner, C., Oldeland, J., Thiele, J., 2016. Evaluation of continuous VNIR-SWIR spectra versus narrowband hyperspectral indices to discriminate the invasive *Acacia longifolia* within a mediterranean dune ecosystem. *Remote Sens.* 8. <https://doi.org/10.3390/rs8040334>
- Guisan, A., Thuiller, W., 2005. Predicting species distribution: Offering more than simple habitat models. *Ecol. Lett.* 8, 993–1009. <https://doi.org/10.1111/j.1461-0248.2005.00792.x>
- Gunderson, L.H., 2000. Ecological resilience-In theory and application. *Annu. Rev. Ecol. Syst.* 31, 425–439. <https://www.jstor.org/stable/221739>
- Hardegree, S.P., Moffet, C.A., Roundy, B.A., Jones, T.A., Novak, S.J., Clark, P.E., Pierson, F.B., Flerchinger, G.N., 2010. A comparison of cumulative-germination response of cheatgrass (*Bromus tectorum* L.) and five perennial bunchgrass species to simulated field-temperature regimes. *Environ. Exp. Bot.* 69, 320–327. <https://doi.org/10.1016/j.envexpbot.2010.04.012>
- Hardisty, A.R., Belbin, L., Hobern, D., McGeoch, M.A., Pirzl, R., Williams, K.J., Kissling, W.D., 2019. Research infrastructure challenges in preparing essential biodiversity variables data products for alien invasive species. *Environ. Res. Lett.* 14, Article 025005. <https://doi.org/10.1088/1748-9326/aaf5db>
- Harris, G.A., Wilson, A.M., 1970. Competition for Moisture among Seedlings of Annual and Perennial Grasses as Influenced by Root Elongation at Low Temperature. *Ecology* 51, 530–534. <https://doi.org/10.2307/1935392>
- Harvey, A.J., Rew, L.J., Prather, T.S., Mangold, J.M., 2020. Effects of Elevated Temperature and CO2 Concentration on Seedling Growth of. *Agronomy* 1–9.
- He, K.S., Bradley, B.A., Cord, A.F., Rocchini, D., Tuanmu, M.N., Schmidtlein, S., Turner, W., Wegmann, M., Pettorelli, N., 2015. Will remote sensing shape the next generation of species distribution models? *Remote Sens. Ecol. Conserv.* 1, 4–18. <https://doi.org/10.1002/rse2.7>

- Hellmann, J.J., Byers, J.E., Bierwagen, B.G., Dukes, J.S., 2008. Five potential consequences of climate change for invasive species. *Conserv. Biol.* 22, 534–543. <https://doi.org/10.1111/j.1523-1739.2008.00951.x>
- Hepting, G.H., 1974. Death of the American Chestnut. *J. For. Hist.* 18, 60–67.
- Hilker, T., Wulder, M.A., Coops, N.C., Linke, J., McDermid, G., Masek, J.G., Gao, F., White, J.C., 2009a. A new data fusion model for high spatial- and temporal-resolution mapping of forest disturbance based on Landsat and MODIS. *Remote Sens. Environ.* 113, 1613–1627. <https://doi.org/10.1016/j.rse.2009.03.007>
- Hilker, T., Wulder, M.A., Coops, N.C., Seitz, N., White, J.C., Gao, F., Masek, J.G., Stenhouse, G., 2009b. Generation of dense time series synthetic Landsat data through data blending with MODIS using a spatial and temporal adaptive reflectance fusion model. *Remote Sens. Environ.* 113, 1988–1999. <https://doi.org/10.1016/j.rse.2009.05.011>
- Hill, R.A., Thomson, A.G., 2005. Mapping woodland species composition and structure using airborne spectral and LiDAR data. *Int. J. Remote Sens.* 26, 3763–3779. <https://doi.org/10.1080/01431160500114706>
- Hoyos, L.E., Gavier-Pizarro, G.I., Kuemmerle, T., Bucher, E.H., Radeloff, V.C., Tecco, P.A., 2010. Invasion of glossy privet (*Ligustrum lucidum*) and native forest loss in the Sierras Chicas of Córdoba, Argentina. *Biol. Invasions* 12, 3261–3275. <https://doi.org/10.1007/s10530-010-9720-0>
- Huang, C., Asner, G.P., 2009. Applications of Remote Sensing to Alien Invasive Plant Studies. *Sensors* 9, 4869–4889. <https://doi.org/10.3390/s90604869>
- Hufkens, K., Friedl, M., Sonnentag, O., Braswell, B.H., Milliman, T., Richardson, A.D., 2012. Linking near-surface and satellite remote sensing measurements of deciduous broadleaf forest phenology. *Remote Sens. Environ.* 117, 307–321. <https://doi.org/10.1016/j.rse.2011.10.006>
- Hulme, P.E., 2011. Biosecurity: the changing face of invasion biology, in: Richardson, D.M. (Ed.), *Fifty Years of Invasion Ecology: The Legacy of Charles Elton*. Wiley, pp. 301–314.
- Irisarri, J.G.N., Oesterheld, M., Verón, S.R., Paruelo, J.M., 2009. Grass species differentiation through canopy hyperspectral reflectance. *Int. J. Remote Sens.* 30, 5959–5975. <https://doi.org/10.1080/01431160902791895>
- Jarihani, A.A., McVicar, T.R., Van Niel, T.G., Emelyanova, I.V., Callow, J.N., Johansen, K., 2014. Blending Landsat and MODIS data to generate multispectral indices: A comparison of “index-then-blend” and “blend-then-index” approaches. *Remote Sens.* 6, 9213–9218. <https://doi.org/10.3390/rs6109213>
- Jetz, W., McGeoch, M.A., Guralnick, R., Ferrier, S., Beck, J., Costello, M.J., Fernandez, M., Geller, G.N., Keil, P., Merow, C., Meyer, C., Muller-Karger, F.E., Pereira, H.M., Regan, E.C., Schmeller, D.S., Turak, E., 2019. Essential biodiversity

- variables for mapping and monitoring species populations. *Nat. Ecol. Evol.* 3, 539–551. <https://doi.org/10.1038/s41559-019-0826-1>
- Jetz, W., McPherson, J.M., Guralnick, R.P., 2012. Integrating biodiversity distribution knowledge: Toward a global map of life. *Trends Ecol. Evol.* 27, 151–159. <https://doi.org/10.1016/j.tree.2011.09.007>
- Johnson, C.G., Swanson, D.K., 2005. Bunchgrass plant communities of the Blue and Ochoco Mountains: A guide for managers. PNW-GTR-641. Portland, OR: USDA Forest Service, Pacific Northwest Research Station.
- Jones, L.C., Norton, N., Prather, T.S., 2018. Indicators of *Venttenata* (*Venttenata dubia*) Invasion in Sagebrush Steppe Rangelands. *Invasive Plant Sci. Manag.* 11, 1–9. <https://doi.org/10.1017/inp.2018.7>
- Jönsson, P., Eklundh, L., 2004. TIMESAT - A program for analyzing time-series of satellite sensor data. *Comput. Geosci.* 30, 833–845. <https://doi.org/10.1016/j.cageo.2004.05.006>
- Jönsson, P., Eklundh, L., 2002. Seasonality extraction by function fitting to time-series of satellite sensor data. *IEEE Trans. Geosci. Remote Sens.* 40, 1824–1832. <https://doi.org/10.1109/TGRS.2002.802519>
- Keeley, J., Baer-Keeley, M., Fotheringham, C., 2005. Alien Plant Dynamics Following Fire in Mediterranean-Climate California Shrublands. *Ecol. Appl.* 15, 2109–2125.
- Keeley, J.E., Brennan, T.J., 2012. Fire-driven alien invasion in a fire-adapted ecosystem. *Oecologia* 169, 1043–1052. <https://doi.org/10.1007/s00442-012-2253-8>
- Kerns, B.K., Day, M.A., 2017. The importance of disturbance by fire and other abiotic and biotic factors in driving cheatgrass invasion varies based on invasion stage. *Biol. Invasions* 19, 1853–1862. <https://doi.org/10.1007/s10530-017-1395-3>
- Kerns, B.K., Tortorelli, C., Day, M.A., Nietupski, T., Barros, A.M.G., Kim, J.B., Krawchuk, M.A., 2020. Invasive grasses: A new perfect storm for forested ecosystems? *For. Ecol. Manage.* 463, 117985. <https://doi.org/10.1016/j.foreco.2020.117985>
- Kimothi, M.M., Dasari, A., 2010. Methodology to map the spread of an invasive plant (*Lantana camara* L.) in forest ecosystems using Indian remote sensing satellite data. *Int. J. Remote Sens.* 31, 3273–3289. <https://doi.org/10.1080/01431160903121126>
- Knapp, P.A., 1996. Cheatgrass (*Bromus tectorum* L.) dominance in the Great Basin Desert: History, persistence, and influences to human activities. *Glob. Environ. Chang.* 6, 37–52.
- Langford, W.T., Gergel, S.E., Dietterich, T.G., Cohen, W., 2006. Map misclassification can cause large errors in landscape pattern indices: Examples from habitat

- fragmentation. *Ecosystems* 9, 474–488. <https://doi.org/10.1007/s10021-005-0119-1>
- Latombe, G., Pyšek, P., Jeschke, J.M., Blackburn, T.M., Bacher, S., Capinha, C., Costello, M.J., Fernández, M., Gregory, R.D., Hobern, D., Hui, C., Jetz, W., Kumschick, S., McGrannachan, C., Pergl, J., Roy, H.E., Scalera, R., Squires, Z.E., Wilson, J.R.U., Winter, M., Genovesi, P., McGeoch, M.A., 2017. A vision for global monitoring of biological invasions. *Biol. Conserv.* 213, 295–308. <https://doi.org/10.1016/j.biocon.2016.06.013>
- Lawrence, C.E., 2015. Responses of Pacific Northwest prairies to soil nutrient manipulations: implications for restoration of *Castilleja levisecta* and control of invasive species [Dataset; Master's thesis]. *Oreg. St. Univ.*
- Levenberg, K., 1944. A method for the solution of certain non-linear problems in least squares. *Q. Appl. Math.* 2, 164–168.
- Levine, J.M., D'Antonio, C.M., 2003. Forecasting biological invasions with increasing international trade. *Conserv. Biol.* 17, 322–326. <https://doi.org/10.1046/j.1523-1739.2003.02038.x>
- Levine, J.M., Vilà, M., D'Antonio, C.M., Dukes, J.S., Grigulis, K., Lavorel, S., 2003. Mechanisms underlying the impacts of exotic plant invasions. *Proc. R. Soc. B Biol. Sci.* 270, 775–781. <https://doi.org/10.1098/rspb.2003.2327>
- Liang, L., Schwartz, M.D., Wang, Z., Gao, F., Schaaf, C.B., Tan, B., Morisette, J.T., Zhang, X., 2014. A cross comparison of spatiotemporally enhanced springtime phenological measurements from satellites and ground in a northern U.S. mixed forest. *IEEE Trans. Geosci. Remote Sens.* 52, 7513–7526. <https://doi.org/10.1109/TGRS.2014.2313558>
- Liao, L., Song, J., Wang, Jindi, Xiao, Z., Wang, Jian, 2016. Bayesian method for building frequent Landsat-like NDVI datasets by integrating MODIS and Landsat NDVI. *Remote Sens.* 8, 452. <https://doi.org/10.3390/rs8060452>
- Lieth, H., 1974. *Phenology and seasonality modeling*. Springer-Verlag, New York, NY.
- Littell, J.S., Mckenzie, D., Peterson, D.L., Westerling, A.L., 2009. Climate and wildfire area burned in western U.S. ecoprovinces, 1916–2003. *Ecol. Appl.* 19, 1003–1021. <https://doi.org/10.1890/07-1183.1>
- Liu, C., Frazier, P., Kumar, L., 2007. Comparative assessment of the measures of thematic classification accuracy. *Remote Sens. Environ.* 107, 606–616. <https://doi.org/10.1016/j.rse.2006.10.010>
- Mack, M.C., D'Antonio, C.M., 1998. Impacts of biological invasions on disturbance regimes. *Trends Ecol. Evol.* 13, 195–198. https://doi.org/10.1007/978-4-431-67879-3_7

- Mack, R.N., 1981. Invasion of *Bromus tectorum* L. into Western North America: An ecological chronicle. *Agro-Ecosystems* 7, 145–165.
[https://doi.org/https://doi.org/10.1016/0304-3746\(81\)90027-5](https://doi.org/https://doi.org/10.1016/0304-3746(81)90027-5)
- Mäyrä, J., Keski-Saari, S., Kivinen, S., Tanhuanpää, T., Hurskainen, P., Kullberg, P., Poikolainen, L., Viinikka, A., Tuominen, S., Kumpula, T., Vihervaara, P., 2021. Tree species classification from airborne hyperspectral and LiDAR data using 3D convolutional neural networks. *Remote Sens. Environ.* 256.
<https://doi.org/10.1016/j.rse.2021.112322>
- McGeoch, M.A., Latombe, G., 2016. Characterizing common and range expanding species. *J Biogeogr.* 43, 217–228. <https://doi.org/10.1111/jbi.12642>
- McMaster, G.S., Wilhelm, W.W., 1997. Growing degree-days: one equation, two interpretations. *Agric. For. Meteorol.* 87, 291–300.
- Melaas, E.K., Friedl, M.A., Zhu, Z., 2013. Detecting interannual variation in deciduous broadleaf forest phenology using Landsat TM/ETM+ data. *Remote Sens. Environ.* 132, 176–185. <https://doi.org/10.1016/j.rse.2013.01.011>
- Melaas, E.K., Sulla-Menashe, D., Gray, J.M., Black, T.A., Morin, T.H., Richardson, A.D., Friedl, M.A., 2016. Multisite analysis of land surface phenology in North American temperate and boreal deciduous forests from Landsat. *Remote Sens. Environ.* 186, 452–464. <https://doi.org/10.1016/j.rse.2016.09.014>
- Meyer, S.E., Allen, P.S., Beckstead, J., 1997. Seed Germination Regulation in *Bromus tectorum* (Poaceae) and Its Ecological Significance. *Oikos* 78, 475–485.
- Miller, G., Friedel, M., Adam, P., Chewings, V., 2010. Ecological impacts of buffel grass (*Cenchrus ciliaris* L.) invasion in central Australia – does field evidence support a fire-invasion feedback? *Rangel. J.* 32, 353–365.
<https://doi.org/10.1071/RJ09076>
- Miller, J.D., Knapp, E.E., Key, C.H., Skinner, C.N., Isbell, C.J., Creasy, R.M., Sherlock, J.W., 2009. Calibration and validation of the relative differenced Normalized Burn Ratio (RdNBR) to three measures of fire severity in the Sierra Nevada and Klamath Mountains, California, USA. *Remote Sens. Environ.* 113, 645–656.
<https://doi.org/10.1016/j.rse.2008.11.009>
- Morellato, L.P.C., Alberton, B., Alvarado, S.T., Borges, B., Buisson, E., Camargo, M.G.G., Cancian, L.F., Carstensen, D.W., Escobar, D.F.E., Leite, P.T.P., Mendoza, I., Rocha, N.M.W.B., Soares, N.C., Silva, T.S.F., Staggemeier, V.G., Streher, A.S., Vargas, B.C., Peres, C.A., 2016. Linking plant phenology to conservation biology. *Biol. Conserv.* 195, 60–72. <https://doi.org/10.1016/j.biocon.2015.12.033>
- Moreno-Martínez, Á., Izquierdo-Verdiguier, E., Maneta, M.P., Camps-Valls, G., Robinson, N., Muñoz-Marí, J., Sedano, F., Clinton, N., Running, S.W., 2020. Multispectral high resolution sensor fusion for smoothing and gap-filling in the cloud. *Remote Sens. Environ.* 247, 111901.
<https://doi.org/10.1016/j.rse.2020.111901>

- Newville, M., Stensitzki, T., Allen, D.B., Ingargiola, A., 2014. LMFIT: Non-linear least-square minimization and curve-fitting for Python. <https://doi.org/https://dx.doi.org/10.5281/zenodo.11813>
- Nicholson, S.E., Farrar, T.J., 1994. The Influence of soil type on the relationships between NDVI, rainfall, and soil moisture in semiarid Botswana. *Remote Sens. Environ.* 50, 107–120.
- Nicolli, M., Rodhouse, T.J., Stucki, D.S., Shinderman, M., 2020. Rapid Invasion by the Annual Grass *Ventena dubia* into Protected-Area, Low-Elevation Sagebrush Steppe. *West. North Am. Nat.* 80, 243–252. <https://doi.org/10.3398/064.080.0212>
- Nietupski, T.C., Kennedy, R.E., Temesgen, H., Kerns, B.K., 2021. Spatiotemporal image fusion in Google Earth Engine for annual estimates of land surface phenology in a heterogenous landscape. *Int. J. Appl. Earth Obs. Geoinf.* 99, 102323. <https://doi.org/10.1016/j.jag.2021.102323>
- Nijland, W., Bolton, D.K., Coops, N.C., Stenhouse, G., 2016. Imaging phenology; scaling from camera plots to landscapes. *Remote Sens. Environ.* 177, 13–20. <https://doi.org/10.1016/j.rse.2016.02.018>
- Noone, M.D., J.S.K. and E.M.N., 2013. Western Juniper and Invasive Annual Grass Mapping in Eastern Oregon. *Inst. Nat. Resour. Portl. State Univ.* 57 pp.
- Norris J.R., Walker J.J., 2020. Solar and sensor geometry, not vegetation response, drive satellite NDVI phenology in widespread ecosystems of the western United States. *Remote Sens. Environ.* 249, 112013. <https://doi.org/10.1016/j.rse.2020.112013>
- Noujdina, N. V., Ustin, S.L., 2008. Mapping Downy Brome (*Bromus tectorum*) Using Multidate AVIRIS Data. *Weed Sci.* 56, 173–179. <https://doi.org/10.1614/WS-07-009.1>
- Olsson, A.D., van Leeuwen, W.J.D., Marsh, S.E., 2011. Feasibility of invasive grass detection in a desertscrub community using hyperspectral field measurements and landsat TM imagery. *Remote Sens.* 3, 2283–2304. <https://doi.org/10.3390/rs3102283>
- Omernik, J.M., 1987. Ecoregions of the conterminous United States. *Ann. Assoc. Am. Geogr.* 77, 118–125.
- Parks, S.A., Holsinger, L.M., Voss, M.A., Loehman, R.A., Robinson, N.P., 2018. Mean composite fire severity metrics computed with google earth engine offer improved accuracy and expanded mapping potential. *Remote Sens.* 10, 1–15. <https://doi.org/10.3390/rs10060879>
- Paruelo, J.M., Lauenroth, W.K., 1998. Interannual variability of NDVI and its relationship to climate for North American shrublands and grasslands. *J Biogeogr.* 25, 721–733. <https://doi.org/10.1046/j.1365-2699.1998.2540721.x>

- Pasquarella, V.J., Holden, C.E., Kaufman, L., Woodcock, C.E., 2016. From imagery to ecology: leveraging time series of all available Landsat observations to map and monitor ecosystem state and dynamics. *Remote Sens. Ecol. Conserv.* 2, 152–170. <https://doi.org/10.1002/rse2.24>
- Pastick, N.J., Dahal, D., Wylie, B.K., Parajuli, S., Boyte, S.P., Wu, Z., 2020. Characterizing land surface phenology and exotic annual grasses in dryland ecosystems using landsat and sentinel-2 data in harmony. *Remote Sens.* 12, 1–17. <https://doi.org/10.3390/rs12040725>
- Pearlstine, L., Portier, K.M., Smith, S.E., 2005. Textural discrimination of an invasive plant, *Schinus terebinthifolius*, from low altitude aerial digital imagery. *Photogramm. Eng. Remote Sensing* 71, 289–298. <https://doi.org/10.14358/PERS.71.3.289>
- Peeler, J.L., Smithwick, E.A.H., 2018. Exploring invasibility with species distribution modeling: How does fire promote cheatgrass (*Bromus tectorum*) invasion within lower montane forests? *Divers. Distrib.* 24, 1308–1320. <https://doi.org/10.1111/ddi.12765>
- Pejchar, L., Mooney, H.A., 2009. Invasive species, ecosystem services and human well-being. *Trends Ecol. Evol.* 24, 497–504. <https://doi.org/10.1016/j.tree.2009.03.016>
- Penuelas, J., Rutishauser, T., Filella, I., 2010. Phenology feedbacks on climate change. *Science* 324, 887–888. <https://doi.org/10.1126/science.1173004>
- Petach, A.R., Toomey, M., Aubrecht, D.M., Richardson, A.D., 2014. Monitoring vegetation phenology using an infrared-enabled security camera. *Agric. For. Meteorol.* 195–196, 143–151. <https://doi.org/10.1016/j.agrformet.2017.11.003>
- Peters, A.J., Walter-Shea, E.A., Ji, L., Vina, A., Hayes, M., Svoboda, M.R., 2002. Drought monitoring with NDVI-based standardized vegetation index. *Photogramm. Eng. Remote Sens.* 68, 71–75.
- Peterson, A.T., 2003. Predicting the Geography of Species' Invasions via Ecological Niche Modeling. *Q. Rev. Biol.* 78, 419–433.
- Peterson, E.B., 2005. Estimating cover of an invasive grass (*Bromus tectorum*) using tobit regression and phenology derived from two dates of Landsat ETM + data. *Int. J. Remote Sens.* 26, 2491–2507. <https://doi.org/10.1080/01431160500127815>
- Petty, A.M., Setterfield, S.A., Ferdinands, K.B., Barrow, P., 2012. Inferring habitat suitability and spread patterns from large-scale distributions of an exotic invasive pasture grass in north Australia. *J. Appl. Ecol.* 49, 742–752. <https://doi.org/10.1111/j.1365-2664.2012.02128.x>

- Pilliod, D.S., Welty, J.L., and Arkle R.S., 2017. Refining the cheatgrass-fire cycle in the Great Basin: Precipitation timing and fine fuel composition predict wildfire trends. *Ecol. and Evol.* 7, 8126-8151. <https://doi.org/10.1002/ece3.3414>
- Pimentel, D., Zuniga, R., Morrison, D., 2005. Update on the environmental and economic costs associated with alien-invasive species in the United States. *Ecol. Econ.* <https://doi.org/10.1016/j.ecolecon.2004.10.002>
- Potter, C.S., Brooks, V., 1998. Global analysis of empirical relations between annual climate and seasonality of NDVI. *Int. J. Remote Sens.* 19, 2921–2948. <https://doi.org/10.1080/014311698214352>
- PRISM Climate Group. 2012. Norm81m. Oregon State University. Version 14.1. <http://prism.oregonstate.edu>.
- Pyšek, P., Richardson, D.M., 2010. Invasive species, environmental change and management, and health. *Annu. Rev. Environ. Resour.* 35, 25–55. <https://doi.org/10.1146/annurev-environ-033009-095548>
- Rao, Y., Zhu, X., Chen, J., Wang, J., 2015. An improved method for producing high spatial-resolution NDVI time series datasets with multi-temporal MODIS NDVI data and Landsat TM/ETM+ images. *Remote Sens.* 7, 7865–7891. <https://doi.org/10.3390/rs70607865>
- Reilly, M.J., McCord, M.G., Brandt, S.M., Linowksi, K.P., Butz, R.J., Jules, E.S., 2020. Repeated, high-severity wildfire catalyzes invasion of non-native plant species in forests of the Klamath Mountains, northern California, USA. *Biol. Invasions* 22, 1821–1828. <https://doi.org/10.1007/s10530-020-02227-3>
- Richardson, A.D., Braswell, B.H., Hollinger, D.Y., Jenkins, J.P., Ollinger, S. V., 2009. Near-surface remote sensing of spatial and temporal variation in canopy phenology. *Ecol. Appl.* 19, 1417–1428. <https://doi.org/10.1890/08-2022.1>
- Richardson, A.D., Anderson, R.S., Arain, M.A., Barr, A.G., Bohrer, G., Chen, G., Chen, J.M., Ciais, P., Davis, K.J., Desai, A.R., Dietze, M.C., Dragoni, D., Garrity, S.R., Gough, C.M., Grant, R., Hollinger, D.Y., Margolis, H.A., Mccaughey, H., Migliavacca, M., Monson, R.K., Munger, J.W., Poulter, B., Raczka, B.M., Ricciuto, D.M., Sahoo, A.K., Schaefer, K., Tian, H., Vargas, R., Verbeeck, H., Xiao, J., Xue, Y., 2012. Terrestrial biosphere models need better representation of vegetation phenology: Results from the North American Carbon Program Site Synthesis. *Glob. Chang. Biol.* 18, 566–584. <https://doi.org/10.1111/j.1365-2486.2011.02562.x>
- Richardson, A.D., Hufkens, K., Milliman, T., Aubrecht, D.M., Chen, M., Gray, J.M., Johnston, M.R., Keenan, T.F., Klosterman, S.T., Kosmala, M., Melaas, E.K., Friedl, M.A., Frohling, S., 2018a. Tracking vegetation phenology across diverse North American biomes using PhenoCam imagery. *Sci. Data* 5, 1–24. <https://doi.org/10.1038/sdata.2018.28>

- Richardson, A.D., Hufkens, K., Milliman, T., Frohling, S., 2018b. Intercomparison of phenological transition dates derived from the PhenoCam Dataset V1.0 and MODIS satellite remote sensing. *Sci. Rep.* 8, 5679. <https://doi.org/10.1038/s41598-018-23804-6>
- Richardson, A.D., Keenan, T.F., Migliavacca, M., Ryu, Y., Sonnentag, O., Toomey, M., 2013. Climate change, phenology, and phenological control of vegetation feedbacks to the climate system. *Agric. For. Meteorol.* 169, 156–173. <https://doi.org/10.1016/j.agrformet.2012.09.012>
- Richardson, D.M., Pyšek, P., Rejmánek, M., Barbour, M.G., Panetta, F.D., West, C.J., 2000. Naturalization and invasion of alien plants: Concepts and definitions. *Divers. Distrib.* 6, 93–107. <https://doi.org/10.1046/j.1472-4642.2000.00083.x>
- Ridder, L.W., Perren, J.A.M., Morris, L.R., Endress, B.A., Taylor, R.V., Naylor, B.J., 2021. Historical Fire and *Ventenata dubia* Invasion in a Temperate Grassland. *Rangel. Ecol. Manag.* 75, 35–40. <https://doi.org/10.1016/j.rama.2020.11.006>
- Rouse, J.W., Haas, R.H., Schell, J.A., Deering, D.W., 1973. Monitoring the vernal advancement and retrogradation (green wave effect) of natural vegetation. Greenbelt, MD, USA.
- Roy, D.P., Kovalskyy, V., Zhang, H.K., Vermote, E.F., Yan, L., Kumar, S.S., Egorov, A., 2016. Characterization of Landsat-7 to Landsat-8 reflective wavelength and normalized difference vegetation index continuity. *Remote Sens. Environ.* 185, 57–70. <https://doi.org/10.1016/j.rse.2015.12.024>
- Royimani, L., Mutanga, O., Odindi, J., Dube, T., Matongera, T.N., 2019. Advancements in satellite remote sensing for mapping and monitoring of alien invasive plant species (AIPs). *Phys. Chem. Earth* 112, 237–245. <https://doi.org/10.1016/j.pce.2018.12.004>
- Rupasinghe, P.A., Chow-Fraser, P., 2021. Mapping Phragmites cover using WorldView 2/3 and Sentinel 2 images at Lake Erie Wetlands, Canada. *Biol. Invasions* 0. <https://doi.org/10.1007/s10530-020-02432-0>
- Russelle, M.P., Wilhelm, W.W., Olson, R.A., Power, J.F., 1984. Growth Analysis Based on Degree Days. *Crop Sci.* 24, 28–32. <https://doi.org/10.2135/cropsci1984.0011183x002400010007x>
- Santos, M.J., Khanna, S., Hestir, E.L., Greenberg, J.A., Ustin, S.L., 2016. Measuring landscape-scale spread and persistence of an invaded submerged plant community from airborne remote sensing. *Ecol. Appl.* 26, 1733–1744. <https://doi.org/10.1890/15-0615>
- Scalera, R., 2010. How much is Europe spending on invasive alien species? *Biol. Invasions* 12, 173–177. <https://doi.org/10.1007/s10530-009-9440-5>
- Schaaf, C.B., Gao, F., Strahler, A.H., Lucht, W., Li, X., Tsang, T., Strugnell, N.C., Zhang, X., Jin, Y., Muller, J.-P., Lewis, P., Barnsley, M., Hobson, P., Disney, M., Roberts,

- G., Dunderdale, M., Doll, C., D'Entremont, R.P., Hu, B., Liang, S., Privette, J.L., Roy, D., 2002. First operational BRDF , albedo nadir reflectance products from MODIS. *Remote Sens. Environ.* 83, 135–148. [https://doi.org/10.1016/S0034-4257\(02\)00091-3](https://doi.org/10.1016/S0034-4257(02)00091-3)
- Scheinost, P., Stannard, M., Prather, T., 2008. *Plant Guide: Ventenata*. NRCS.
- Syednasrollah, B., Young, A.M., Hufkens, K., Milliman, T., Friedl, M.A., Frohling, S., Richardson, A.D., 2019. Tracking vegetation phenology across diverse biomes using Version 2.0 of the PhenoCam Dataset. *Sci. Data.* 6, 222. <https://doi.org/10.1038/s41597-019-0229-9>
- Shackleton, R.T., Shackleton, C.M., Kull, C.A., 2019. The role of invasive alien species in shaping local livelihoods and human well-being: A review. *J. Environ. Manage.* 229, 145–157. <https://doi.org/10.1016/j.jenvman.2018.05.007>
- Simberloff, D., Martin, J.L., Genovesi, P., Maris, V., Wardle, D.A., Aronson, J., Courchamp, F., Galil, B., García-Berthou, E., Pascal, M., Pyšek, P., Sousa, R., Tabacchi, E., Vilà, M., 2013. Impacts of biological invasions: What's what and the way forward. *Trends Ecol. Evol.* 28, 58–66. <https://doi.org/10.1016/j.tree.2012.07.013>
- Simpson, M.J., Kertis, J., Acker, S., Hochhalter, P., Nathanson, A., DeMeo, T., 2019. Potential Vegetation Types of California, Oregon, and Washington at the Vegzone and Subzone scale.
- Song, H., Liu, Q., Wang, G., Hang, R., Huang, B., 2018. Spatiotemporal satellite image fusion using deep convolutional neural networks. *IEEE J. Sel. Top. Appl. Earth Obs. Remote Sens.* 11, 821–829. <https://doi.org/10.1109/JSTARS.2018.2797894>
- Stenseth, N.C., Mysterud, A., 2002. Climate, changing phenology, and other life history traits: Nonlinearity and match-mismatch to the environment. *Proc. Natl. Acad. Sci. USA* 99, 13379–13381. <https://doi.org/10.1073/pnas.212519399>
- Stephens, S.L., Burrows, N., Buyantuyev, A., Gray, R.W., Keane, R.E., Kubian, R., Liu, S., Seijo, F., Shu, L., Tolhurst, K.G., van Wageningen, J.W., 2014. Temperate and boreal forest mega-fires: Characteristics and challenges. *Front. Ecol. Environ.* 12, 115–122. <https://doi.org/10.1890/120332>
- Stricker, K.B., Hagan, D., Flory, S.L., 2015. Improving methods to evaluate the impacts of plant invasions: lessons from 40 years of research. *AoB Plants* 7, Article plv028. <https://doi.org/10.1093/aobpla/plv028>
- Thill, D.C., Beck, K.G., Callihan, R.H., 1984. The Biology of Downy Brome (*Bromus tectorum*). *Weed Sci.* 32, 7–12.
- Thill, D.C., Schirman, R.D., Appleby, A.P., 1979. Influence of soil moisture, temperature, and compaction on the germination and emergence of Downy Brome (*Bromus tectorum*). *Weed Sci.* 27, 625–630. <https://www.jstor.org/stable/4043082>

- Tilman, D., Clark, M., Williams, D.R., Kimmel, K., Polasky, S., Packer, C., 2017. Future threats to biodiversity and pathways to their prevention. *Nature* 546, 73–81. <https://doi.org/10.1038/nature22900>
- Tortorelli, C.M., Krawchuk, M.A., Kerns, B.K., 2020. Expanding the invasion footprint: *Ventenata dubia* and relationships to wildfire, environment, and plant communities in the Blue Mountains of the Inland Northwest, USA. *Appl. Veg. Sci.* 1–13. <https://doi.org/10.1111/avsc.12511>
- Underwood, E.C., Ustin, S.L., Ramirez, C.M., 2007. A comparison of spatial and spectral image resolution for mapping invasive plants in coastal California. *Environ. Manage.* 39, 63–83. <https://doi.org/10.1007/s00267-005-0228-9>
- Ustin, S.L., Dipietro, D., Olmstead, K., Underwood, E., Scheer, G.J., 2002. Hyperspectral Remote Sensing for Invasive Species Detection and Mapping Band ratios. *Ieee* 00, 7536–7538. <https://doi.org/10.1109/igarss.2002.1026212>
- Vermote, E., Justice, C., Claverie, M., Franch, B., 2016. Preliminary analysis of the performance of the Landsat 8/OLI land surface reflectance product. *Remote Sens. Environ.* 185, 46–56. <https://doi.org/10.1016/j.rse.2016.04.008>
- Vermote, E.F., Saleous, N.E., Justice, C.O., Kaufman, Y.J., Privette, J.L., Remer, L., Roger, J.C., Tanr, D., 1997. Atmospheric correction of visible to middle-infrared EOS-MODIS data over land surfaces: Background, operational algorithm and validation. *J. Geophys. Res.* 102, 131–141.
- Virtanen, P., Gommers, R., Oliphant, T.E., Haberland, M., Reddy, T., Cournapeau, D., Burovski, E., Peterson, P., Weckesser, W., Bright, J., van der Walt, S.J., Brett, M., Wilson, J., Millman, K.J., Mayorov, N., Nelson, A.R.J., Jones, E., Kern, R., Larson, E., Carey, C.J., Polat, İ., Feng, Y., Moore, E.W., VanderPlas, J., Laxalde, D., Perktold, J., Cimrman, R., Henriksen, I., Quintero, E.A., Harris, C.R., Archibald, A.M., Ribeiro, A.H., Pedregosa, F., van Mulbregt, P., Vijaykumar, A., Bardelli, A. Pietro, Rothberg, A., Hilboll, A., Kloeckner, A., Scopatz, A., Lee, A., Rokem, A., Woods, C.N., Fulton, C., Masson, C., Häggström, C., Fitzgerald, C., Nicholson, D.A., Hagen, D.R., Pasechnik, D. V., Olivetti, E., Martin, E., Wieser, E., Silva, F., Lenders, F., Wilhelm, F., Young, G., Price, G.A., Ingold, G.L., Allen, G.E., Lee, G.R., Audren, H., Probst, I., Dietrich, J.P., Silterra, J., Webber, J.T., Slavič, J., Nothman, J., Buchner, J., Kulick, J., Schönberger, J.L., de Miranda Cardoso, J.V., Reimer, J., Harrington, J., Rodríguez, J.L.C., Nunez-Iglesias, J., Kuczynski, J., Tritz, K., Thoma, M., Newville, M., Kümmerer, M., Bolingbroke, M., Tartre, M., Pak, M., Smith, N.J., Nowaczyk, N., Shebanov, N., Pavlyk, O., Brodtkorb, P.A., Lee, P., McGibbon, R.T., Feldbauer, R., Lewis, S., Tygier, S., Sievert, S., Vigna, S., Peterson, S., More, S., Pudlik, T., Oshima, T., Pingel, T.J., Robitaille, T.P., Spura, T., Jones, T.R., Cera, T., Leslie, T., Zito, T., Krauss, T., Upadhyay, U., Halchenko, Y.O., Vázquez-Baeza, Y., 2020. SciPy 1.0: fundamental algorithms for scientific computing in Python. *Nat. Methods* 17, 261–272. <https://doi.org/10.1038/s41592-019-0686-2>

- Vose, R.S., Applequist, S., Squires, M., Durre, I., Menne, M.J., Williams, C.N., Jr., Fenimore, C., Gleason, K., Arndt, D., 2014. Improved historical temperature and precipitation time series for U.S.S climate divisions. *J Appl. Meteorol. Climatol.* 53, 1232–1251. <https://doi.org/10.1175/JAMC-D-13-0248.1>
- Wagner, R.G., Little, K.M., Richardson, B., McNabb, K., 2006. The role of vegetation management for enhancing productivity of the world's forests. *Forestry* 79, 57–79. <https://doi.org/10.1093/forestry/cpi057>
- Walker, J.J., de Beurs, K.M., Wynne, R.H., 2014. Dryland vegetation phenology across an elevation gradient in Arizona, USA, investigated with fused MODIS and Landsat data. *Remote Sens. Environ.* 144, 85–97. <https://doi.org/10.1016/j.rse.2014.01.007>
- Walker, J.J., de Beurs, K.M., Wynne, R.H., Gao, F., 2012. Evaluation of Landsat and MODIS data fusion products for analysis of dryland forest phenology. *Remote Sens. Environ.* 117, 381–393. <https://doi.org/10.1016/j.rse.2011.10.014>
- Wallace, J.M., Pavek, P.L.S., Prather, T.S., 2015. Ecological characteristics of *Ventenata dubia* in the Intermountain Pacific Northwest. *Invasive Plant Sci. Manag.* 8, 57–71. <https://doi.org/10.1614/IPSM-D-14-00034.1>
- Wang, P., Gao, F., Masek, J.G., 2014. Operational data fusion framework for building frequent Landsat-like imagery. *IEEE Trans. Geosci. Remote Sens.* 52, 7353–7365. <https://doi.org/10.1109/TGRS.2014.2311445>
- Wang, K., Wang, T., Liu, X., 2018. A review: Individual tree species classification using integrated airborne LiDAR and optical imagery with a focus on the urban environment. *Forests* 10, 1–18. <https://doi.org/10.3390/f10010001>
- Weisberg, P.J., Lingua, E., Pillai, R.B., 2007. Spatial Patterns of Pinyon–Juniper Woodland Expansion in Central Nevada. *Rangel. Ecol. Manag.* 60, 115–124. <https://doi.org/10.2111/05-224R2.1>
- West, A.M., Evangelista, P.H., Jarnevich, C.S., Kumar, S., Swallow, A., Luizza, M.W., Chignell, S.M., 2017. Using multi-date satellite imagery to monitor invasive grass species distribution in post-wildfire landscapes: An iterative, adaptable approach that employs open-source data and software. *Int. J. Appl. Earth Obs. Geoinf.* 59, 135–146. <https://doi.org/10.1016/j.jag.2017.03.009>
- Westerling, A.L., Hidalgo, H.G., Cayan, D.R., Swetnam, T.W., 2006. Warming and earlier spring increase western U.S. forest wildfire activity. *Science*. 313, 940–943. <https://doi.org/10.1126/science.1128834>
- White, M.A., Thornton, P.E., Running, S.W., 1997. A continental phenology model for monitoring vegetation responses to interannual climatic variability. *Global Biogeochem. Cycles* 11, 217–234. <https://doi.org/10.1029/97GB00330>

- Wilson, A.M., Wondercheck, D.E., Goebel, C.J., 1974. Responses of Range Grass Seeds to Winter Environments. *J Range Manag.* 27, 120-122.
<https://doi.org/10.2307/3896746>
- Wolkovich, E.M., Cook, B.I., Davies, T.J., 2014. Progress towards an interdisciplinary science of plant phenology: Building predictions across space, time and species diversity. *New Phytol.* 201, 1156–1162. <https://doi.org/10.1111/nph.12599>
- Wulder, M.A., White, J.C., Loveland, T.R., Woodcock, C.E., Belward, A.S., Cohen, W.B., Fosnight, E.A., Shaw, J., Masek, J.G., Roy, D.P., 2016. The global Landsat archive: Status, consolidation, and direction. *Remote Sens. Environ.* 185, 271–283. <https://doi.org/10.1016/j.rse.2015.11.032>
- Xu, H., Ding, H., Li, M., Qiang, S., Guo, J., Han, Z., Huang, Z., Sun, H., He, S., Wu, H., Wan, F., 2006. The distribution and economic losses of alien species invasion to China. *Biol. Invasions* 8, 1495–1500. <https://doi.org/10.1007/s10530-005-5841-2>
- Yang, L., Jin, S., Danielson, P., Homer, C., Gass, L., Bender, S.M., Case, A., Costello, C., Dewitz, J., Fry, J., Funk, M., Granneman, B., Liknes, G.C., Rigge, M., Xian, G., 2018. A new generation of the United States National Land Cover Database: Requirements, research priorities, design, and implementation strategies. *ISPRS J. Photogramm. Remote Sens.* 146, 108–123.
<https://doi.org/10.1016/j.isprsjprs.2018.09.006>
- Young, J., 1992. Ecology and management of medusahead (*Taeniatherum caput-medusae* ssp. *asperum* Melderis). *Gt. Basin Nat.* 52, 6.
- Young, J.A., Evans, R.A., 1970. Invasion of Medusahead into the Great Basin. *Weed Sci.* 18, 89–97.
- Zeng, L., Wardlow, B.D., Xiang, D., Hu, S., Li, D., 2020. A review of vegetation phenological metrics extraction using time-series , multispectral satellite data. *Remote Sens. Environ.* 237, 111511. <https://doi.org/10.1016/j.rse.2019.111511>
- Zhang, X., Friedl, M.A., Schaaf, C.B., Strahler, A.H., Hodges, J.C.F., Gao, F., Reed, B.C., Huete, A., 2003. Monitoring vegetation phenology using MODIS. *Remote Sens. Environ.* 84, 471–475. [https://doi.org/10.1016/S0034-4257\(02\)00135-9](https://doi.org/10.1016/S0034-4257(02)00135-9)
- Zhang, X., Liu, L., Liu, Y., Jayavelu, S., Wang, J., Moon, M., Henebry, G.M., Friedl, M.A., Schaaf, C.B., 2018. Generation and evaluation of the VIIRS land surface phenology product. *Remote Sens. Environ.* 216, 212–229.
<https://doi.org/10.1016/j.rse.2018.06.047>
- Zhang, X., Wang, J., Henebry, G.M., Gao, F., 2020. Development and evaluation of a new algorithm for detecting 30 m land surface phenology from VIIRS and HLS time series. *ISPRS J. Photogramm. Remote Sens.* 161, 37–51.
<https://doi.org/10.1016/j.isprsjprs.2020.01.012>

- Zhou, J., Jia, L., Menenti, M., Gorte, B., 2016. On the performance of remote sensing time series reconstruction methods – A spatial comparison. *Remote Sens. Environ.* 187, 367–384. <https://doi.org/10.1016/j.rse.2016.10.025>
- Zhu, X., Chen, J., Gao, F., Chen, X., Masek, J.G., 2010. An enhanced spatial and temporal adaptive reflectance fusion model for complex heterogeneous regions. *Remote Sens. Environ.* 114, 2610–2623. <https://doi.org/10.1016/j.rse.2010.05.032>
- Zimmermann, N.E., Edwards, T.C., Moisen, G.G., Frescino, T.S., Blackard, J.A., 2007. Remote sensing-based predictors improve distribution models of rare, early successional and broadleaf tree species in Utah. *J. Appl. Ecol.* 44, 1057–1067. <https://doi.org/10.1111/j.1365-2664.2007.01348.x>

APPENDICES

A. Landsat and MODIS Metadata

The following figure and table present details about the metadata associated with images used in the image fusion and evaluation. Cloud cover associated with all MODIS images used in the image fusion can be found in Figure A1. Metadata associated with the Landsat images used in the image fusion and evaluation can be found in Table A.1.

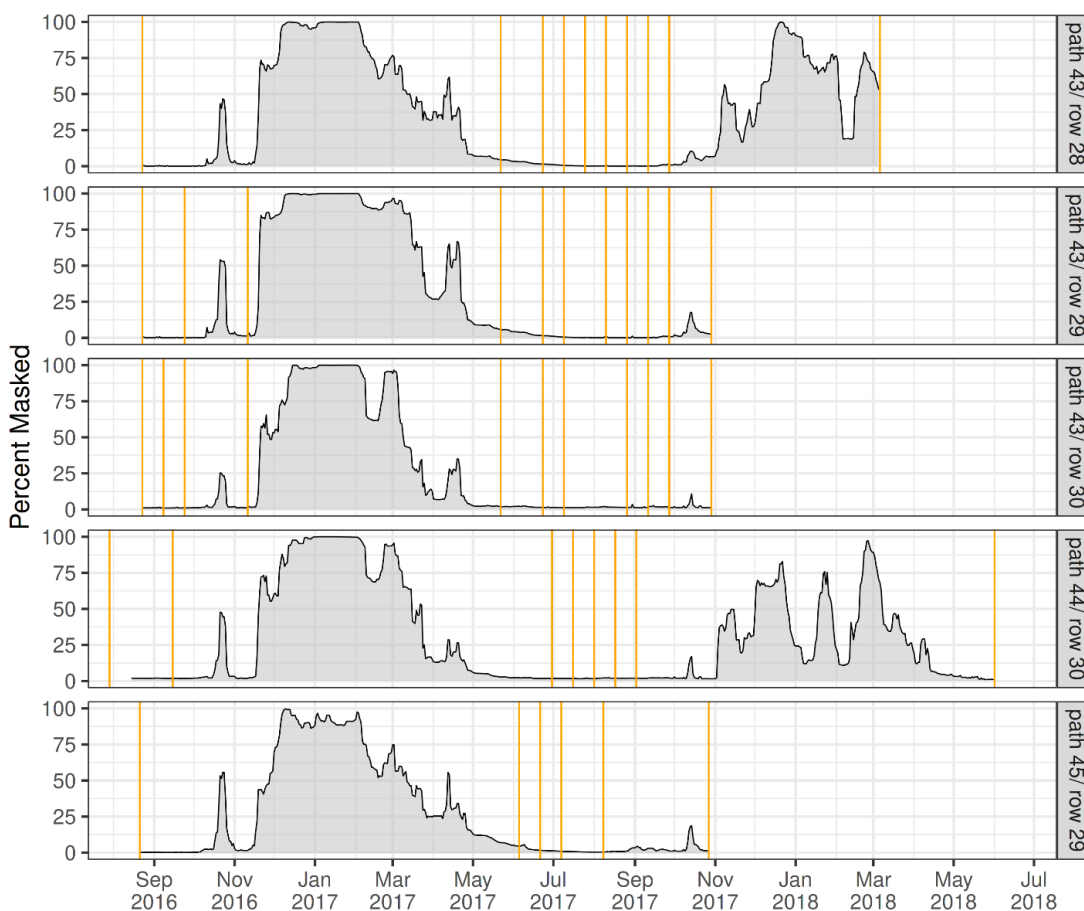


Figure A.1. The percent of MODIS pixels masked by date within the bounds of each Landsat WRS-2 scene used in the image fusion and LSP estimation. MODIS pixels were masked for snow and cloud cover. Vertical orange lines indicate the dates of the Landsat images paired with MODIS images (see Table A.1 for Landsat specific information).

Table A.1. All Landsat images used in the GEE image fusion and evaluation. Images used to evaluate the GEE image fusion and locally run ESTARFM algorithm are indicated with bold typeface.

Scene	Date	DOY	Cloud Cover (%)	Days to Next Pair
path 43/ row 28	08/23/16	236	0.1	271
	05/22/17	142	0.6	31
	06/23/17	174	0.4	15
	07/09/17	190	0.5	15
	07/25/17	206	0.5	15
	08/10/17	222	0.8	15
	08/26/17	238	0.0	15
	09/11/17	254	0.1	15
	09/27/17	270	0.4	159
	03/06/18	65	0.5	NA
path 43/ row 29	08/23/16	236	0.0	31
	09/08/16	252	15.0	NA
	09/24/16	268	0.9	47
	11/11/16	316	2.2	191
	05/22/17	142	4.2	31
	06/07/17	158	24.5	NA
	06/23/17	174	0.5	15
	07/09/17	190	1.3	31
	07/25/17	206	14.5	NA
	08/10/17	222	4.5	15
	08/26/17	238	0.0	15
	09/11/17	254	0.0	15
	09/27/17	270	0.4	31
10/29/17	302	0.4	NA	
path 43/ row 30	08/23/16	236	0.0	15
	09/08/16	252	0.1	15
	09/24/16	268	0.2	47
	11/11/16	316	0.2	191
	04/04/17	94	19.8	NA
	05/22/17	142	0.4	31
	06/23/17	174	0.0	15
	07/09/17	190	0.3	47
	07/25/17	206	20.1	NA
	08/10/17	222	17.4	NA
	08/26/17	238	0.0	15
	09/11/17	254	2.2	15
	09/27/17	270	0.2	31
10/29/17	302	0.2	NA	

Table A.1. Continued.

Scene	Date	DOY	Cloud Cover (%)	Days to Next Pair
	07/29/16	211	0.0	47
	09/15/16	259	0.3	287
	06/30/17	181	0.0	15
path 44/ row 30	07/16/17	197	0.8	15
	08/01/17	213	2.7	15
	08/17/17	229	0.0	15
	09/02/17	245	0.0	271
	06/01/18	152	0.2	NA
	08/21/16	234	0.0	287
	06/05/17	156	0.8	15
path 45/ row 29	06/21/17	172	1.0	15
	07/07/17	188	4.7	31
	08/08/17	220	0.1	79
	10/27/17	300	1.1	NA

B. Spatio-temporal Image Fusion Evaluation

The following figures show the relationship between true Landsat and fused images at the five dates used for image fusion evaluation that were not shown in the results section of chapter 2.

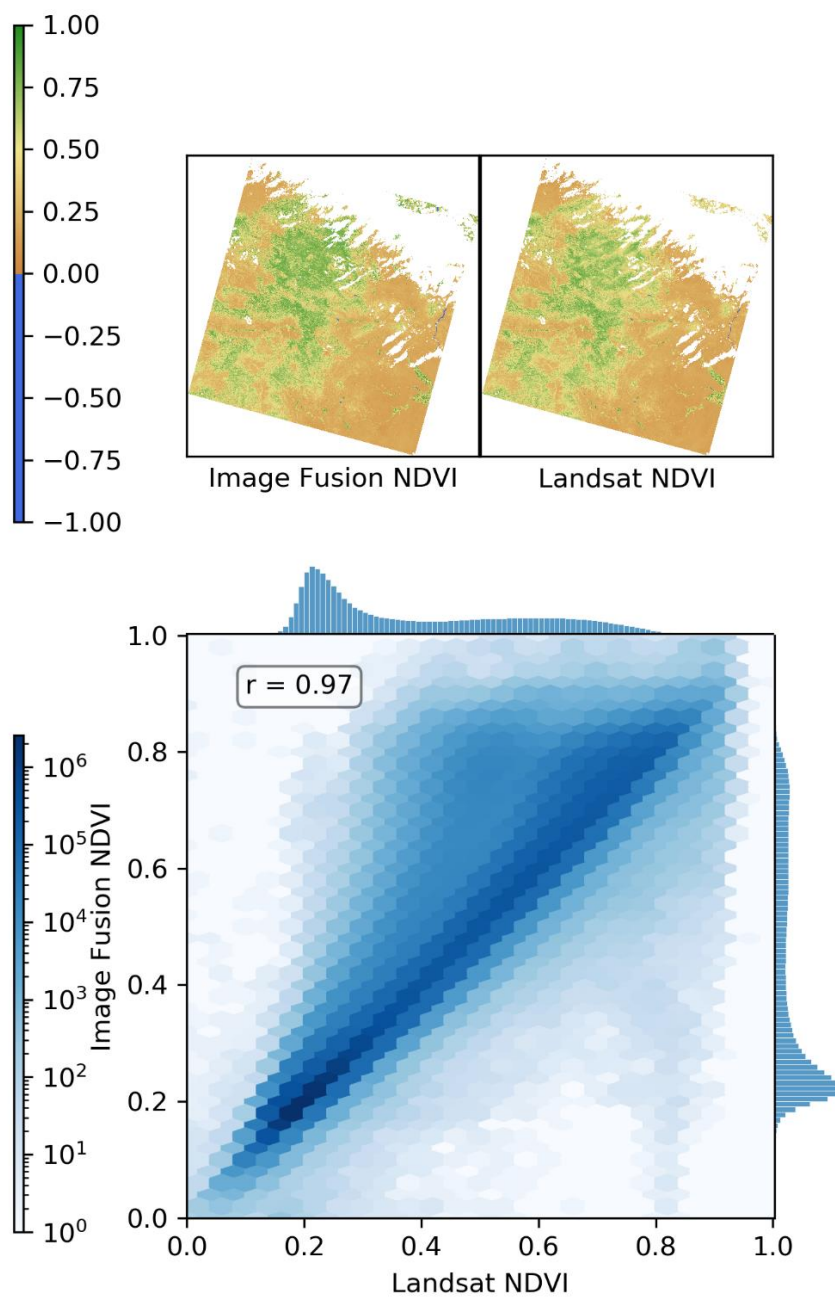


Figure B.1. Hex grid of the true Landsat NDVI vs. the GEE image fusion NDVI for path 43/ row 29 on DOY 252. See Table 2.1 for further evaluation details.

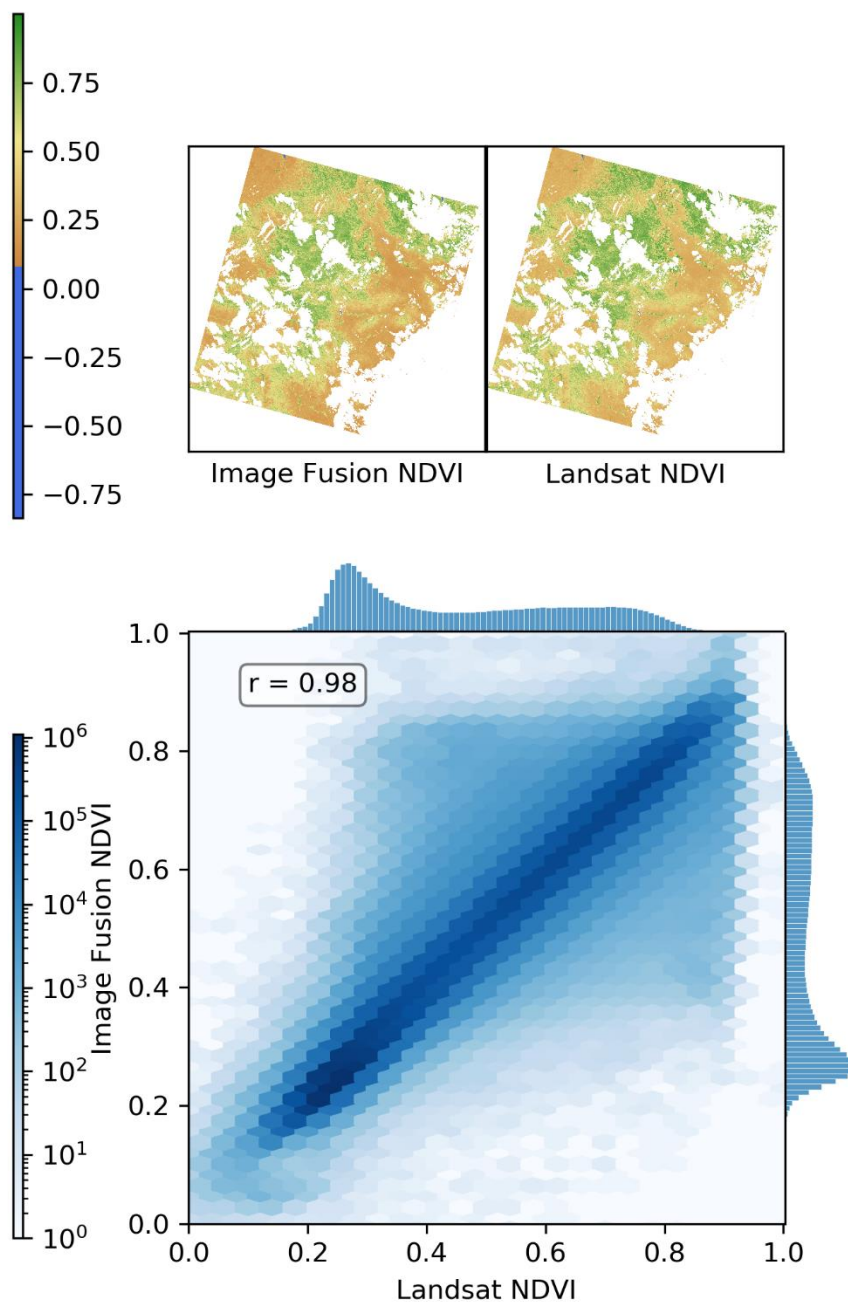


Figure B.2. Hex grid of the true Landsat NDVI vs. the GEE image fusion NDVI for path 43/ row 29 on DOY 206. See Table 2.1 for further evaluation details.

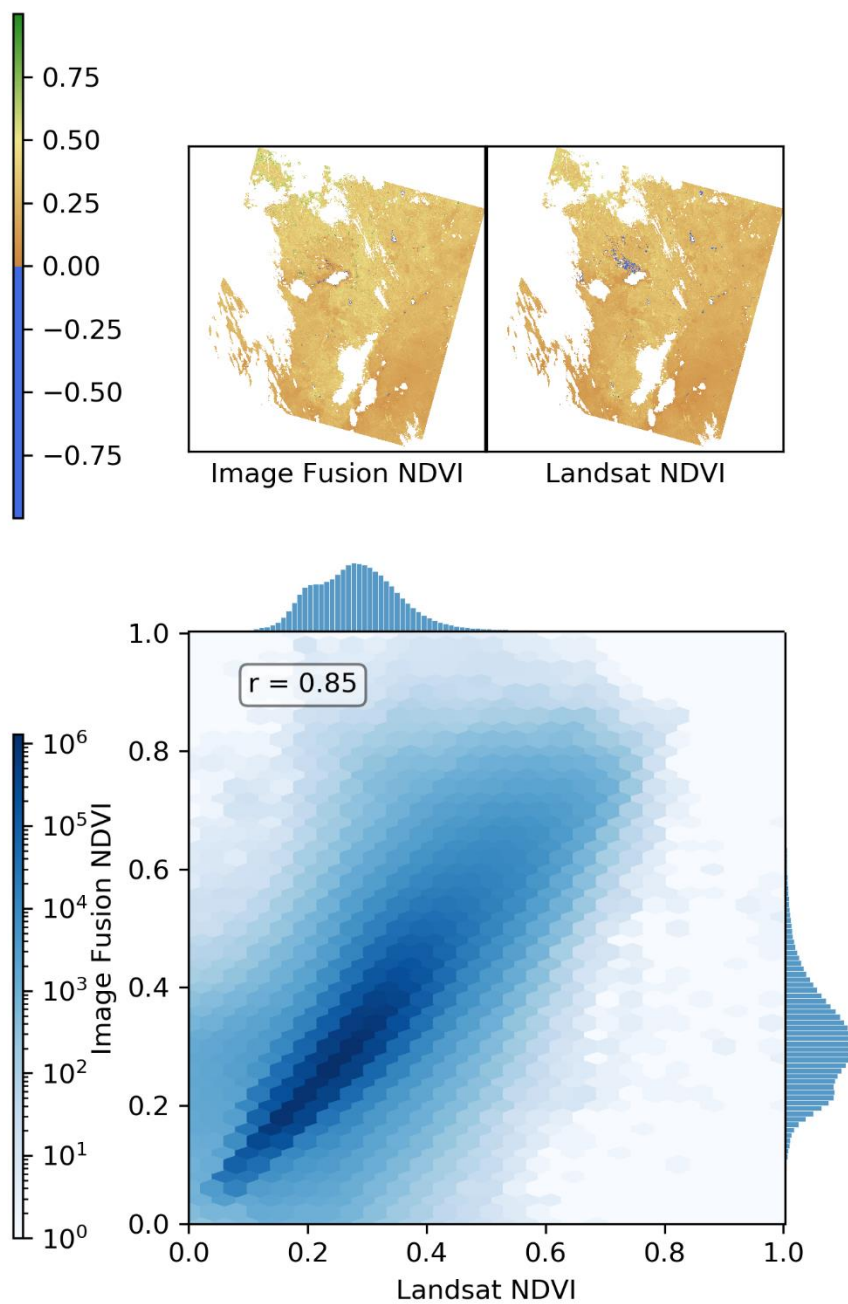


Figure B.3. Hex grid of the true Landsat NDVI vs. the GEE image fusion NDVI for path 43/ row 30 on DOY 94. See Table 2.1 for further evaluation details.

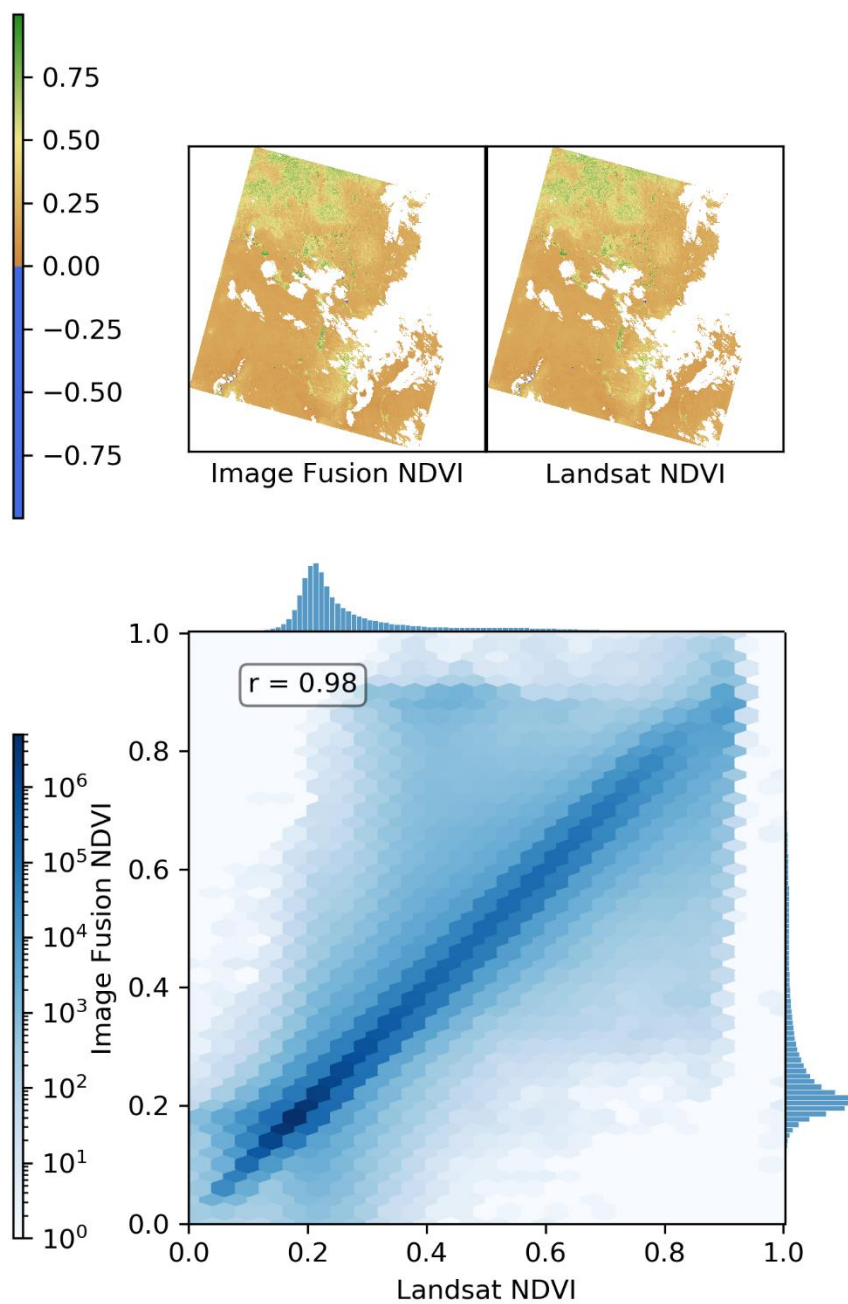


Figure B.4. Hex grid of the true Landsat NDVI vs. the GEE image fusion NDVI for path 43/ row 30 on DOY 206. See Table 2.1 for further evaluation details.

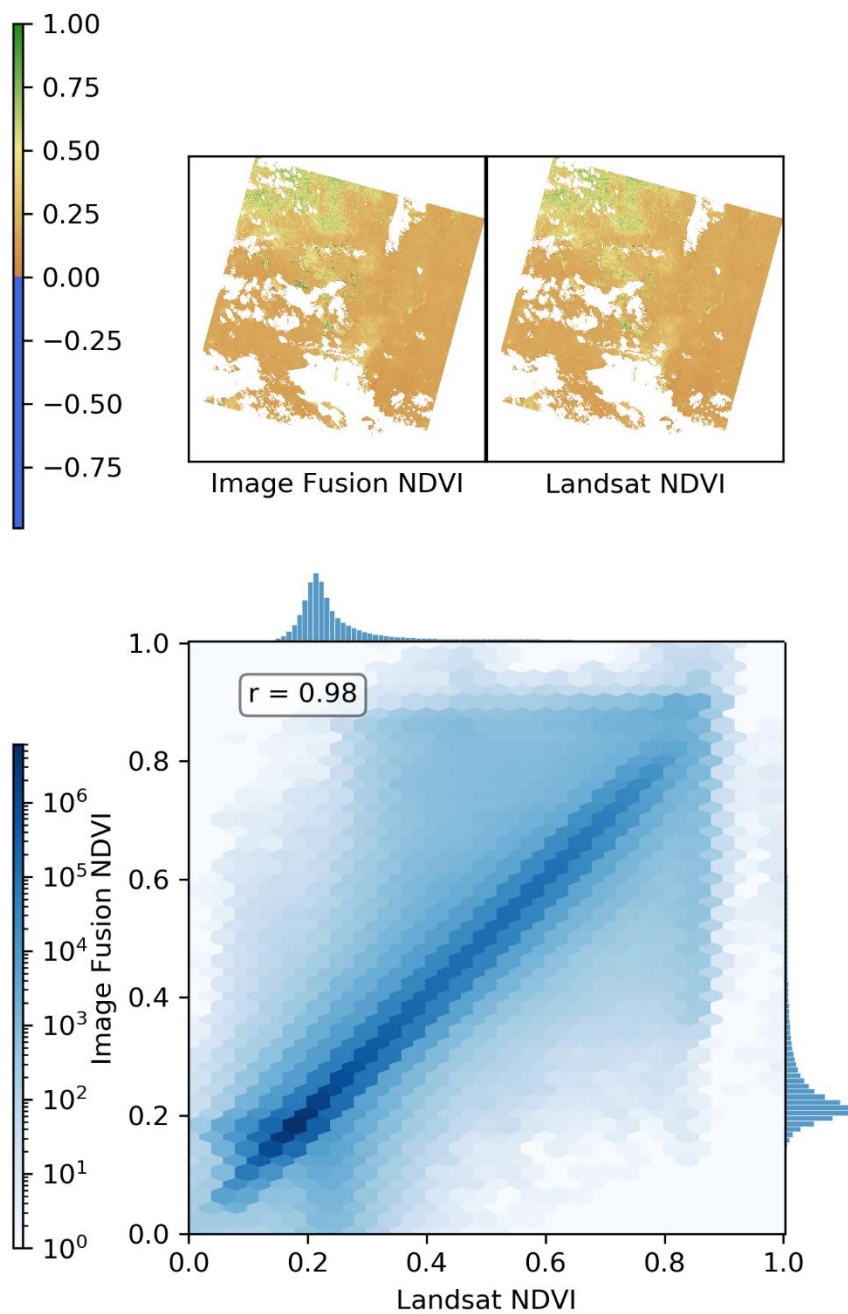


Figure B.5. Hex grid of the true Landsat NDVI vs. the GEE image fusion NDVI for path 43/ row 30 on DOY 222. See Table 2.1 for further evaluation details.

C. PhenoCam Time Series Comparisons

The agriculture and conifer forest PhenoCam sites showed little correspondence between G_{CC} and NDVI time series. Accordingly, the phenometrics extracted with the double logistic smoothing method were quite different. In both the NDVI and G_{CC} time series at the agriculture site the beginning of season was not captured leading to a relatively poor fit of the function and substantial difference in the phenometrics. Neither of the conifer sites had much seasonal variation in NDVI which strongly contrasts with the clear seasonal trend present in the G_{CC} time series.

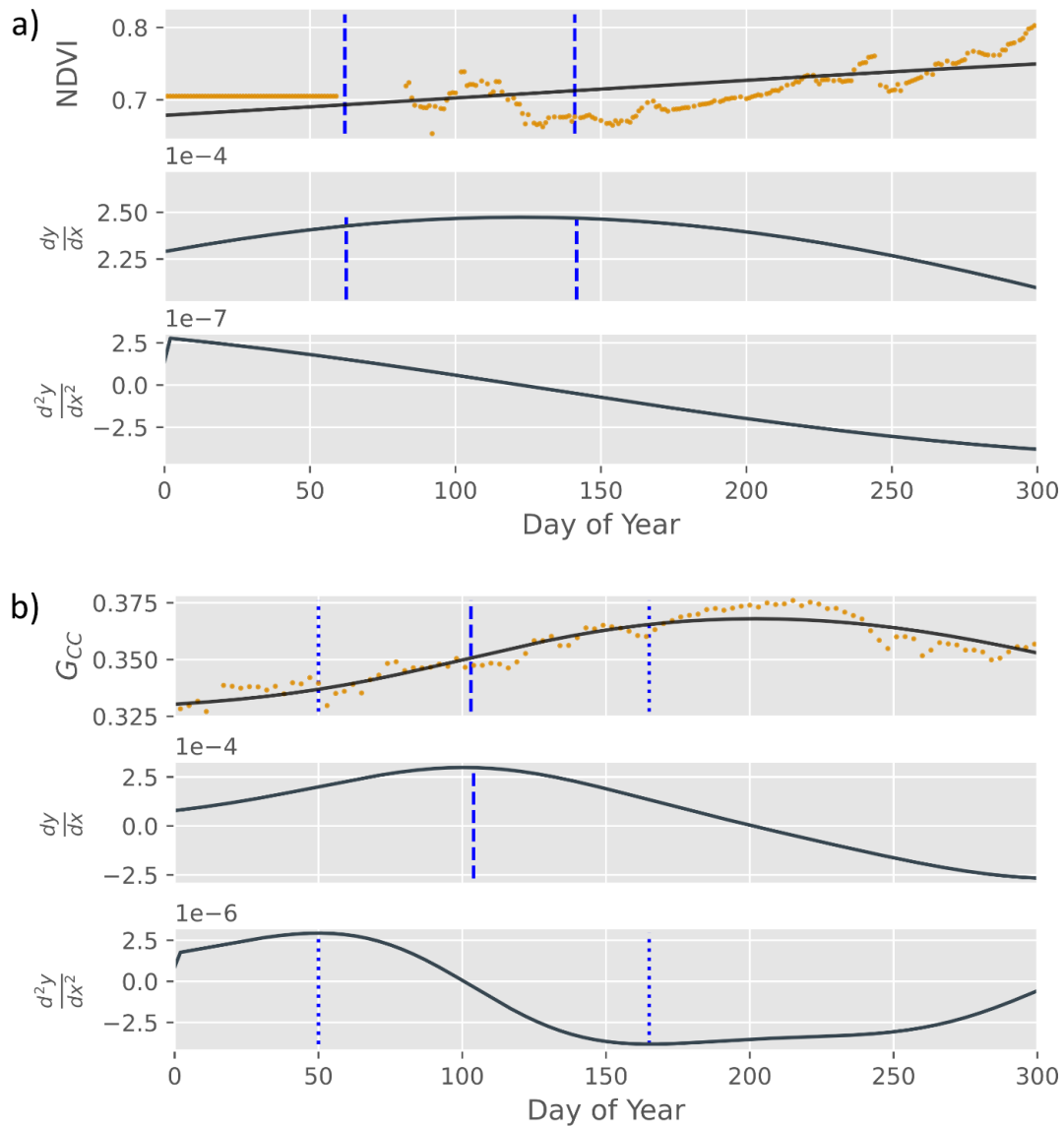


Figure C.1. Comparison of the time series and model fit for the conifer PhenoCam site near Sisters, Oregon (PhenoCam-2). The top panel (a) shows the image fusion NDVI-derived time series, model, and phenometrics. The bottom panel (b) shows the PhenoCam G_{cc} -derived time series, model, and phenometrics. For each main panel (e.g., a and b), the three subpanels follow the labeling and symbology conventions of Figure 2.3.

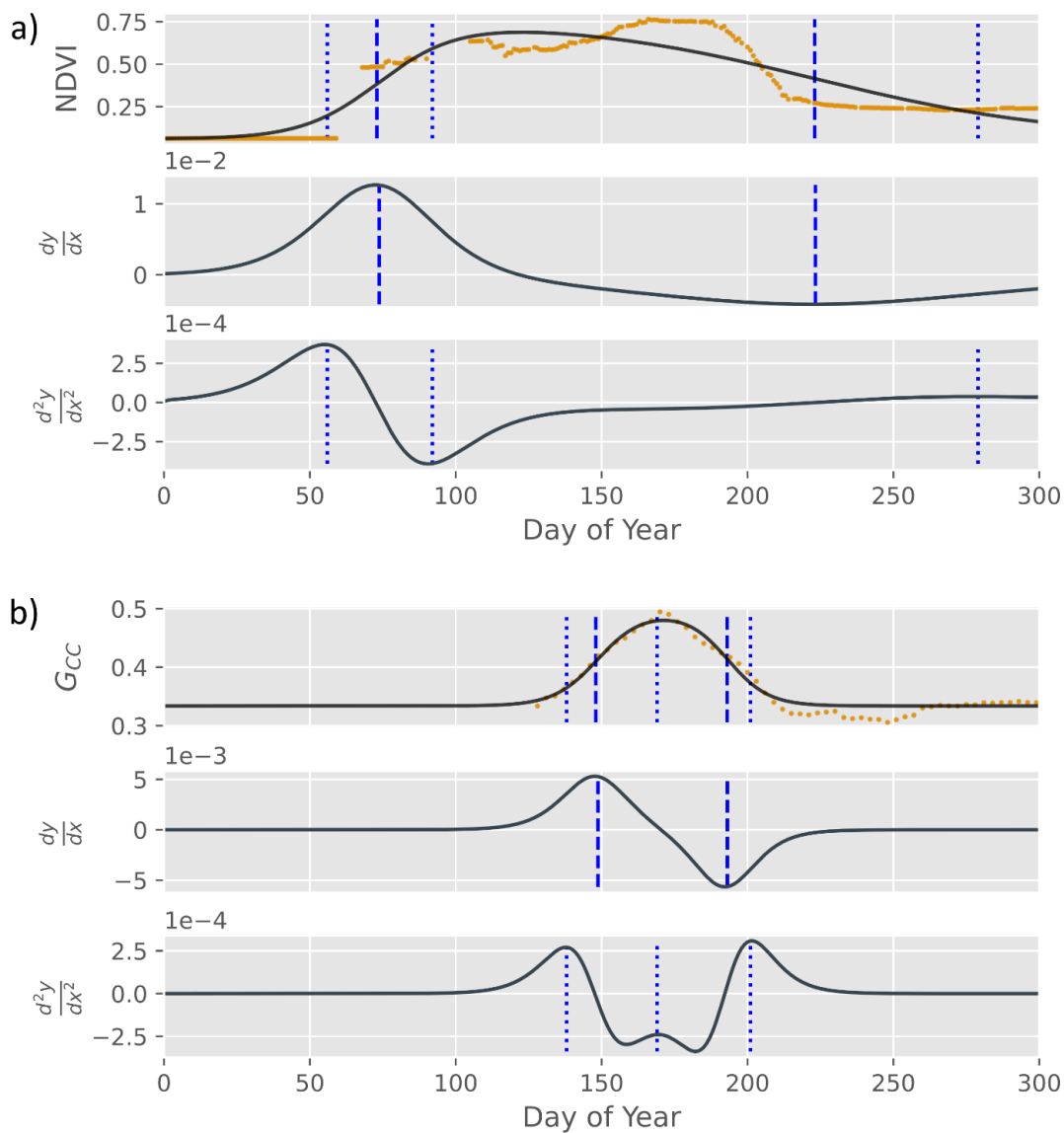


Figure C.2. Comparison of the time series and model fit for the agricultural PhenoCam site near Pullman, Washington (PhenoCam-4). The top panel (a) shows the GEE image fusion's NDVI-derived time series, model, and phenometrics. The bottom panel (b) shows the PhenoCam's G_{cc} -derived time series, model, and phenometrics. For each main panel (i.e., a and b), the three subpanels follow the labeling and symbology conventions of Figure 2.3.

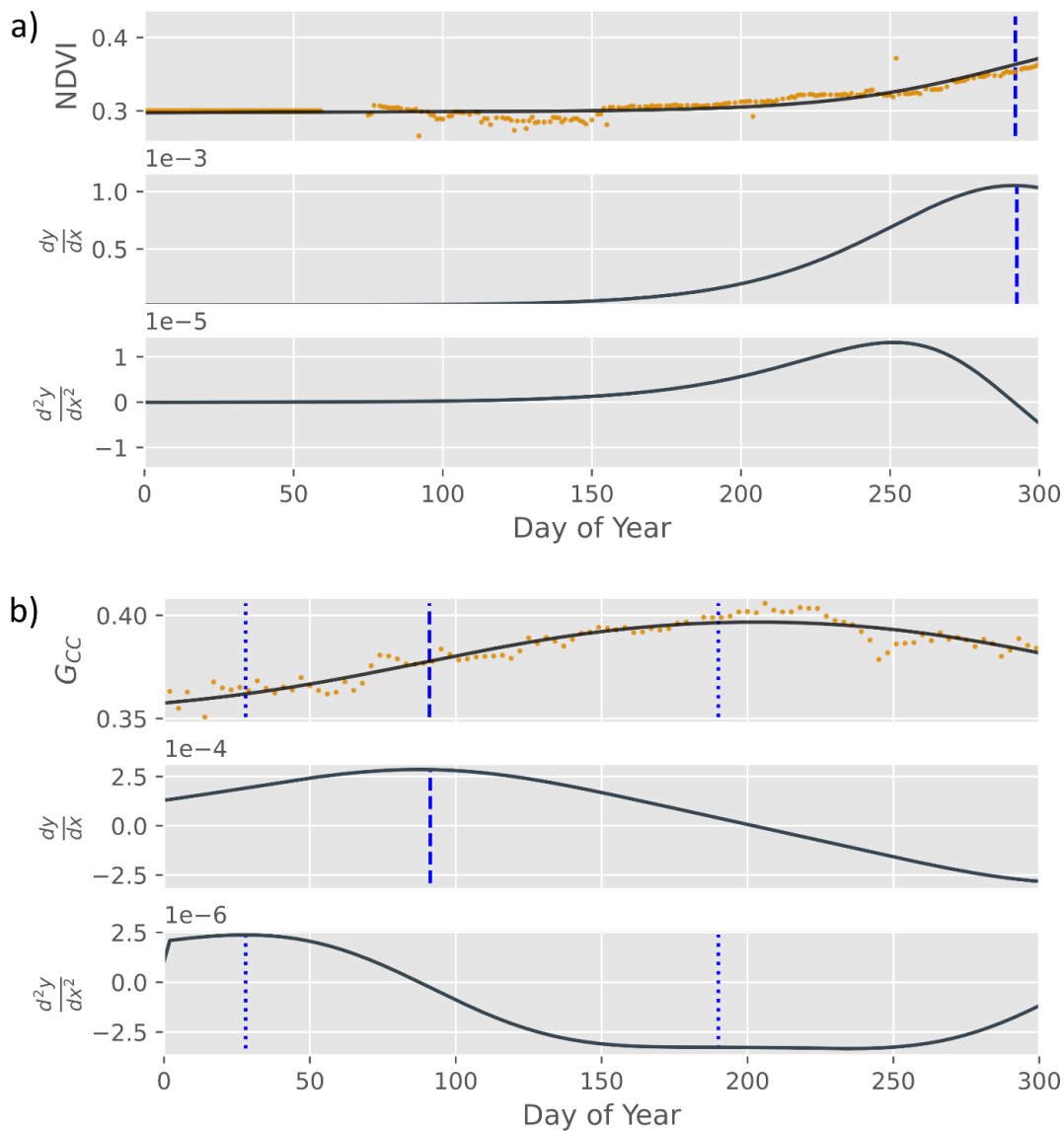


Figure C.3. Comparison of the time series and model fit for the conifer PhenoCam site near Sisters, Oregon (PhenoCam-3). The top panel (a) shows the GEE image fusion's NDVI-derived time series, model, and phenometrics. The bottom panel (b) shows the PhenoCam's G_{cc} -derived time series, model, and phenometrics. For each main panel (i.e., a and b), the three subpanels follow the labeling and symbology conventions of Figure 2.3.

D. Starkey Experimental Forest and Range Mixed Conifer Phenology

The phenology observed in the plots at the mixed conifer site in SEFR did not correspond with the phenometrics predicted from the image fusion data. This is to be expected in areas with high conifer canopy cover because the seasonal signal is indistinct. The overstory cover would have completely obscured any phenology occurring in the understory.

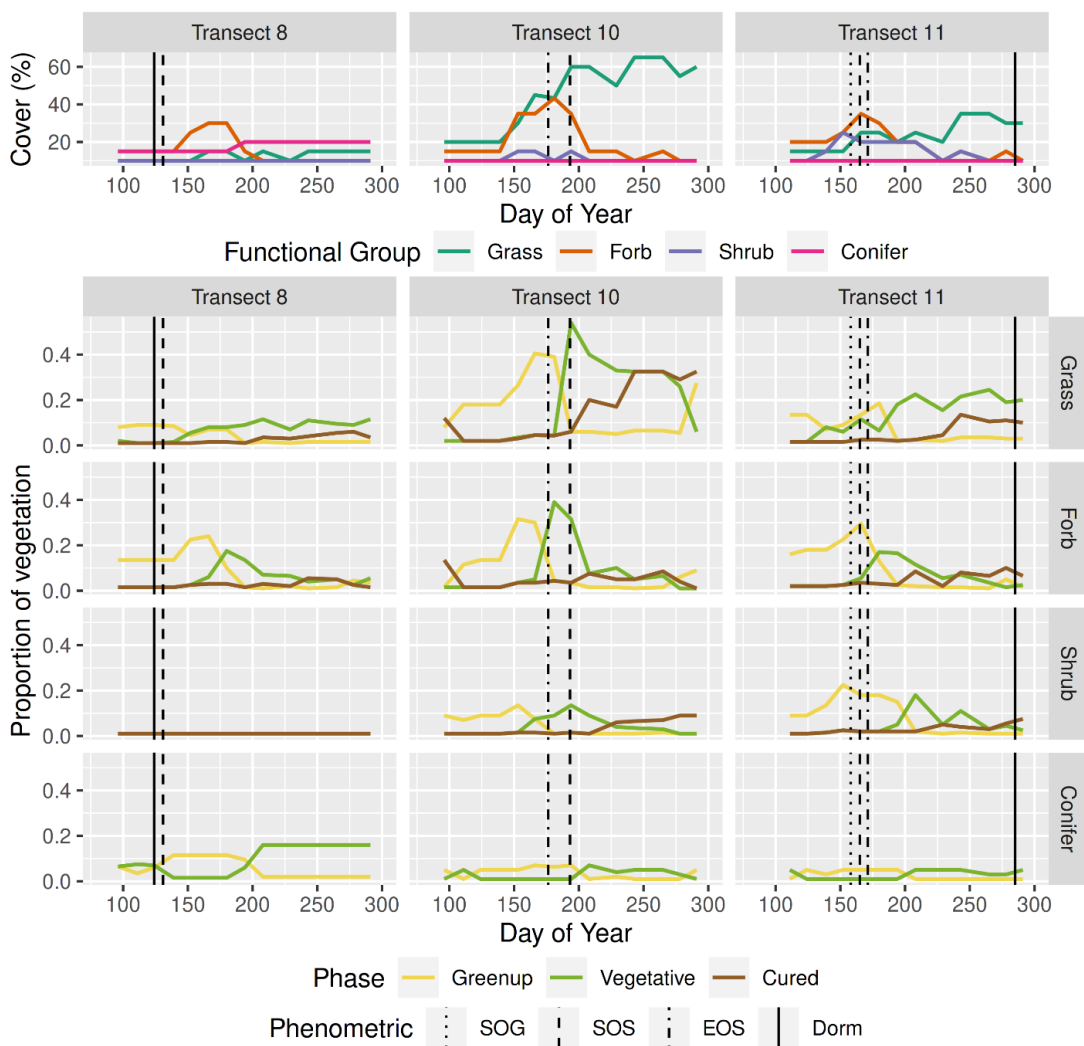


Figure D.1. The SEFR transects sampled in mixed conifer sites for the 2017 growing season. The top panel shows percent cover by functional group at the four sites (transects). The bottom panel shows the proportion of vegetation in each phase by functional group. In both panels, vertical lines show the phenometrics estimated

from the image-fusion based NDVI time-series, including start of green-up (SOG), start of season (SOS), end of season (EOS), and dormancy (Dorm).

E. Phenology, Climate, Soils, and Topography Predictors

Table E.1. Complete list of predictors used to model the presence and absence of *ventenata*.

Group	Acronym	Units	Description
Phenometrics	Dorm	Day of Year	Inflection point when greenness stops decreasing.
	EOS	Day of Year	Day in which decrease in greenness is steepest.
	LOS	Day of Year	Start and end of season difference.
	Mat	Day of Year	Day of maximum greenness based on function.
	SOS	Day of Year	Day in which increase in greenness is steepest.
	SOG	Day of Year	Inflection point when greenness starts rising.
	ROG	NDVI/Day	Steepness of increase in greenness at the SOS.
	ROS	NDVI/Day	Steepness of decrease in greenness at EOS.
	NDVI_Amp	NDVI	Baseline and maximum NDVI difference.
	NDVI_Max	NDVI	Maximum NDVI observed in 2017.
	NDVI_Min	NDVI	Median NDVI from September 2016 (baseline).
	GDD_at_Dorm	degrees Celsius	Cumulative GDD at dormancy.
	GDD_at_EOS	degrees Celsius	Cumulative GDD at EOS.
	GDD_at_Mat	degrees Celsius	Cumulative GDD at Maturity.
	GDD_at_SOG	degrees Celsius	Cumulative GDD at SOG.
GDD_at_SOS	degrees Celsius	Cumulative GDD at SOS.	
Climate	Ann_Ppt	millimeters	Total annual precipitation.
	Fall_Ppt	millimeters	Total fall precipitation.
	Spr_Ppt	millimeters	Total spring precipitation.
	Summ_Ppt	millimeters	Total summer precipitation.
	Wint_Ppt	millimeters	Total winter precipitation.
	Ann_Tmin	degrees Celsius	Mean annual monthly minimum temperature.
	Fall_Tmin	degrees Celsius	Mean fall monthly minimum temperature.
	Spr_Tmin	degrees Celsius	Mean spring monthly minimum temperature.
	Summ_Tmin	degrees Celsius	Mean summer monthly minimum temperature.
	Wint_Tmin	degrees Celsius	Mean winter monthly minimum temperature.
	Ann_Tmax	degrees Celsius	Mean annual monthly maximum temperature.
	Fall_Tmax	degrees Celsius	Mean fall monthly maximum temperature.
	Spr_Tmax	degrees Celsius	Mean spring monthly maximum temperature.
	Summ_Tmax	degrees Celsius	Mean summer monthly maximum temperature.
	Wint_Tmax	degrees Celsius	Mean winter monthly maximum temperature.
	Ann_VPDmin	hPa	Mean annual monthly minimum vapor pressure deficit.
	Fall_VPDmin	hPa	Mean fall monthly minimum vapor pressure deficit.
	Spr_VPDmin	hPa	Mean spring monthly minimum vapor pressure deficit.
Summ_VPDmin	hPa	Mean summer monthly minimum vapor pressure deficit.	
Wint_VPDmin	hPa	Mean winter monthly minimum vapor pressure deficit.	
Ann_VPDmax	hPa	Mean annual monthly maximum vapor pressure deficit.	
Fall_VPDmax	hPa	Mean fall monthly maximum vapor pressure deficit.	

Table E.1. Continued.

Group	Acronym	Units	Description
Climate	Spr_VPDmax	hPa	Mean spring monthly maximum vapor pressure deficit.
	Summ_VPDmax	hPa	Mean summer monthly maximum vapor pressure deficit.
	Wint_VPDmax	hPa	Mean winter monthly maximum vapor pressure deficit.
Soils	Clay_L1	percent	Clay content in the top 20 cm of the soil.
	Frag_L1	percent	Rock content in the top 20 cm of the soil.
	OM_L1	percent	Organic matter content in the top 20 cm of the soil.
	Sand_L1	percent	Sand content in the top 20 cm of the soil.
Topography	Slope	percent	Percent slope
	Eastness	Sine of Aspect	East to west gradient (1 to -1)
	Northness	Cosine of Aspect	North to south gradient (1 to -1)

F. Bioclimatic and Phenology Model Importance Plots

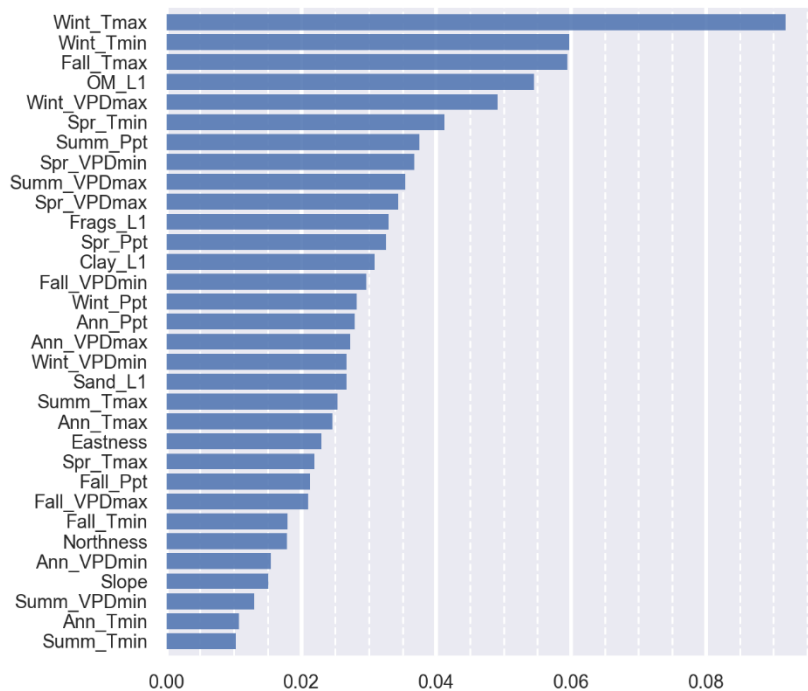


Figure F.1. Variable importance and rank of the 32 predictors in the bioclimatic model.

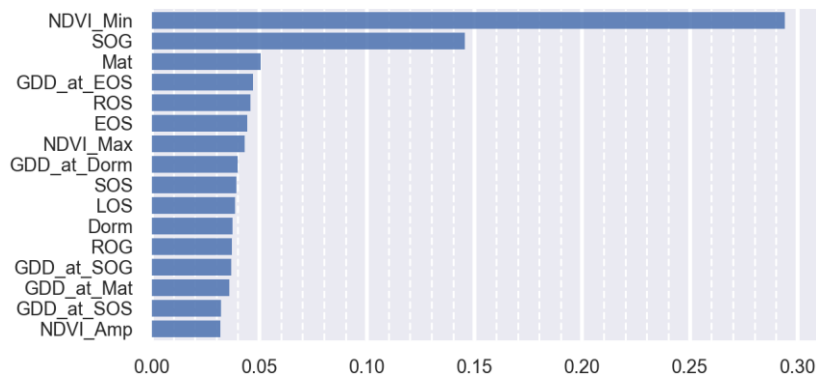


Figure F.2. Variable importance and rank of the 16 predictors in the phenology model.

Table G.2. Composition of the BME by PNV class and their representation in the ventenata field data set.

PNV	% of BME	n	Prevalence
Developed	4	1	0
Upland grass	11	93	0.19
Moist Meadow	1	4	0.5
Wet Meadow	0	1	0
Scabland Shrub	4	32	0.41
Upland Shrub	20	53	0.15
Riparian Shrub	0	1	0
Juniper Steppe	0	1	0
Juniper Woodlands	5	15	0.2
Ponderosa Pine-Lodgepole Pine	0	1	1
Dry Ponderosa Pine	1	16	0.13
Moist Ponderosa Pine	1	22	0.05
Xeric Pine	5	101	0.25
Dry Douglas-Fir	2	45	0.18
Moist Douglas-Fir	6	74	0.05
Dry White Fir - Grand Fir	2	69	0.04
Moist White Fir - Grand Fir	19	270	0.01
Wet White Fir - Grand Fir	3	45	0
Cold Dry White Fir - Grand Fir	2	88	0.03
Moist Subalpine Fir	1	3	0
Wet Subalpine Fir	2	5	0

H. Spatial Patterns of Ventenata Probability Difference and Percent Probability Difference

The following figures show the regional patterns in vegetation and the difference in probability of ventenata between 2006 and 2017. While the much of the region shows a small percentage decrease in probability, much of the lower elevation areas with this decrease had a low probability of occurrence in both 2006 and 2017. Many of the larger increases in probability occur in forests and ecotones across the region.

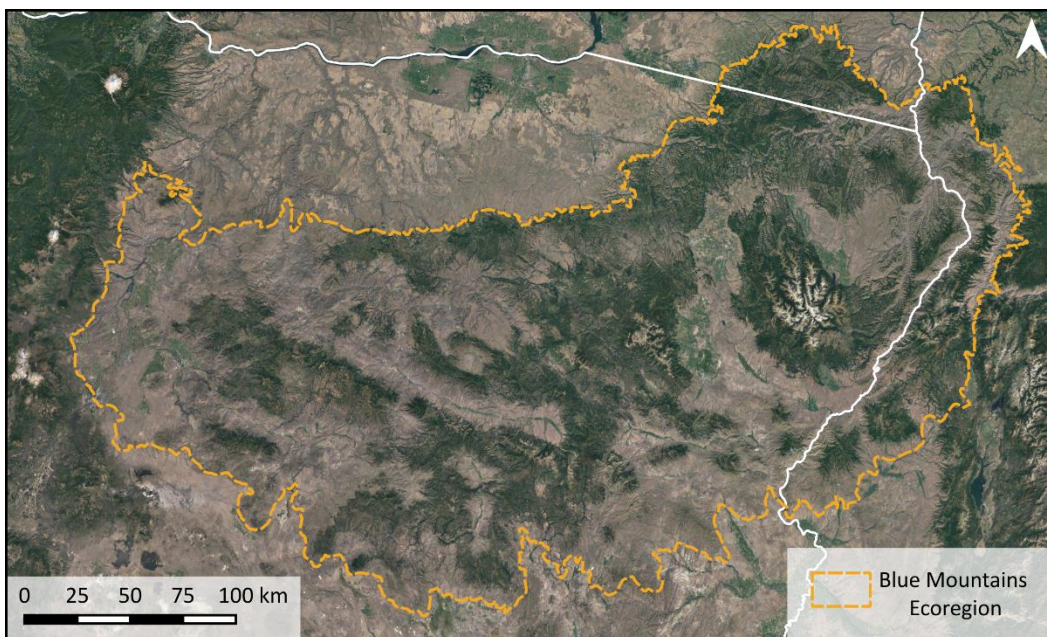


Figure H.1. Google satellite image showing the broad-scale spatial patterns of forested and non-forested areas within the Blue Mountains Ecoregion.

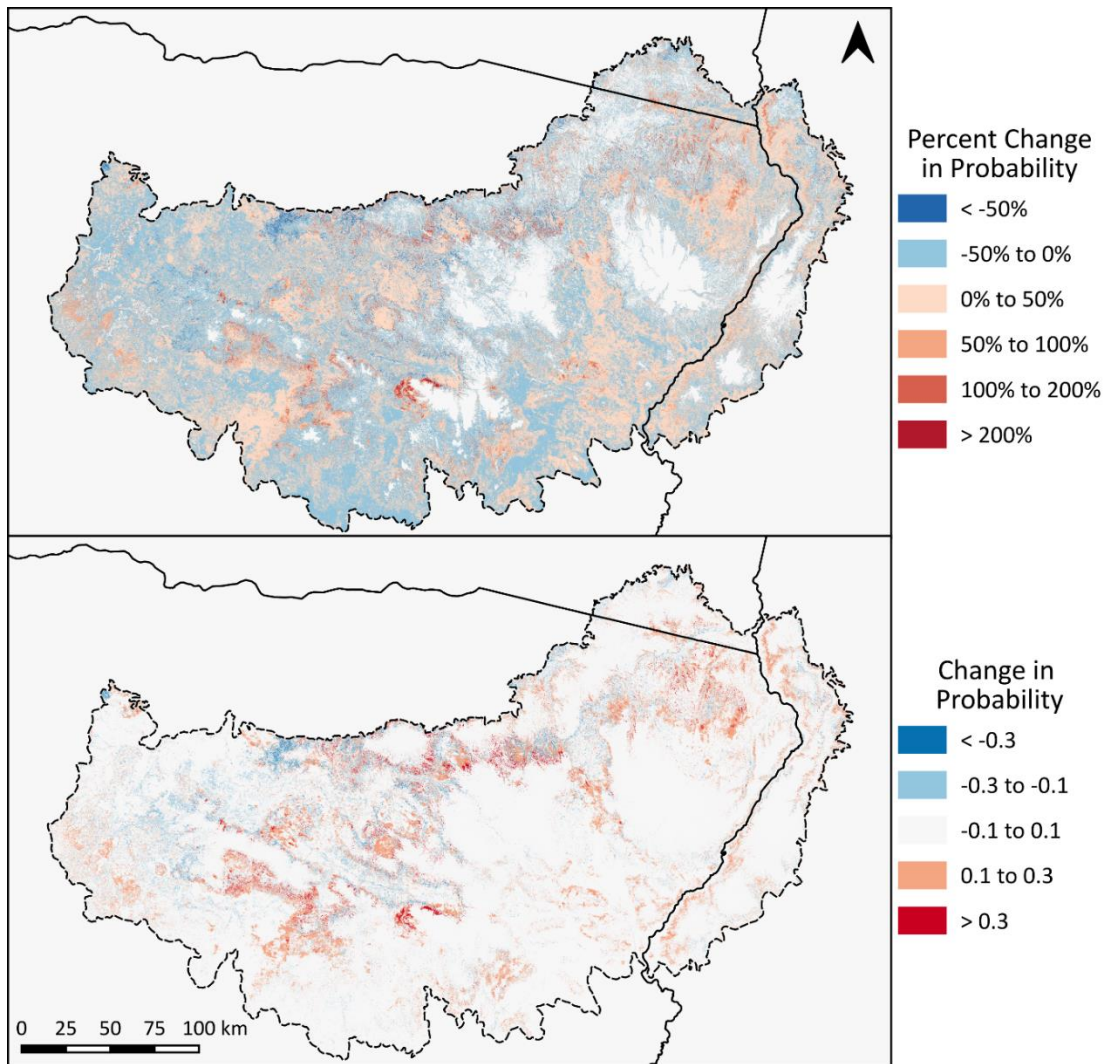


Figure H.2. Regional change in *ventenata* probability between 2006 and 2017. Positive values indicate that the probability was higher in 2017 than in 2006.